Gdańsk University of Technology
Faculty of Applied Physics nad Mathematics
Department of Physics of Electronic Phenomena

Doctor of Philosophy Dissertation

Photovoltaic phenomena in devices with perfluorozincphthalocyanine layer

by

Justyna Szostak

Supervisor: Prof. dr hab. Jan Godlewski
Co-supervisor: dr inż. Ryszard Signerski

Gdańsk, 2016

Acknowledgment

I would like to thank my supervisors - prof. dr hab. Jan Godlewski and dr inż. Ryszard Signerski, for their guidance, wise advising, patience and precious time.

I also wish to express my gratitude to my family and friends, especially to my husband Mariusz, my mom Irena and my best friend Gosia, who gave me support and motivation to work hard, and to my son Henio for beeing the joy of my life.

Contents

List of Symbols and Abbreviations

List of symbols:

a	width of the generation layer
α	bimolecular free electron-free hole recombination constant
c	speed of light
$C(x,t)$	concentration of CT statets
d	thickness of the regarded layer
D	diffusion constant
$Diss_C$	dissociation rate of CT statets
e	elementary charge
E_b^{CT}	binding energy of a charge-transfer exciton
E_b^{ex}	exciton binding energy
E_F	Fermi level
ε_0	vacuum permittivity
ε_r	dielectric constant (Relative permittivity of a material)
ε_A	dielectric constant (Relative permittivity of the acceptor material)
ε_D	dielectric constant (Relative permittivity of the donor material)
FF	fill factor
G_C	rate of generation of CT states from singlet excitons
G_L	rate of generation of CT states via recombination of free charge carriers
G_S	singlet exciton generation rate
G_{ex}	rate of free electron photogeneration
G_{th}	rate of thermal generation of free electrons
h	Planck's constant
I_0	incident light intensity
I_{sc}	short-circuit current
j_0	dark saturation current density
j_{diff}	diffusion current density
j_{drift}	drift current density
j_{MPP}	current density at the maximum power point

j_{sc}	short-circuit current density
κ	linear absorption coefficient
k	Boltzmann's constant
k_{diss}	exciton dissociation rate constant
k_R	free charge carrier recombination constant
k_R^p	free hole recombination constant inside the generation layer
k_R^n	free electron recombination constant inside the generation layer
L	exciton diffusion length
m	diode ideality factor
$n(x)$	free electron concentration
n_0	free electron concentration at the front electrode
n_0^{th}	free electron concentration at the front electrode under thermal equilibrium in the dark
n_d	free electron concentration at the rear electrode
n_d^{th}	free electron concentration at the rear electrode under thermal equilibrium in the dark
n_i	free electron concentration at the D/A junction
n_i^{th}	free electron concentration at the D/A junction under thermal equilibrium in the dark
λ	wavelength
μ	free charge carrier mobility
μ_p	hole mobility in a donor layer
μ_n	electron mobility in an acceptor layer
η	power conversion efficiency
η_{abs}	absorption efficiency
η_{diff}	exciton diffusion efficiency
η_{diss}	exciton dissociation efficiency
ρ	power density
ρ_{max}	maximum power density
$p(x)$	free hole concentration
p_0	free hole concentration at the front electrode
p_0^{th}	free hole concentration at the front electrode under thermal equilibrium in the dark

p_d	free hole concentration at the rear electrode
p_d^{th}	free hole concentration at the rear electrode under thermal equilibrium in the dark
p_i	free hole concentration at the D/A junction
p_i^{th}	free hole concentration at the D/A junction under thermal equilibrium in the dark
R_C	CT exciton annihilation rate
R_S	singlet exciton annihilation rate
R_s	series resistance
R_{sh}	shunt resistance
RR	rectification ratio
s	exciton annihilation velocity
$S(x),\ S(x,t)$	concentration of singlet excitons
T	absolute temperature
τ	exciton/free charge carrier lifetime
U_{oc}	Open-circuit voltage
v_d	electron drift velocity
v_R	surface recombination velocity
V_{MPP}	voltage at the maximum power point
W	incident light intensity measured in W/cm^2
φ_C	free charge carrier collection efficiency
Φ_0^{ex}	exciton flux density annihilation rate

List of abbreviations:

BHJ	Bulk heterojunction
CFA	Constant field approximation
CNT	Carbon nanotube
CT	Charge-transfer
CVD	Chemical vapor deposition
D/A	Donor/acceptor
DSC	Dye-sensitized solar cell
EBL	Exciton blocking layer
ETL	Electron transporting layer
HOMO	Highest occupied molecular orbital
HTL	Hole transporting layer
HWF	High work function
ICL	Interconnection layer
IPCE	Incident photon to current efficiency
ITO	Indium tin oxide
LUMO	Lowest unoccupied molecular orbital
LWF	Low work function
MBE	Molecular beam epitaxy
MPc	Metal phthalocyanine
MPP	Maximum power point
MS	Magnetron sputtering
OSC	Organic solar cell
OPV	Organic photovoltaics
PV	Photovoltaic
PVD	Physical vapor deposition
SEC	Shockley equivalent circuit
SRH	Shockley-Read-Hall
TCO	Transparent conducting oxide

Chapter 1

Motivation and aim of the study

By now, the most common acceptor materials used in organic photovoltaics are Buckminsterfullerene (C_{60}) and its derivatives, like soluble PCBM ((6,6)-phenyl C_{61} butyric acid methyl ester). Good electron accepting properties and relatively high electron mobilities shown by these materials and the fact that an ultrafast electron transfer from various donor materials to these molecules is observed account for the popularity of these compounds. Nevertheless, these materials have some serious drawbacks. First of all, they absorb light mainly in the ultraviolet range, so that solar cells incorporating these materials harvest light from the spectral range limited to the donor absorption range. Second of all, fullerenes and their derivatives are very susceptible to air, therefore fast degradation of solar cells that are not encapsulated and utilize these compounds is unavoidable. Hence, further improvement of organic solar cells relies on finding new acceptor materials with proper electron affinities [1], stability and capability of light harvesting in the visible range [2].

Acceptor materials are materials characterized by high values of electron affinity, so their HOMO (the highest occupied molecular orbital) and LUMO (the lowest unoccupied molecular orbital) energy levels lie below HOMO and LUMO levels of their donor counterparts. It was reported that substitution of molecules with electron withdrawing groups lowers HOMO and LUMO energy levels making such substituted molecules less susceptible to oxidation [3]. Moreover, if the unsubstituted molecule is a donor material and the shift of HOMO and LUMO levels resulting from the chemical modification mentioned above is significant,

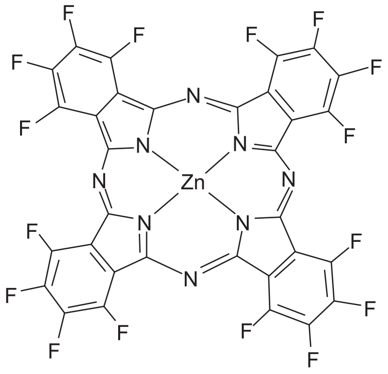

$F_{16}ZnPc$

Figure 1.1: Chemical structure of perfluorozincphthalocyanine molecule.

these substituted molecules will show electron accepting properties. Such effect is obtained when metallophthalocyanines (MPcs) are substituted with fluorine atoms. Complete fluorination of the phthalocyanine ring (all 16 external hydrogen atoms are exchanged with fluorine atoms) causes a 1.6 eV downward shift of HOMO and LUMO energy levels of these molecules. Therefore, perfluorinated (hexadecafluorinated) metallophthalocyanines (F_{16}MPcs) are very stable in air and can be used as electron acceptors and n-type organic semiconductors [3, 4] in contrast to their unsubstituted counterparts. Furthermore, according to Bao et al. [3], molecules in thin layers of all hexadecafluorinated MPcs adopt an edge-on conformation, so that only fluorine atoms are in touch with ambient air. This may prevent penetration of these films by moisture and enhance stability of solar cells with such layers.

For the aforementioned reasons, one of perfluorinated metallophthalocyanines, namely perfluorozincphthalocyanine (F_{16}ZnPc), whose chemical structure is shown in Fig.1.1, was chosen as an acceptor material in organic planar solar cells fabricated in the course of this study. The aim of this research is to investigate the photovoltaic phenomenon in single layer and bilayer donor/acceptor systems utilizing a thin layer of F_{16}ZnPc since there are only few reports regarding application of this molecule as the active material in solar cells. It has been used in photoelectrochemical cells [5], hybrid organic/inorganic devices [6], organic donor/acceptor [7] and n-n type solar cells [7, 8]. The latter make use of exciton recombination at a junction of two electron acceptors, thus they harvest light from a limited range of wavelengths in which both acceptors show high absorption coefficients. Therefore, it seems justified to verify the applicability of F_{16}ZnPc in donor/acceptor systems in which absorption spectra of materials forming the active junction complement one another enabling such cell to utilize light from the whole visible range. Moreover, some properties of the F_{16}ZnPc layer that determine its utility in the field of organic photovoltaics can be concluded from the analysis of photovoltaic phenomenon observed in single layer cells based on this material. Therefore, the aim of this work is to study the photovoltaic phenomenon occurring in organic polymer/F_{16}ZnPc and small molecule/F_{16}ZnPc planar cells in which both donor and acceptor materials show significant absorption of light in a broad spectral range as well as in single layer cells containing thin layers of F_{16}ZnPc. Another goal of this research is to develop theoretical models of current-voltage behavior of single and bilayer organic solar cells in order to verify the relation between the performance of fabricated devices and properties of used materials and layers they form.

Chapter 2

Optical properties of organic materials

Organic molecules in a solid state attract each other mainly via weak van der Waals forces, also known as dispersion forces, resulting from the presence of fluctuating electric dipoles even in case of non-polar symmetric molecules. In such case, a molecule of a temporary polarity induces a temporary dipole in a neighboring molecule. The latter affects the distribution of electrons in the adjacent molecule and in such way temporary dipoles are induced within a whole lattice. Polarities of molecules in the lattice fluctuate with synchronization maintaining the attraction between the molecules. The lack of strong intermolecular interaction is the reason why optical and electrical properties of individual molecules are mostly preserved in organic solids. The number of atoms forming an organic compound and so the number of electrons and degrees of freedom of one molecule may be quite large. This complexity accounts for the large number of molecular electronic states and possible transitions between them. Energetic and spatial distributions of electrons within an isolated molecule are described via molecular orbitals. The highest occupied and the lowest unoccupied molecular orbitals are called HOMO and LUMO respectively and their positions determine important optoelectronic properties of organic materials. Since in a solid phase molecules interact with each other weakly only upper atomic orbitals merge and create localized molecular orbitals, while intermolecular bands are very narrow (band width is lower than 0.1 eV) and electronic structure of an organic solid mostly preserves the electronic structure of a single molecule or a polymer chain. Therefore terms HOMO and LUMO may often refer not only to molecular orbitals of separated molecules

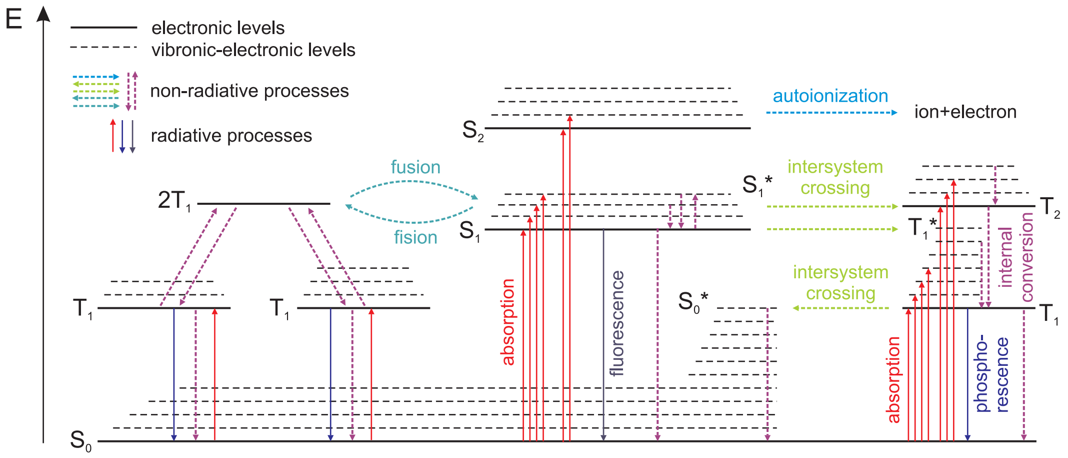

Figure 2.1: Common energy levels and possible transitions between them in organic crystals. S and T refer to singlet and triplet excitons respectively, while high vibronic-electronic levels are marked with an asterisk. Levels corresponding to trapped singlet and triplet excitons were not included on the scheme. Redrawn after [9].

but also to positions of electronic bands in organic solids [10]. These bands are understood as transport bands for free holes and free electrons and the difference between the edges of these bands is called the transport or electronic band gap E_{gE}. Absorption of light by a molecular solid state usually does not cause direct generation of free charge carriers. It rather leads to photoexcitation of a material, i.e. to creation of strongly bound electron-hole pairs called Frenkel excitons. Depending on the spin configuration a singlet (S) or a triplet (T) state is formed. The optical band gap E_{gO} determining the optical absorption edge is lower than the electronic one by the value of the exciton binding energy E_b^{ex} [11]

$$E_{gO} = E_{gE} - E_b^{ex} \ . \tag{2.1}$$

Molecules may be excited to various electronic levels or to higher vibronic-electronic levels $(S^*$ or $T^*)$ of some excess energy. All these states undergo many radiative and non-radiative processes, such as

- internal conversion
- intersystem crossing
- fluorescence

- phosphorescence
- radiative transfer
- resonance transfer
- exciton transfer
- exciton interaction
- autoionization

Internal conversion is a non-radiative process proceeding without a change in multiplicity. During this process vibrational portion of exciton energy is transferred to the lattice in a form of phonons [9]. Another non-radiative process excitons may undergo is an adiabatic spin-orbit coupling dependent process between states of different multiplicity termed an intersystem crossing. Mainly a fast $(\sim 10^{-8}$ s$)$ cross over from the lowest first excited singlet state S_1 to a highly vibrating first triplet state T_1^* followed by internal conversion to the lowest first triplet state T_1 is observed, while analogical transition from the latter state to the ground state S_0 via a highly vibrating level S_0^* is also possible but much slower $(\sim 10^{-4}$ s$)$. Fluorescence and phosphorescence are radiative decays from the lowest n-th excited singlet and triplet levels respectively to the ground state S_0. Fluorescence $(\sim 10^{-8}$ s$)$ is much faster than phosphorescence $(\sim 10^{-2}$ s$)$, since the latter requires a change in multiplicity. If one of molecules, called a donor, emits a photon that is subsequently reabsorbed by another molecule, called an acceptor, we speak of radiative transfer that may occur between molecules of different materials as long as absorption spectrum of the acceptor molecule overlaps the fluorescence spectrum of the donor molecule. This condition is also valid in case of a long range (up to few nm [9, 12]) non-radiative resonance transfer, also known as Förster transfer based on a dipole-dipole interactions during which total spins of both species involved in such transfer are conserved, and since the ground state is usually a singlet state Förster transfer is possible only in case of singlet excitons [12]. Since excitons interact with their surroundings single excitation levels split into bands of the number of levels dependent on the number of molecules per unit cell of a crystal. Such splitting is called Davydov splitting and its magnitude depends upon the strength of resonance interactions between molecules [13]. Davydov splitting is the reason why exciton levels in organic solids lie lower than exciton levels of single molecules. It originates from an overlap of neighboring molecular orbitals that enables exciton transfer dependent on the coupling energy between an excited molecule and adjacent unexcited molecule [9]. If such coupling energy is low then exciton transfer is slow and other competing process, like luminescence, are more probable. Apart from Förster transfer, which enables migration of singlet states only, Dexter transfer may occur [12]. This process may be understood as simultaneous transfer of an electron and a hole to the adjacent unexcited molecule during which the total spin of both molecules is conserved, hence triplet state may migrate in this way as well. According to Wróbel et al., Förster transfer takes place when the distance between donor and acceptor molecules ranges from 0.5 nm to 10 nm, while Dexter transfer is possible if the separation between these entities does not exceed 0.5 nm [14]. If the energy of an exciton is high enough autoionazition may occur which means that a free electron and a positive ion are formed. Another possibility of exciton energy dissemination is exciton interaction with other entities, like free charge carriers or other excitons if their concentration is high enough. The main types of these interactions and their consequences are listed below, while schematic illustration of energy levels in an organic solid and possible transitions between electronic states is shown in Fig. 2.1.

- homofission
  $S_1 + S_0 \longrightarrow T_1 + T_1$
- singlet-singlet, triplet-triplet or singlet-triplet annihilation
  $S_1 + S_1 \longrightarrow S_1^* + S_0 \longrightarrow S_1 + S_0 + \text{phonons}$
  $S_1 + S_1 \longrightarrow e + h$
  $S_1 + S_1 \longrightarrow T_1^* + T_1^*$
  $T_1 + T_1 \longrightarrow S_1^* + S_0 \longrightarrow S_1 + S_0 + \text{phonons}$
  $T_1 + T_1 \longrightarrow T_2 \text{ (or } T_1^*) + S_0 \longrightarrow T_1 + S_0 + \text{phonons}$
  $S_1 + T_1 \longrightarrow T_2^* + S_0$
  $S_1 + T_1 \longrightarrow e + h$
- exciton-charge carrier interaction

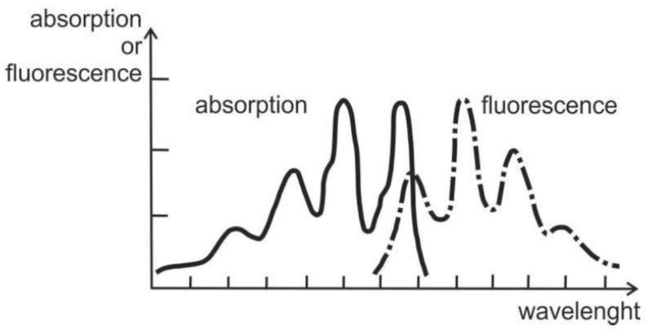

Figure 2.2: Absorption and fluorescence spectra of organic solids showing the mirror symmetry following from the Stokes shift [15].

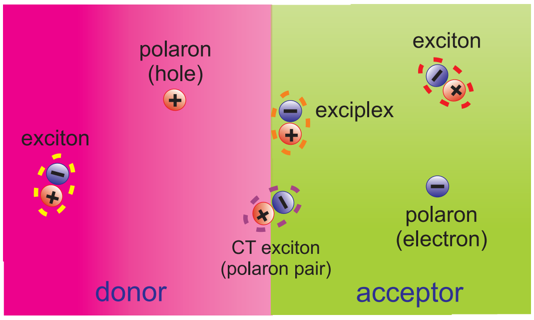

Figure 2.3: Schematic representation of excited states and polarons generated in organic materials.

$$\mathrm{S_1} + \text{free or trapped e (or } h) \longrightarrow \mathrm{S_0^*} \text{ (or } \mathrm{T_1^*}) + \text{e (or h)}$$

$$\mathrm{T_1} + \text{free or trapped e (or h)} \longrightarrow \mathrm{S_0} + \text{e (or h)}$$

- exciton-photon interaction

  $$\mathrm{S_1} \text{ (or } \mathrm{T_1}) + \mathrm{h}\nu \longrightarrow \mathrm{e} + \mathrm{h}$$

- exciton-surface interaction

  $$\mathrm{S_1} \text{ (or } \mathrm{T_1}) + \text{surface} \longrightarrow \text{e (or h)}$$

Interactions of trapped excitons with other entities as well as exciton interactions with traps are also possible. It is worth noting, that triplet-triplet annihilation may result in singlet state generation followed by photoemission called delayed fluorescence.

Organic solids show high values of linear absorption coefficients dependent on the wavelength of incident light. Absorption spectra of organic solids are similar to those measured for organic molecules in solutions, where broadening of sharp absorption peaks related to excitation of single molecules occurs as a result of intermolecular interactions. Moreover, due to Franck-Condon principle and fast relaxation of excited molecules, the energy emitted is lower than the energy absorbed that causes a red shift of fluorescence spectrum with respect to absorption one (see Fig. 2.2), called the Stokes shift [9]. Linear absorption coefficients of organic solids can be determined from absorption spectra of the investigated material as long as Beer-Lambert law, presented below, describing attenuation of light due to absorption is applicable, which means that optical phenomena such as reflectance and interference within this material can be neglected

$$I(x) = I_0 \exp(-\kappa x) \ , \tag{2.2}$$

where I_0, $I(x)$ and κ are the incident light intensity, light intensity at a depth x and linear absorption coefficient of the absorbing material respectively.

The course of photovoltaic phenomenon observed in inorganic solar cells differs a lot from the one observed in devices based on organic materials. The main cause of such dissimilarity is the difference in dielectric constants of these materials. These constants have a major impact on interactions between electric charges that determine the nature of many processes taking place in inorganic and organic materials. In case of inorganic materials absorption of light leads to a creation of a weakly-bound electron-hole pair called the Wannier-Mott exciton. In such pair electron and hole are separated from each other by a relatively large distance, as great as few lattice constants, and attract each other very weakly. Therefore, such excited state dissociates easily and as a result an electron is promoted to the conduction band while a hole remains in the valence band. In such a way free charge carriers are photogenerated. As already mentioned, in contrast to inorganic materials, interaction between organic molecules does not lead to creation of valence and conduction bands in a solid phase. Instead, levels or narrow bands dependent on positions of HOMO and LUMO levels are created. Moreover, dielectric constants of organic materials are low and the screening lengths are large, hence electron-hole pairs photogenerated in these materials are strongly bound by Coulombic attraction. These bound charge carriers are very close to each other and usually they reside at the same molecule. Such excited states are called Frenkel excitons and their binding energy, which is the energy needed to separate charge carriers forming an exciton, can be as high as 1 eV, which is much greater than thermal energy. Frenkel excitons are then electrically neutral mobile quasi-particles. Their motion can be described using macroscopic diffusion model [15] that will be discussed in the next chapter. When an exciton gets to the interface with another material it experiences a different environment and its nature changes since it involves an interaction between two different molecules, namely a donor molecule and an acceptor molecule and an excited complex, termed an exciplex, is formed [13]. Partial separation of charge carriers at the interface, which is an intermediate step in free charge carrier generation process, leads to creation of a polaron pair, also known as a charge transfer (CT) exciton. In this case electron resides at the acceptor molecule while hole at the adjacent donor molecule and their mutual attraction has to be overcome in order to complete the exciton dissociation process. Moreover, a free charge carrier in organic materials often causes distortion of its surroundings and such pair, i.e. a hole or an electron and distortion of its surrounding, is called a polaron. Thus, charge transport from one molecule to another brings about deformation of both molecules, which requires some energy called the reorganization energy and as a result charge transport in organic materials is hampered. Excited states and polarons mentioned above are schematically pictured in Fig. 2.3.

Chapter 3

Photovoltaic phenomenon in organic materials

3.1 First reports and major discoveries in the field of organic photovoltaics

Although first reports on photoelectric properties of organic materials were published in 1906 by Pochettino, who studied photoconductivity of anthracene crystals, intensive research regarding this material was started several decades later - in the mid of the 20th century. Nevertheless, the first organic compounds used in the field of organic photovoltaics (OPV) were porphyrins (Ps) and phthalocyanines (PCs) [16] - groups of materials that comprise such biologically important molecules as haem (haemoglobin component) and chlorophylls. Thanks to a broad range of advantages porphyrins and phthalocyanines still attract considerable attention. In 1982 the first polymer, namely (polyacetylene), was used as the active component of the solar cell. Until 1986 all investigated solar cells incorporated only one organic material and their performance was rather poor. That is why introduction of a bilayer donor/acceptor solar cell concept based on a planar heterojunction of two organic materials made by Tang in 1986 was a real milestone in the field of OPV. The first bilayer cell reported by Tang was based on a copper phthalocyanine (CuPc)/perylene dye (PV) junction and showed 1%

power conversion efficiency and a fill factor of 0.65 under simulated AM2 illumination [17]. Another incontestable breakthrough was made in 1992 by Heeger and Sariciftci, who discovered an ultrafast photoinduced electron transfer from a conjugated (conducting) polymer to a buckminsterfullerene molecule (C_{60}). Due to the fact, that charge transfer from the excited polymer state to a fullerene molecule takes place on a picosecond time scale, and thanks to low temperature metastability of the charge-separated state in such composite polymer/fullerene films, photogeneration of charge carriers can be realized with almost 100% efficiency [18]. At the time Heeger and Sariciftci reported on photoinduced charge transfer, they proposed a novel solar cell architecture - bulk heterojunction (BHJ) solar cell, that they patented in 1994. This discovery boosted the research on organic photovoltaics and paved the way toward high efficiency organic solar cells produced by simple coating techniques. Nowadays, majority of organic solar cells is based on a bulk heterojunction of two organic materials, mainly various polymers, like polytiophenes or polyphenylenevinylenes, and fullerene derivatives, such as PCBM ([6,6]-phenyl-C61-butyric acid methyl ester). When Heeger and Sariciftci were introducing their new outstanding concepts another crucial development in the field of organic photovoltaics was made. Namely, in 1991 Michael Grätzel and Brian O'Regan presented their innovative concept of dye-sensitized solar cells (DSC), that were hybrid solar cells based on a junction of a titanium dioxide and an organic dye, that showed 7.1-7.9% efficiency and relatively high stability under simulated solar light [19]. In 2009, Miyasaka et al. used organolead halide perovskite materials, namely $CH_3NH_3PbBr_3$ and $CH_3NH_3PbI_3$, as sensitezers in dye-sensitized solar cells and though they reached efficiencies lower than 4%, few years later solar cells utilizing organolead halide perovskite materials achieved efficiencies exceeding 15% [20] and a new group of cells - perovskite solar cells was distinguished. One of the next sections provides some insight into the working principle of cells of basic architectures.

3.2 Performance of solar cells

Performance of all solar cells is usually described by a set of parameters extracted from the current-voltage curve (see Fig.3.1), among which, short-circuit

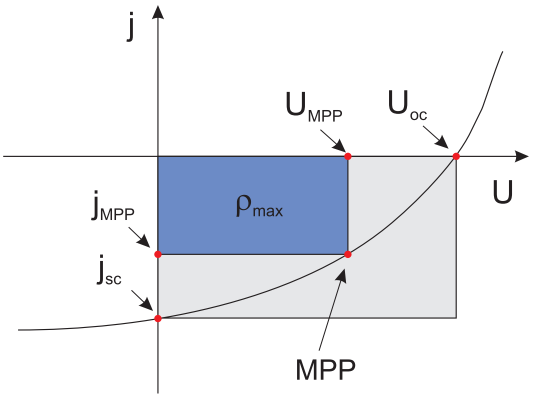

Figure 3.1: Current density vs. voltage for an illuminated cell: j_{sc} - short-circuit current density, U_{oc} - open-circuit voltage, MPP - maximum power point, j_{MPP} - current density at the MPP, U_{MPP} - voltage at the MPP, ρ_{max} - maximum delivered power density.

current J_{sc}, open-circuit voltage U_{oc}, fill factor FF and energy conversion efficiency η seem to be the most important ones. The open-circuit voltage is the voltage developed between the electrodes in the absence of electric current flow. In inorganic p-n solar cells this parameter origins from the quasi-Fermi level splitting observed for electrons and holes under illumination [21]

$$eU_{oc} = {E_F}^n - {E_F}^p, \tag{3.1}$$

where ${E_F}^n$ and ${E_F}^p$ refer to the position of the quasi-Fermi level of electrons and holes respectively. It is believed, that in case of organic D/A junction solar cells maximum value of the open-circuit voltage is determined by the energy offset between donor's HOMO $(HOMO_D)$ and acceptor's LUMO $(LUMO_A)$ positions [22]

$$e{U_{oc}}^{max} = LUMO_A - HOMO_D \ , \tag{3.2}$$

however values of eU_{oc} obtained experimentally are usually few tenths of eV lower than this HOMO/LUMO offset [23, 24]. Another crucial parameter describing the performance of a solar cell is the short-circuit current, that is the current flowing through the circuit when both electrodes are brought into direct contact and no external voltage is applied $(U = 0)$.

Current obtained from a unit area of a cell is called current density j. Product of the photocurrent density and applied voltage gives the power density ρ, i.e. power extracted from a unit area of a cell at a certain external load

$$\rho = jU \ . \tag{3.3}$$

The point on the current-voltage curve for which maximum value of power density ρ_{max} is obtained is called the maximum power point (MPP). Its coordinates are denoted by j_{MPP} and U_{MPP}. The value of ρ_{max} divided by the product of j_{sc} and U_{oc} gives another crucial parameter termed the fill factor (FF)

$$FF = \frac{\rho_{max}}{j_{sc}U_{oc}} = \frac{j_{MPP}U_{MPP}}{j_{sc}U_{oc}} \ . \tag{3.4}$$

High values of FF characterize those cells which are able to deliver power density close to its maximum value in a broad range of external loads. Therefore, high fill factors characterize devices capable of efficient charge carrier collection even at low electric fields, i.e. when voltage approaches the value of U_{oc}. Knowing maximum power density or values of fill factor, short-circuit current, open-circuit voltage and the illumination intensity W one can calculate the most important parameter characterizing the performance of a solar cell from the practical point of view, i.e. energy (power) conversion efficiency η

$$\eta = \frac{\rho_{max}}{W} \ , \tag{3.5}$$

where W is given in Watts per cm^2. According to Eq. 3.4 the energy conversion efficiency can be written as follows

$$\eta = FF\frac{j_{sc}U_{oc}}{W} \tag{3.6}$$

and that is why these four parameters, namely η, FF, j_{sc} and U_{oc} are commonly used to describe performance of solar cells. When photovoltaic cells are illuminated with monochromatic light the intensity of the latter is often measured in the number of photons incident on a unit area in a unit time. Such illumination intensity is usually denoted by I_0. In such case, the energy conversion efficiency is calculated form the following formula

$$\eta = FF\,\frac{j_{sc}\,U_{oc}}{h\nu I_0} \ , \tag{3.7}$$

where h stands for Planck's constant, while ν is the frequency of incident light. The ability of a solar cell to convert light of a certain wavelength into electricity can also be characterized by quantum efficiency (QE). The number of electrons flowing in the external circuit divided by a number of incident photons gives external quantum efficiency (EQE) also known as incident photon to current efficiency $(IPCE)$

$$EQE = IPCE = \frac{\text{number of collected electrons}}{\text{number of incident photons}} \,. \tag{3.8}$$

Substitution of the number of incident photons in the equation above with the number of absorbed photons changes external quantum efficiency into internal quantum efficiency (IQE)

$$IQE = \frac{\text{number of collected electrons}}{\text{number of absorbed photons}} \,. \tag{3.9}$$

Quantum efficiencies depend on many processes, such as exciton diffusion and dissociation, along with charge carrier transport, recombination and extraction, taking place in all layers and interfaces forming a solar cell.

3.3 Shockley equivalent circuit

Although mechanisms of charge carrier generation in organic solar cells differ from the ones that govern this process in inorganic devices it was shown that in a limited range of voltage analytical solution of dark current-voltage dependence for organic solar cells is consistent with the Shockley equation [25, 26], so the same equivalent circuit, called the Shockley equivalent circuit (SEC), can be used for both types of cells. Shockley equation and simple or modified SEC were used in numerous theoretical and experimental works regarding organic solar cells of different architectures [25–37], and good agreement between numerical or analytical models for the current-voltage relation and experimental data was obtained. In the ideal case an equivalent circuit would have only two constituents connected in parallel: a photocurrent source and a diode. In the absence of light the only current flowing through such circuit would be the dark current of the diode J_d resulting from thermal generation of free charge carriers within the cell and thermal injection from electrodes given by the Shockley equation

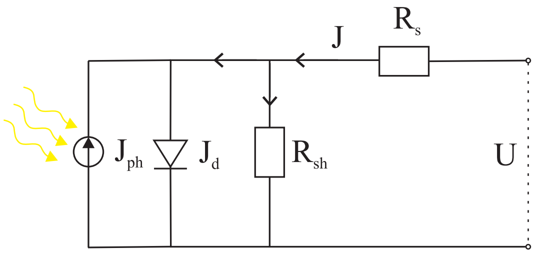

Figure 3.2: Shockley equivalent circuit of a real solar cell consisting of a photocurrent source, a diode and two resistors; U-applied voltage, J- current flowing through the circuit, J_{ph}- generated photocurrent, J_d - dark current , R_s - series resistance, R_{sh} - shunt resistance.

$$J_d = J_0 \left[exp \left(\frac{eU}{mkT} \right) - 1 \right] , \tag{3.10}$$

where J_0 is the saturation current, e denotes the elementary charge and m stands for the diode ideality factor. J_0 depends on properties of materials forming the cell and on temperature. Under illumination current flowing through the circuit is a sum of the dark current J_d and the photocurrent J_{ph} that flow in opposite directions, so the net current J is

$$J = J_d - J_{ph} \ . \tag{3.11}$$

The equation given above describes the behavior of an ideal solar cell in the absence of loss mechanisms and therefore rather impossible to achieve. In real photovoltaic devices losses arising from shorting and presence of potential barriers at contacts are impossible to avoid. That is why a series resistance R_s and a shunt (parallel) resistance R_{sh} have to be introduced to the equivalent circuit of a solar cell in order to describe the current - voltage relation in the case of a real device. The series resistance R_s of a cell originates from all ohmic losses, like non-ohmic electrode contacts, whereas shunting, represented by R_{sh}, is connected with charge carrier recombination. The smaller the series resistance and the greater the shunt resistance are the better. Current J flowing through the cell under illumination is derived from the Kirchhoff's laws applied to the equivalent circuit of a real solar cell shown in Fig. 3.2. In this case, due to losses, voltage V applied to the diode is lower than U

$$V = U - JR_s \tag{3.12}$$

and, for the same reason, the net current is

$$J = J_d + \frac{U - JR_s}{R_{sh}} - J_{ph} \ , \tag{3.13}$$

Therefore, the dark current flowing through the diode is

$$J_d = J_0 \left\{ exp\left[\frac{e(U - JR_s)}{mkT} \right] - 1 \right\} , \tag{3.14}$$

so the current - voltage relation for the equivalent circuit is expressed by the following equation

$$J = \frac{R_{sh}}{R_{sh} + R_s} \left\{ J_0 \left[exp\left(\frac{e(U - JR_s)}{mkT} \right) - 1 \right] + \frac{U}{R_{sh}} - J_{ph} \right\} \ . \tag{3.15}$$

Analytical expression of such form was obtained by Foster et al. [26] who considered a drift-diffusion model for a bilayer organic D/A solar cell. A perfectly symmetric device with no pinhole defects, no minority carriers and Shockley-Read-Hall (SRH) recombination was regarded. Thus, the ideality factor of the diode was equal to 2, while shunt resistance was infinite. Authors implied that consideration of pinholes and minority carriers would require the introduction of a nonlinear shunt resistance dependent on the applied potential. It is noteworthy, that also other parameters given in this equation may not be constant. Vandewal et al. [27], who studied bulk heterojunction solar cells, assumed that the saturation current may depend on the applied voltage and charge density. Also Fonash [38], who presented analytical approach to analysis of excitonic cells, stated that diode ideality factor and saturation current may show illumination and voltage dependence. According to Turek [39], series resistance of a cell is not a constant parameter, but it depends on current flowing through the cell and illumination conditions. Rand et al. [35], who modeled organic semiconductor heterojunction energy level offsets, assumed that the photogenerated current is a function of electric bias, while shunt resistance decreases with increasing light intensity as a result of photoconductive charge generation that leads to the drop in the efficiency of a cell. Similar conclusion regarding shunt resistance was drawn by Waldauf et al. [36], who described this resistance as a function free charge carrier concentration that changes upon illumination.

3.4 Organic solar cells architectures

There are four main types of organic and hybrid solar cell concepts, i.e. single-layer, bilayer, bulk heterojunction and dye-sensitized solar cells. Hybrid devices incorporate both - organic and inorganic - materials in the active layer and, just as perovskite solar cells, they may have various architectures. A short overview of main types of architectures, as well as, some basics of their operation are given below:

- **Single layer organic solar cells**
  In this kind of cells a thin organic layer is placed between two electrodes of different work functions. One of electrodes, namely the high work function (HWF) or the low work function (LWF) electrode, has to be transparent or at least semi-transparent to provide sufficient light penetration. Usually transparent conducting oxides (TCOs), like ITO (indium tin oxide), are employed in the role of a transparent electrode.If a photovoltaic device is based on only one organic layer charge carrier generation occurs mainly via exciton dissociation at the organic material/electrode interface (Fig. 3.3). That means, this interface is an active junction. Creation of such junction in single layer devices is observed when a rectifying (Schottky) contact is formed between an organic material and one of electrodes. Moreover, it is crucial to have only one rectifying contact within the cell. The other one should remain

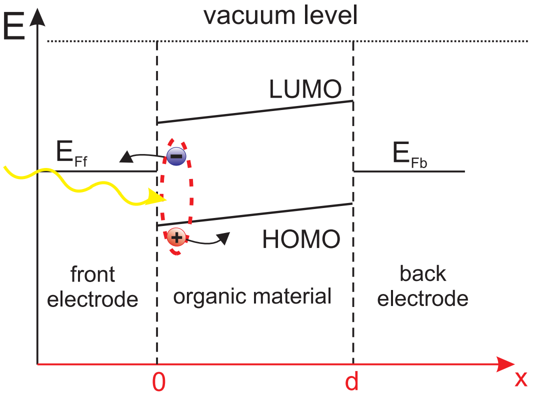

Figure 3.3: Exciton dissociation at the electrode/organic material interface resulting in injection of a hole into organic material. E - energy, x - space coordinate.

ohmic to provide efficient charge carrier collection and to avoid creation of two competing active junctions of opposite polarity. Creation of such competing active junctions leads to reduction in U_{oc} and, as a consequence, to the decrease in the performance of a cell. Apart from generation of free charge carriers taking place in the vicinity of the metal/organic material interface, generation of free charge carriers in the bulk is possible, but far less efficient.

A very serious problem affecting all kinds of organic solar cells is a very short exciton diffusion length *L*, originating from short lifetime of singlet excitons and low diffiusivities of triplet excitons (resulting from the short range Dexter energy transfer process) [40]. Values of the diffusion length typical for organic materials range from few nanometers in case of polymers and other disordered systems [1,40,41] to few dozens of nanometers for highly-ordered structures [42]. For that reason, not all excitons are able to reach the active interface within their lifetime. This is a so-called exciton diffusion bottleneck [1]. Due to this drawback the thickness of organic materials incorporated into solar cells has to be carefully chosen to ensure a reasonable compromise between sufficient light absorption and the distance excitons have to travel to reach the active interface.

- **Bilayer organic solar cells**

  These cells, originally called two-layer solar cells [17], are composed of two planar thin films made of different organic materials sandwiched between dissimilar electrodes. Application of two organic materials instead of one brings about an increase in the efficiency of the cell, since exciton dissociation occurring at junctions of some organic materials is much more probable than exciton dissociation at organic material/electrode interfaces. Molecules donating and accepting electrons are called donors (D) and acceptors (A), respectively. When excitation takes place in the donor material (see Figure 3.4) exciton dissociation at a D/A junction is very efficient providing the energy offset between LUMO levels of materials forming that junction is greater than the exciton binding energy E_b^{ex} [43] :

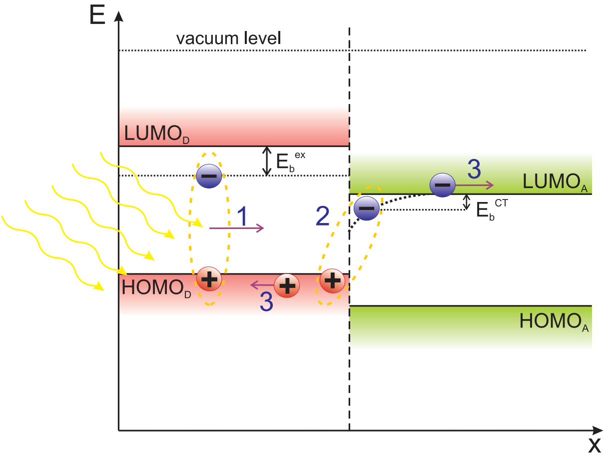

Figure 3.4: Charge carrier photogeneration at a junction of two organic materials for which efficient exciton dissociation is observed when excitation occurs in a donor material: 1 - excitation of a molecule as a result of light absorption followed by exciton diffusion toward a D/A junction, 2 - charge-transfer state formation and dissociation into free charge carriers, 3 - migration of free charge carriers through HTL and ETL toward respective electrodes, E - energy, x - space coordinate.

$$LUMO_D - LUMO_A > E_b^{ex} \; , \tag{3.16}$$

where $LUMO_D$ and $LUMO_A$ stand for the positions of the donor and acceptor LUMO levels respectively.

If the condition given above is fulfilled, electron transfer from the donor to the acceptor molecule should be energetically a downhill process of high probability. One must bare in mind, that electron transfer occurs at the D/A interface, so electron and hole are initially located at two adjacent molecules, which means that initial separation distance is not grater than 1 nm [43]. Thus, these charge carriers still attract each other quite strongly, and so, geminate recombination is very probable. Such bound electron-hole pair is called a charge-transfer (CT) state or a charge-transfer exciton, while the energy of the above mentioned Coulomb attraction is termed a charge-transfer state binding energy (E_b^{CT}) and it is usually greater than thermal energy, so it constitutes an important barrier in the charge separation process. That is why the condition for efficient and complete exciton dissociation given by Eq. 3.16 has to be modified to the following form [44]:

$$LUMO_D - LUMO_A > E_b^{ex} + E_b^{CT} \ . \tag{3.17}$$

Analogical condition for complete exciton dissociation can be written for excitons generated in the acceptor layer and in this case relative positions of HOMO levels determine the effectiveness of the dissociation process.It is worth noting (Fig. 3.4) that the energy of a charge separated (CS) state is higher than the energy of a CT state formed at the junction of two organic materials, so the process of CT exciton dissociation should be a process that is additionally activated, for instance thermally, or it may be a field-dependent process [45]. Moreover, despite intensive research run in the field of organic solar cells comprising D/A junctions it is still unclear what kind of excitons is the main precursor of free charge carriers generated at the junction of two organic materials. There are at least few possible pathways leading to creation of these free charge carriers: a) direct dissociation of excited donor D^* or acceptor A^* manifolds, b) dissociation of a hot CT state and c) dissociation of a vibrationally relaxed CT state. Although D^*, A^* and hot CT states possess higher energy than a thermalized CT exciton, Vandewal et al. [46], who have recently investigated various BHJ solar cells, shown that efficiency of charge carrier generation and charge extraction is the same for all these kinds of excitons and that the excess energy of D^*, A^* and hot CT excitons can not be used to increase charge carrier generation efficiency. Authors have also pointed out, that the binding energy of a thermalized CT state is not always greater than kT and there are such donor/acceptor systems in which CT excitons are so delocalized that internal quantum efficiency is as high as 90% and it does not depend on the applied field.

After separation at the D/A junction, free charge carriers are driven to respective electrodes by the built-in electric field and concentration gradient. Donor layer is a hole transporting layer (HTL), whereas acceptor layer is an electron transporting layer (ETL), so to provide efficient charge transport the donor material should be a good hole conductor, whereas the acceptor material should be a good electron conductor. Electrodes should form Ohmic contacts with organic materials they are in touch with to ensure productive charge collection. Furthermore, creation of Schottky contacts instead of Ohmic ones would lead to the presence of additional active interfaces competing with the D/A junction, and as a result, performance of a cell would be hampered. According to Lloyd et al. [47], theoretical and experimental data show that the fill factor of a cell, that is dependent on recombination rate, is the greatest when the ratio of charge carrier mobilities in donor and acceptor layers approaches unity:

$$\frac{\mu_p}{\mu_n} \rightarrow 1 \,, \tag{3.18}$$

where μ_p denotes the hole mobility in a HTL, while μ_n is the electron mobility in an ETL. On the other hand, authors point out, that results of research run by Peumans et al. on exciton dissociation probability show, that the probability, that electron and hole will remain separated after exciton dissociation, decreases when condition stated by equation 3.18 is fulfilled. Moreover, authors suggest that semiconductors with high charge carrier mobilities $(\mu \simeq 10^{-5}\mathrm{cm}^2\mathrm{V}^{-1}\mathrm{s}^{-1})$ guarantee exciton dissociation under illumination of 1000 W/cm^2, while further mobility enhancement is not desirable due to decrease in the open-circuit voltage and drop in power conversion efficiency introduced by this enhancement as it leads to lower concentration of charge carriers close to the D/A junction. In contrast, Street [48] infers that high mobilities do not lead to low open-circuit voltages, since at the condition of the open-circuit there is no current flow and charge carriers are not collected at the electrodes. Therefore, positions of the quasi-Fermi levels of electrons and holes that determine the value of U_{oc} depend on recombination not on charge extraction. Hence high charge carrier mobilities foster high values of FF.

As one can see, processes involved in the photovoltaic phenomenon in organic systems are very complex and, despite intensive research run in this field, still not fully understood [43].

- **Bulk heterojunction organic solar cells**

  Since exciton dissociation is very efficient at a junction of two organic materials and exciton lifetime is relatively short, the larger the interface area of these materials and the shorter the path to this interface are the better the performance of a cell is. Hence, bulk heterojunction solar cells are based on a blend of donor and acceptor materials, so that the active interface exists practically within the whole bulk of a device - D/A blend forms the active layer in which domains of both materials are present. Hence, greater number of excitons is able to reach the D/A interface within their lifetime. Nevertheless, exciton dissociation into free charge carriers is just the first step toward photovoltaic action. One must remember, that these newly created free charge carriers have to travel through hole and electron transporting materials, i.e. donor and acceptor, to be collected at respective electrodes. Thus, donor and acceptor phases should form interpenetrating networks with percolation paths. Otherwise, electrons and holes will recombine at the end of the dead-end domain making no contribution to the total current (Fig. 3.5A). Moreover, unfavorable electron-hole recombination is also unavoidable when the donor material is in contact with the cathode or when the acceptor material is in contact with the anode. These two phenomena are very important loss mechanisms in BHJ solar cells [49, 50]. The latter may be eliminated by the introduction of a thin planar layer of the donor material directly before the deposition of the D/A blend and a thin film of the acceptor material right on the top of this blend. The first problem is much more complicated, since the morphology of the D/A blend is not so easy to control. An ideal ordered structure of a BHJ solar cell concept is presented in Fig. 3.5B. A very interesting and relatively simple way to produce laterally ordered polymer-polymer bulk heterojunction solar cells was presented by Lipomi et al. [51].

- **Tandem solar cells**
  Tandem solar cells are multijunction solar cells of improved efficiency overcoming some of the limitations of single junction cells [52]. They are based on two or more planar or bulk donor/acceptor heterojunctions connected in series via special interconnection layers (ICLs) allowing for selective recombination of free charge carriers. Due to partial recombination of free charge carriers at ICLs current flowing through such stack of junctions is lower than the one flowing through a single junction cell but the resultant open-circuit

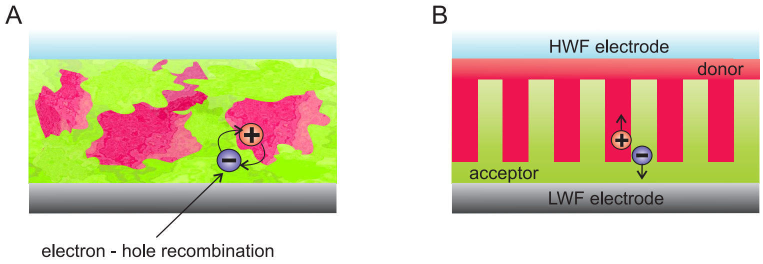

Figure 3.5: (A) Electron-hole recombination at the edge of two domains in the BHJ solar cell with no percolation paths, (B) concept of an ordered BHJ solar cell structure

voltage and thus efficiency of a tandem cell is much greater than that of a single junction one. Usually, in case of tandem cells comprising two sub-cells two different donor materials, mainly polymers, with complementary absorption spectra and minimal absorption overlap are used as donor materials to harvest light from a broad spectral range. A wide-bandgap material is placed in the bottom cell, while a low-bandgap one is a part of the top cell [53]. Fullerenes and their derivatives, such as $PC_{71}BM$, are the most common acceptor materials used for both sub-cells. Another approach to realization of a tandem structure is connection of two identical sub-cells of high internal quantum efficiency [54, 55]. Such structures are called homo-tandem solar cells. The idea behind fabrication of such homo structures is to absorb more light via introduction of additional sub-cell not exceeding the optimal film thickness of active layers. Efficiencies of organic tandem solar cells already exceed 11% [55].

- **Dye-sensitised solar cells**
  Dye-sensitized solar cells (DSCs), also called Grätzel cells after the name of one of their inventors - Michael Grätzel, are hybrid photo-electrochemical systems that employ organic and inorganic components in the active layer (Fig. 3.6). Their efficiencies exceed 12% [56], which is high enough to compete with conventional inorganic solar cells. In DSCs a nanoparticle layer of a wide band gap semiconductor, like titanium dioxide or zinc oxide, is covered (sensitized) with an organic dye. Such layer is brought into contact with electrolyte containing a redox couple, usually iodide/tri-iodide, sandwiched between electrodes and sealed well to avoid leakage. Organic molecules

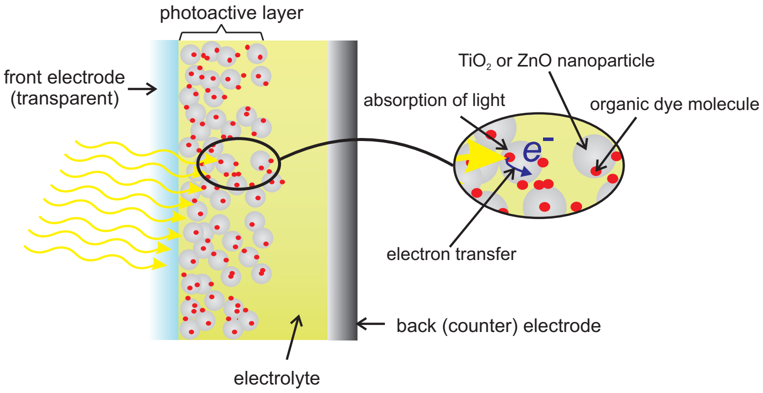

Figure 3.6: Dye-sensitised organic solar cell structure.

absorb light from the visible range, while wide band gap inorganic semiconductors utilize UV light. A nanoparticle layer is preferred over a homogenous planar layer because it provides larger active area. Photoexcitation of an organic molecule results in a fast electron transfer from the dye molecule to conduction band of the inorganic semiconductor. Ground state of the dye molecule is restored thanks to electron injection from the electrolyte to the oxidized dye molecule, during which iodide changes into triiodide $(3I^- - 2e^- \rightarrow I_3^-)$ that is subsequently reduced at the counter electrode by electrons flowing through the external circuit. The difference between the Fermi level of electrons in the solid and the redox potential of the electrolyte determines the value of generated photovoltage [57]. Grätzel cell is the only type of photovoltaic devices in which charge photogeneration and charge transport are separated - electric charge is transported not through organic material used for light harvesting, but through electrolyte and nanoparticle layer. That is a great advantage of DSCs, since optimization of light absorbing and charge transporting materials can be done independently. This reduces demands on purity of materials and enables usage of great variety of absorbers, as well as, transporting materials [56]. Furthermore, for the former reason, these materials can be deposited by simple and cheap coating techniques. All these factors account for relatively low price of this type of solar cells. Nevertheless, there are some disadvantages hampering commercialization of DSCs. Thermal instability of liquid electrolytes and problems with sealing are some of them. Moreover, electrolytes are based on volatile solvents [58], that are dangerous to human health and the environment, so any leakage is unacceptable. Next problem is the corrosives of a I^-/I_3^- redox couple [59]. Some attempts to exchange liquid electrolytes with solid state ones, like p-type inorganic semiconductors, organic hole transporting materials or solvent-free polymer electrolytes, have been made. In general, solid-state DSCs show worse performance than those containing liquid electrolytes, however recent research run by Grätzel et al. on hybrid solar cells utilizing polymeric hole conductors resulted in development of solid-state DSCs with 12% efficiency [60].

3.5 Buffer layers

For many reasons organic materials rather do not form Ohmic contacts with electrodes. Therefore, to avoid creation of extraction and injection barriers and to enable efficient charge collection and selectivity of the contact thin layers of various materials are introduced between the electrodes and components of the active layer. Such interlayers, called buffer layers, are also added to control wettability and compatibility of the electrode/organic material contact [61]. If such layers are introduced between the anode and the active layer they are called anodic buffer layers. Analogically, interlayers placed between the active layer and the cathode are named cathodic buffer layers. The most common anodic buffer layers are thin layers of PEDOT:PSS ([poly(3,4-ethylenedioxythiophene) poly(styrenesulfonate)]), MoO_3 (molybdenum oxide) and V_2O (vanadium oxide) [62,63], whereas thin films of BCP (bathocuproine), BPhen (bathophenanthroline) as well as Alq_3 (tris(8- hydroxyquinolinato)aluminium), TiO_2 or ZnO [6,61,64–66] are examples of cathodic buffer layers. New materials, like graphene oxide, have also been employed as interlayers [67]. Properties of such layers and their influence on the performance of solar cells depend on many factors, like the material they are made of, thickness of the layer, methods of fabrication and other materials they are in touch with. For example, PEDOT:PSS is a good p-type conductor, so it enhances collection of holes at the anode. Moreover, it is believed to smooth the surface of ITO anode out which helps to prevent shorting. It is also claimed that the presence of PEDOT:PSS enhances adhesion of organic layers [64]. However, apart from other disadvantages, this material is hygroscopic and slightly acidic, which results in introduction of water into the active layer and corrosion of the ITO electrode that lead to degradation of a cell and to deterioration of its performance [62, 64, 68, 69]. Cathodic buffer layers are often called the exciton blocking layers, since these materials have high values of energy band gap and high values of ionization potential, so they prevent diffusion of excitons to the cathode. Excitons are rather reflected from these layers back to the active junction where they can dissociate into free charge carriers [65].

Since the number of materials that can be used as buffer layers is quite large and they show different properties depending on the choice of other components of a cell selection of a suitable buffer layer and its optimization is not a trivial issue. Details on properties of buffer layers used in the course of this research and their influence on the performance of investigated cells will be given in the experimental part of this thesis.

3.6 Photovoltaic phenomenon in solar cells utilizing perfluorophthalocyanines

There are not many reports on photovoltaic properties of perfluorophthalocyanines though their n-type character and insusceptibility to ambient air have been confirmed almost two decades ago [3, 4]. In 2003 Wróbel studied photoelectric properties of F_{16}ZnPc as well as other phthalocyanines and porphyrins incorporated into photoelectrochemical cells and shown the correlation between the dye molecular structure and dye ability for generation of photocurrent in the investigated cells [5]. In 2007 F_{16}CuPc was used by Jiang et al. [70] as an electron acceptor material in planar donor/acceptor solar cells utilizing para-sexiphenyl (p-6P) as a donor material. As a result, cells of improved stability but relatively poor performance, attributed to high value of series resistance originating from contact resistance and low free charge carrier mobility in the donor layer, were fabricated. Authors assigned the degradation of the cell, that was stored in ambient air without encapsulation, to instability of PEDOT:PSS buffer layer and pointed out that F_{16}CuPc was a promising electron accepting material. The same conclusion was drawn by Yang et al. [71], who investigated photovoltaic effect in F_{16}CuPc/SubPc (boron subphthalocyanine chloride) cells. Relatively good overall performance and stability, with a power conversion efficiency of 0.56% after optimization of the thickness of the phthalocyanine layer was obtained, but small contribution of excitons created in this layer to photocurrent generation was observed. A different approach was taken by Song et al. [8] who used two n-type organic semiconductors, namely F_{16}ZnPc and C_{60}, and fabricated a new n-n type planar heterojunction solar cell. The structure of this cell was ITO/F_{16}ZnPc/C_{60}/Alq_3/Ag, and on the basis of the direction of the current flow it was inferred that photogeneration of free charge carriers in this system was not a result of exciton dissociation at the F_{16}ZnPc/C_{60} junction but it followed from recombination of electrons from excitons generated in the phthalocyanine layer with holes from excitons created in the fullerene layer taking place at this junction. Therefore, such solar cells were called recombination solar cells. Efficient operation of these cells requires simultaneous generation of excitons in both organic layers and their subsequent recombination during which half of the charge carriers of excitons is lost, while the other half contributes to the current flow. Relatively low value of the photocurrent noted for the investigated cells was attributed to very poor hole mobility in the F_{16}ZnPc layer. The same concept of n-n organic solar cells was applied by Yang et al. [72] who studied the course of photovoltaic phenomenon in cells based on the C_{60}/F_{16}CuPc heterojunction of a conventional ITO/MoO_x/ C_{60}/F_{16}CuPc/BCP/Al and an inverted ITO/BCP/F_{16}CuPc/C_{60}/MoO_x/Al structure. Direction of the current flow and sublinear dependence of the short-circuit current on light intensity observed for both of these structures lead to a conclusion that in this case conventional exciton dissociation at the junction of organic semiconductors was responsible for free charge carrier generation. F_{16}CuPc played the role of an acceptor, while C_{60} of a donor material. Similarly to F_{16}CuPc/SubPc cells, small contribution of the phthalocyanine acceptor layer to photocurrent generation was observed and attributed to insufficient for acceptor exciton dissociation HOMO levels offset of only 0.2 eV. Recently, Zhang et al. [7] investigated solar cells of conventional and inverted architectures based on the C_{60}/F_{16}ZnPc junction with ITO and Al electrodes and different buffer layers affecting the electrode work functions and hence determining the direction of the built-in field. As a result, recombination and dissociation solar cells for both aforementioned architectures were obtained. Free charge carrier generation as a result of exciton recombination was proved by superlinear dependence of photocurrent on light intensity and the direction of the current flow. It was shown that exciton dissociation and recombination mechanisms of free charge carrier generation coexist at the C_{60}/F_{16}ZnPc junction but exciton dissociation is more efficient. It was also shown that in case of the dissociation devices both mechanisms contribute to the current generation, while in case of recombination solar cells only free charge carriers generated via exciton recombination may be collected, since the inner electric field directs charges generated via exciton dissociation back to the active interface where they are lost due to recombination. Zinc perfluorophthalocyanine was also used by Signerski et al. [73, 74] in hybrid solar cells based on the planar CdTe/F_{16}ZnPc and ZnTe/F_{16}ZnPc heterojunctions. In these cases short-circuit current and open-circuit voltage action spectra revealed two mechanism of free charge carrier generation, i.e. excitation of the phthalocyanine layer followed by exciton dissociation at the inorganic semiconductor/F_{16}ZnPc junction and band to band transitions in CdTe and ZnTe layers. Light intensity dependence of j_{sc} and U_{oc} indicated that trap-assisted recombination of free charge carriers at the investigated heterojunction was a dominant recombination process.

Chapter 4

Theoretical description of photovoltaic phenomenon in single- and bilayer systems

4.1 Photogeneration of free charge carriers at interfaces

Photogeneration of free charge carriers in organic systems is a multistage process and its first step is generation of excitons resulting from light absorption. Afterward, excitons diffuse toward the active interface where they may dissociate into free charge carriers or CT states. In case of one-dimensional systems (Fig. 4.1) concentration of excitons along an organic material $S(x,t)$ can be evaluated from the following continuity equation

$$\frac{\partial S}{\partial t} = G_S - R_S - D\frac{\mathrm{d}^2 S(x)}{\mathrm{d}x^2} \; , \tag{4.1}$$

where G_S is a generation term dependent on light intensity, while R_S is a recombination term, while the last term accounts for exciton diffusion. If we take a singlelayer cell into consideration, assume that Lambert-Beer law holds for our system and the cell is illuminated with monochromatic light, while excitons recombine only in a monomolecular manner we will obtain the following one-dimensional diffusion equation for excitons in a steady state, i.e. when $\partial S(x,t)/\partial t = 0$

$$I_0 \kappa e^{-\kappa x} - kS(x) + D\frac{\mathrm{d}^2 S(x)}{\mathrm{d}x^2} = 0 \; , \tag{4.2}$$

in which k is the exciton annihilation rate equal to the reciprocal of exciton lifetime τ. Choice of boundary conditions determines the final solution of this equation, therefore, if we assume that

1. excitons are quenched at the illuminated front electrode/organic material interface with exciton annihilation velocity s,
2. the thickness of absorbing layer d is much greater than exciton diffusion length L
3. absorption of light is strong, so that $d \gg \kappa^{-1}$,

boundary conditions given below can be applied to Eq. 4.2

$$D\frac{\mathrm{d}S(x)}{\mathrm{d}x}|_{x=0} = sS(0) \quad \text{and} \quad S(d) = 0 \ . \tag{4.3}$$

Under such conditions the following equation expresses the concentration of excitons at the illuminated interface, i.e at $x = 0$

$$S(0) = \frac{I_0}{s(1 + 1/\kappa L)(1 + D/sL)} \ , \tag{4.4}$$

where $L = \sqrt{D\tau}$. In this case, as it will be proved in section 4.3.2, the short-circuit current density can be calculated as a product of the elementary charge e, exciton annihilation velocity s, exciton - electron conversion efficiency at the electrode φ_{diss} and concentration of excitons at the illuminated active interface $S(0)$

$$j_{sc} = -e\varphi_{diss}sS(0) = \frac{e\varphi_{diss}I_0}{(1 + 1/\kappa L)(1 + D/sL)} \ . \tag{4.5}$$

In case of bilayer systems, in which exciton dissociation into free charge carriers can occur at anode/donor, donor/acceptor and acceptor/cathode interfaces, proper set of boundary conditions has to be introduced to find the correct solution of the continuity equation in each organic layer. If both contacts are Ohmic photogeneration of charge carriers is limited to the D/A junction. However, if excitons dissociating at the D/A junction are not the direct source of free charge carriers and CT states are created at this junction prior to complete electron-hole dissociation, another continuity equation regarding concentration $C(x, t)$ of these intermediate states has to be considered. The following equation regarding the creation of charge transfer states was proposed by Cheyns et al. [30]

$$\frac{\partial C}{\partial t} = G_C + G_L - R_C - Diss_C \ , \tag{4.6}$$

where G_C represents generation of CT states from excitons at the D/A interface, G_L stands for creation of CT states via recombination of free charge carriers (Langevin recombination), while R_C and $Diss_C$ represent the decline in CT concentration as a result of their recombination and dissociation into free charge carriers, respectively. Thus, solution of this equation depends on concentration of excitons at the D/A interface and on concentration of free charge carriers. Another simple model for generation, diffusion and recombination of excitons was used by Stübinger and Brütting [75], who applied the following continuity equation to polymer/$\mathrm{C_{60}}$ and small molecule/$\mathrm{C_{60}}$ cells

$$\frac{\partial S}{\partial t} = g\alpha I_0(1-R)exp(-\alpha x) - \frac{S}{\tau} + D\frac{\partial^2 S}{\partial x^2} - F(x-x_i)S \ . \tag{4.7}$$

Herein g represents internal photon-to-exciton conversion efficiency, $(1-R)$ factor is introduced to account for reflectivity losses, the next two terms refer to monomolecular recombination and diffusion of excitons, while the last term stands for the dissociation of excitons at the donor/acceptor interface located at $x = x_i$. These models do not take into consideration interference effects that should be regarded when thin layers and well reflecting electrodes are considered. A general approach to optical interference effects that can be applied to organic solar cells is the transfer matrix approach. This model was thoroughly described by Peumans, Yakimov and Forrest and used to model optical intensity distribution for a bilayer cell with anodic and cathodic buffer layers [76]. This distribution was then substituted into the exciton diffusion equation in which the exciton generation rate G was not based on Lambert-Bear's law, but given by

$$G = \frac{\lambda}{hc} Q(x) \ , \tag{4.8}$$

where λ denotes the wavelength, h is Planck's constant, c is the speed of light and $Q(x)$ is the time averaged absorbed power equal to

$$Q(x) = \frac{4\pi c \epsilon_0 k n}{2\lambda} |\overline{E}(x)|^2 \ . \tag{4.9}$$

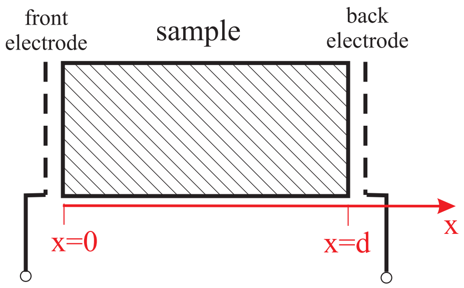

Figure 4.1: Schematic representation of a one-dimensional system.

Herein, n is the refractive index indicating the phase velocity, k stands for the extinction coefficient, while $\overline{E}(x)$ is the total electric field at a position x of a chosen layer given in terms of the electric field of the incident wave that was calculated using the transfer matrix method.

4.2 One-dimensional steady current flow

Current flow originates from electric potential gradient $\nabla\phi(\mathbf{r})$ and/or chemical potential gradient $\nabla\xi(\mathbf{r})$ that results from free charge carrier concentration gradient. Thus, in the lack of electric field and charge carrier concentration gradient, motion of free charge carriers is completely random and so the net current is zero. The sum of electric and chemical potentials is called the electrochemical potential $\eta(\mathbf{r})$

$$\eta_n(\mathbf{r}) = -e\phi(\mathbf{r}) + \xi_n(\mathbf{r}) \ \text{ and } \ \eta_p(\mathbf{r}) = e\phi(\mathbf{r}) + \xi_p(\mathbf{r}) \ . \tag{4.10}$$

Indexes n and p refer to electrons and holes respectively, while $\mathbf{r}$ is a vector describing the position in space. Electrochemical potentials are used to define quasi-Fermi level positions of electrons ${E_f}^n(\mathbf{r})$ and holes ${E_f}^p(\mathbf{r})$ in a material

$${E_f}^n(\mathbf{r}) = \eta_n(\mathbf{r}) \ \ and \ \ {E_f}^p(\mathbf{r}) = -\eta_p(\mathbf{r}). \tag{4.11}$$

Therefore, electric current flow is observed whenever Fermi level gradient is produced, i.e. when $\nabla E_f \neq 0$. If the source of the latter is electric field then the current is called the drift current, whereas diffusion current is the current that is driven by chemical potential gradient.

Lets consider the electric current flow in one-dimensional systems in which currents flow in only one direction, e.g. along the x axis (Fig. 4.1). If both types of carriers are mobile drift current density j_{drift} can be expressed as follows

$$j_{drift}(x) = -en(x)v_n + ep(x)v_p \ , \tag{4.12}$$

where $n(x)$ and $p(x)$ stand for concentration of free (mobile) electrons and free holes respectively, whereas v_n and v_p denote electron and hole drift velocities. If internal electric field F is not too high, then drift velocity is a linear function of the former [77]

$$\overrightarrow{v_n} = -\mu_n \overrightarrow{F} \quad and \quad \overrightarrow{v_p} = \mu_p \overrightarrow{F} \tag{4.13}$$

and the net drift current density flowing through a sample is

$$j_{drift}(x) = eF[n(x)\mu_n + p(x)\mu_p] = \sigma F \ . \tag{4.14}$$

This equation expresses Ohm's law, in which $\sigma = e[n(x)\mu_n + p(x)\mu_p]$ stands for electric conductivity of a material.

Diffusion current density j_{diff} can be derived from Fick's law. Under the assumption of a steady state, i.e. when concentration of charge carriers and hence current density do not change in time, one obtains

$$j_{diff}(x) = eD_n \frac{\mathrm{d}n}{\mathrm{d}x} - eD_p \frac{\mathrm{d}p}{\mathrm{d}x} \ , \tag{4.15}$$

where D_n and D_p denote electron and hole diffusion coefficients, that can be related to mobilities of these charge carriers by Einstein-Smoluchowski relation

$$D = \frac{\mu k T}{e} \ . \tag{4.16}$$

Combination of Eqs. 4.14 and 4.15 gives the total bipolar, i.e. electron and hole, current density j flowing through the sample in a steady state

$$j = j_{drift}(x) + j_{diff}(x) = eF(n\mu_n + p\mu_p) + e\left(D_n \frac{\mathrm{d}n}{\mathrm{d}x} - D_p \frac{\mathrm{d}p}{\mathrm{d}x}\right) \ . \tag{4.17}$$

4.3 Single layer cells

4.3.1 Literature overview

Though efficiencies of single layer photovoltaic cells are rather low, studies carried out on simple metal/organic solid/metal (M/OS/M) structures are relevant since they provide information on basic optoelectronic properties of investigated organic solids as well as on the nature of processes taking place in such structures in the presence of electric field or illumination. Numerical approach to modeling of photoelectric properties of M/OS/M systems was taken by Signerski et al., who considered thermal and photogeneration of free charge carriers at both electrode/organic material interfaces as well as in the bulk of the sample [78]. Singlet excitons, neutral generation centers of exponential spatial distribution, discrete level of traps of finite concentration and unipolar charge transport were regarded. Numerical calculations yielded current-voltage curves of illuminated samples, short-circuit current vs. linear absorption coefficient and illumination intensity under different conditions. Symbatic or antybatic behavior of j_{sc} dependent on trapping conditions and values of absorption coefficient along with a power-law dependence of j_{sc} on light intensity

$$j_{sc} \sim {I_0}^n , \tag{4.18}$$

where n ranged from 0 to 1, that stands in a good agreement with experimental data, were obtained.

Numerical and analytical approach to model the performance of surface barrier solar cells of different architectures, in which band bending near the barrier-former/ semiconductor contact is observed, was presented by Fonash [38]. This model involved the presence of minority charge carriers, hence a bipolar current flow was considered. Moreover, no internal electric field within the bulk of the semiconductor beyond the barrier-region was assumed in this model and the results of numerical simulations shown that good photovoltaic performance, for which the energy conversion efficiency exceeds 12% is possible in this type of cells. Therefore, this model is rather inconsistent with the results of experiments conducted in the field of single layer organic photovoltaic cells.

Analytical dark current-voltage expression for a hole-only metal-insulator-metal (MIM) organic diode, in which the presence of a uniform electric field within the whole organic layer is assumed, was derived by Bruyn et al. [79]. Authors of this work considered a model of a diode with asymmetric contacts, i.e. one Schottky type contact and one Ohmic type contact, of different work functions. Dark current density under bias U lower than the built-in voltage derived in the absence of band bending was

$$j_{dark} = \frac{e\mu_p N_v(\varphi_b - U)[\exp\left(\frac{eU}{kT}\right) - 1]}{d[\exp\left(\frac{e\varphi_b}{kT}\right) - \exp\left(\frac{eU}{kT}\right)]} \ , \tag{4.19}$$

while if band bending at the Ohmic contact, resulting from accumulation of free charge carriers diffusing from this electrode into an insulator or undoped semiconductor, was considered the following expression was proposed

$$j_{dark} = \frac{e\mu_p N_v(\varphi_b - b - U)[\exp\left(\frac{eU}{kT}\right) - 1]}{d[\exp\left(\frac{e\varphi_b}{kT}\right) - \exp\left(\frac{e(U+b)}{kT}\right)]} \ , \tag{4.20}$$

where N_v stands for the effective density of states, φ_b is the built-in voltage, d denotes the thickness of the organic layer, whereas b describes the magnitude of band-bending dependent on d, N_v and dielectric constant of the organic material. Under bias greater than the built-in voltage space charge limited current $($SCLC$)$ following the Mott-Gurney equation in the trap free case, i.e.

$$j = \frac{9}{8}\varepsilon\mu\,\frac{(U - \varphi_b)^2}{L^3} \tag{4.21}$$

was expected.

An overview regarding currents and photocurrents limited by some interface phenomena, like thermal, tunneling and photoinjection along with free charge carrier trapping taking place at the electrode/organic material junctions, as well as, at the organic material heterojunctions, was presented by Godlewski [80,81]. The open-circuit voltage developed in the one-dimensional system, in which both electrodes are active and inject the same carrier type, the rate of dark injection is constant, while the rate of photoinjection is proportional to the light intensity was described by Pope [82], according to whom the photovoltage step U_1 developed at the front electrode, for which $x = 0$, in a steady state at zero current flow is

$$U_1 = \frac{kT}{e}\ln\left(1 + \frac{j_{ph}}{j_0}\right) = \frac{kT}{e}\ln\frac{n_0}{{n_0}^{th}} \ . \tag{4.22}$$

Analogical expression can be written for the photovoltage step U_2 developed at the back electrode, for which $x = d$ and since these two voltages oppose each other, the resultant open-circuit voltage U_{oc} generated across such cell is equal to

$$U_{oc} = U_1 - U_2 = \frac{kT}{e}\ln\left(\frac{1 + j^f_{ph}/j^f_0}{1 + j^b_{ph}/j^b_0}\right) \ , \tag{4.23}$$

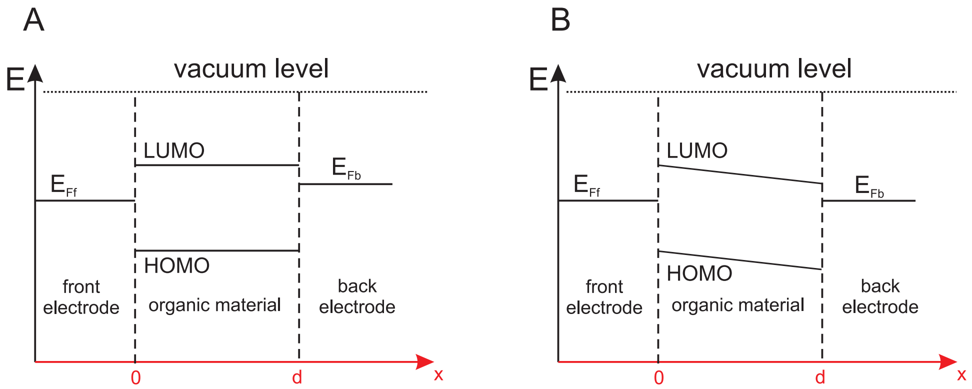

Figure 4.2: Schematic representation of relative positions of energy levels of a single organic layer and electrodes before contact (A) and after contact (B). A simple case of no surface dipoles and no band bending is considered, d stands for the thickness of an organic layer, indexes f and b refer to the front and back electrodes respectively.

where indexes f and b refer to front and back electrodes respectively. In a simple case of identical electrodes the open-circuit voltage results from different concentrations of free charge carriers at these contacts originating from their uneven illumination

$$U_{oc} = \frac{kT}{e} \ln \frac{n_0}{n_d} \ . \tag{4.24}$$

If we assume that photoinjected current is proportional to the light intensity I_0 and that a and b are the ratios of photoinjection efficiency to dark injection rate at front and rear electrodes respectively, then U_{oc} becomes

$$U_{oc} = \frac{kT}{e} \ln \left(\frac{1 + aI_0}{1 + bI_0} \right) \ . \tag{4.25}$$

In case of only one active contact, e.g. the front illuminated electrode/organic layer interface, when illumination is sufficiently high we may simplify the equation given above to the following one

$$U_{oc} = \frac{kT}{e} \ln \left(aI_0 \right) \ , \tag{4.26}$$

since in such case $J^f_{ph}/J^f_d \gg 1$, while $J^b_{ph}/J^b_d \ll 1$.

4.3.2 Constant field approximation model of a single layer cell

This section presents derivation of a simplified theoretical model of single layer photovoltaic cells that will be termed the constant field approximation (CFA) model.

Schematic energy diagram of the regarded one-dimensional system consisting of one organic layer of thickness d sandwiched between dissimilar electrodes is shown in Fig. 4.2. Band bending and surface dipoles are not taken into consideration. Electric field within the organic layer is uniform, hole transport can be neglected, front contact is a rectifying one, while the back contact is neutral, which means that neither light nor external bias affect the free charge carrier concentration at that contact. Moreover, upon illumination free charge carriers are generated as a result of exciton dissociation at the front illuminated electrode/organic material contact, whereas bulk generation is negligible. The total current flowing through such cells is a sum of drift and diffusion currents

$$j = j_{drift} + j_{diff} = -e\mu n \frac{\mathrm{d}\varphi}{\mathrm{d}x} + \mu kT \frac{\mathrm{d}n}{\mathrm{d}x} = \mathrm{const}\ . \tag{4.27}$$

In the absence of external bias internal field is determined by the difference in electrode work functions equal to ΔW. The built-in potential U_{bi} is then equal to

$$U_{bi} = \Delta W / e, \tag{4.28}$$

therefore, if we assume that the electric potential at the front electrode $\varphi(0)$ is zero then its value at the rear contact $\varphi(d)$ equals U_{bi}. Under external bias U the latter value remains unchanged while $\varphi(0) = U$. If free electron concentrations at front and rear contacts are

$$n(0) = n_0 \ \text{ and } \ n(d) = n_d \tag{4.29}$$

respectively, the solution of equation 4.27 yields

$$n(x) = \exp[e(\varphi(x) - U)/kT] \left\{ \frac{j}{\mu kT} \int\limits_0^x \exp[-e(\varphi(x) - U)/kT] \mathrm{d}x + n_0 \right\}\ . \tag{4.30}$$

Since the rear contact is neutral $n_d = n_d^{th}$, where n_d^{th} denotes the concentration of free electrons at the back contact in thermal equilibrium in the dark. Thus, according to equation given above, current j flowing through the considered system can be expressed as follows

$$j = \mu kT \, \frac{n_d^{th} \exp[-e(U_{bi} - U)/kT] - n_0}{\int\limits_0^d \exp[-e(\varphi(x) - U)/kT] \mathrm{d}x}\ . \tag{4.31}$$

Electric field within the considered device is constant, therefore electric potential varies linearly with x. Hence, regarding the boundary conditions one obtains the following expression for the spatial distribution of electric potential within the sample

$$\varphi(x) = U + \frac{U_{bi} - U}{d}\, x \; . \tag{4.32}$$

Substitution of this dependence into Eq. 4.31 yields the current-voltage relation for the regarded single layer cell

$$j = \frac{\mu e(U_{bi} - U)}{d} \, \frac{n_d^{th}\exp[-e(U_{bi} - U)/kT] - n_0}{1 - \exp[-e(U_{bi} - U)/kT]} \; . \tag{4.33}$$

Under thermal equilibrium conditions in the dark no current flows through the unbiased device and $n_0 = n_0^{th}$, hence

$$n_0^{th} = n_d^{th}\exp(-eU_{bi}/kT) \; . \tag{4.34}$$

If we assume that the processes of generation and recombination of free charge carriers at the illuminated contact are monomolecular processes we will obtain the following form of the continuity equation

$$\frac{-j}{ea} = G^{ex} + G^{th} - k_R n_0 \; , \tag{4.35}$$

where a denotes the width of a thin generation layer adjacent to the front contact, equal to one or two lattice constants [38], G^{ex} is the rate of photogeneration of free electrons, i.e. the concentration of free electrons generated via exciton dissociation in a unit time, G^{th} is the thermal generation rate, i.e. concentration of electrons generated thermally in a unit time, while k_R stands for the recombination constant. Thus, we may express the concentrations of free electrons at the front contact under illumination and in the dark as follows

$$n_0 = \frac{G^{ex} + G^{th} + j/(ea)}{k_R} \; , \tag{4.36}$$

while

$$n_0^{th} = \frac{G^{th}}{k_R} \; . \tag{4.37}$$

Substitution of these expressions into Eq. 4.33 leads to the following form of the current-voltage characteristics of the illuminated cell

$$j = -\frac{\mu e(U_{bi} - U)}{d} \, \frac{G^{ex}/k_R + n_d\exp[-eU_{bi}/(kT)]\,\{1 - \exp[eU/(kT)]\}}{1 - \exp[-e(U_{bi} - U)/kT] + \mu(U_{bi} - U)/(dak_R)} \tag{4.38}$$

that, according to Eqs. 4.34 and 4.37, may also be written in terms of generation rates and recombination constant

$$j = -\frac{\mu e(U_{bi} - U)}{d} \frac{G^{ex} + G^{th}\{1 - \exp[eU/(kT)]\}}{k_R - \frac{G^{th}}{n_d^{th}}\exp[eU/(kT)] + \mu(U_{bi} - U)/(da)} , \tag{4.39}$$

while the dark current-voltage relation may be expressed as follows

$$j_{dark} = -\frac{\mu e(U_{bi} - U)}{d} \frac{n_d^{th}\exp(-eU_{bi}/(kT))[1 - \exp(eU/(kT))]}{1 - \exp[-e(U_{bi} - U)/(kT)] + \mu(U_{bi} - U)/(dak_R)} . \tag{4.40}$$

According to this equation, under positive bias in the dark electrons flow toward the front contact, while under negative bias toward the back contact. Analogical but simplified expression for hole-only MIM (metal-insulator-metal) diodes was obtained by Bruyn et al., who assumed that concentrations of holes at both contacts do not depend on the applied voltage [79]. Comparison of Eqs. 4.40 and 4.39 lets us infer, that the density of the current flowing through the illuminated cell is a sum of the dark current density and the generation current density (j_g), both dependent on the applied voltage, where (j_g) is expressed as follows

$$j_g = -\frac{\mu e(U_{bi} - U)}{d} \frac{G^{ex}/k_R}{1 - \exp[-e(U_{bi} - U)/(kT)] + \mu(U_{bi} - U)/(dak_R)} . \tag{4.41}$$

Under reverse bias, i.e. at $U < 0$, j_{dark} and j may be approximated in the following manner as long as $G^{ex} \gg G^{th}$

$$j_{dark} \approx -\frac{\mu e(U_{bi} - U)}{d} \frac{aG^{th}}{ak_R + \mu(\varphi_{bi} - U)/(d)} \tag{4.42}$$

and

$$j \approx -\frac{\mu e(U_{bi} - U)}{d} \frac{aG^{ex}}{ak_R + \mu(\varphi_{bi} - U)/(d)} . \tag{4.43}$$

Under such conditions two characteristic cases may be distinguished:

- fast recombination and low mobility,
- slow recombination and high mobility.

In the first case, current densities are linear functions of the applied voltage:

$$j_{dark} \approx -\frac{\mu e G^{th}}{k_R d}(U_{bi} - U) = -\frac{\mu e n_d^{th}\exp[-eU_{bi}/(kT)]}{d}(U_{bi} - U) , \tag{4.44}$$

while

$$j \approx -\frac{\mu e G^{ex}}{dk_R}(U_{bi} - U) \ , \tag{4.45}$$

whereas in the second case, both current densities are constant and depend on charge carrier generation rates:

$$j_{dark} \approx -eaG^{th} = -eak_R n_d^{th} \exp[-eU_{bi}/(kT)] \ . \tag{4.46}$$

and

$$j \approx -eaG^{ex} \ . \tag{4.47}$$

The latter is the maximum generation current density. Under high forward bias dark current dominates the current flow and density of the current increases linearly with the applied voltage in the following manner

$$j = j_{dark} \approx -\frac{\mu e n_d^{th}}{d}(U_{bi} - U) \ . \tag{4.48}$$

At open-circuit no current flows through the cell, therefore according to Eq. 4.33

$$U_{oc} = \frac{kT}{e} \ln \frac{n_0}{n_0^{th}} \tag{4.49}$$

therefore

$$U_{oc} = \frac{kT}{e} \ln \left(\frac{G^{ex}}{G^{th}} + 1 \right) \ . \tag{4.50}$$

Thus, whenever the photogeneration rate is much greater than the thermal generation rate and the former is directly proportional to the incident light intensity I_0 the open-circuit voltage becomes a logarithmic function of I_0

$$U_{oc} = \frac{kT}{e} \ln(cI_0) \ , \tag{4.51}$$

where c is a constant. Moreover, in this case the open-circuit voltage exceeds the built-in voltage whenever the photogeneration rate is high enough, i.e. whenever

$$G^{ex} \geqslant k_R n_d^{th} \ . \tag{4.52}$$

At short-circuit $U = 0$, thus

$$j_{sc} = -\frac{\mu e U_{bi}}{d} \frac{n_0 - n_0^{th}}{1 - n_0^{th}/n_d^{th}} = -\frac{\mu e U_{bi}}{d} \frac{aG^{ex}}{ak_R - aG^{th}/n_d^{th} + \mu U_{bi}/d} \ . \tag{4.53}$$

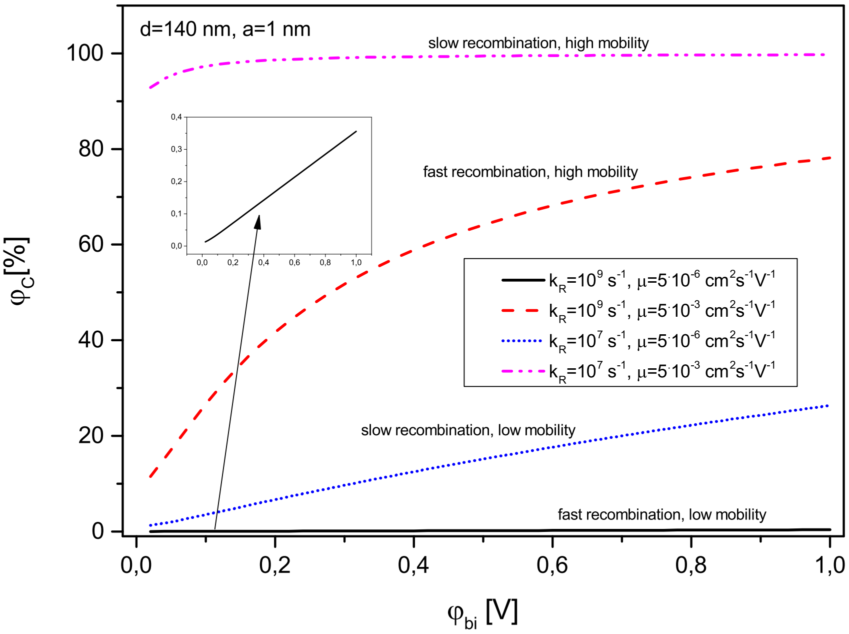

Figure 4.3: Free charge carrier collection efficiency as a function of the built-in field calculated for the derived CFA model (Eq. 4.55) for different values of recombination constant and free electron mobility specified in the inset of the graph.

According to this equation, short-circuit current density may be expressed as a product of the elementary charge, width of the generation layer, free electron photogeneration rate and electron collection efficiency φ_C:

$$j_{sc} = -e\varphi_C a G^{ex} \; , \tag{4.54}$$

where, according to Eqs. 4.34, 4.37 and 4.57 this efficiency may be expressed as follows

$$\varphi_C = \frac{\mu U_{bi}}{d}\,\frac{1}{ak_R\{1-\exp[-eU_{bi}/(kT)]\}+\mu U_{bi}/d} = \frac{v_d}{v_d + v_R\{1-\exp[-eU_{bi}/(kT)]\}} \; . \tag{4.55}$$

Terms $v_d = \mu e U_{bi}/d$ and $v_R = ak_R$ express the electron drift velocity and the surface recombination velocity respectively. If $\exp[-eU_{bi}/(kT)] \ll 1$, free charge carrier collection efficiency can be approximated by the following expression

$$\varphi_C = \frac{1}{1 + v_R/v_d} \; . \tag{4.56}$$

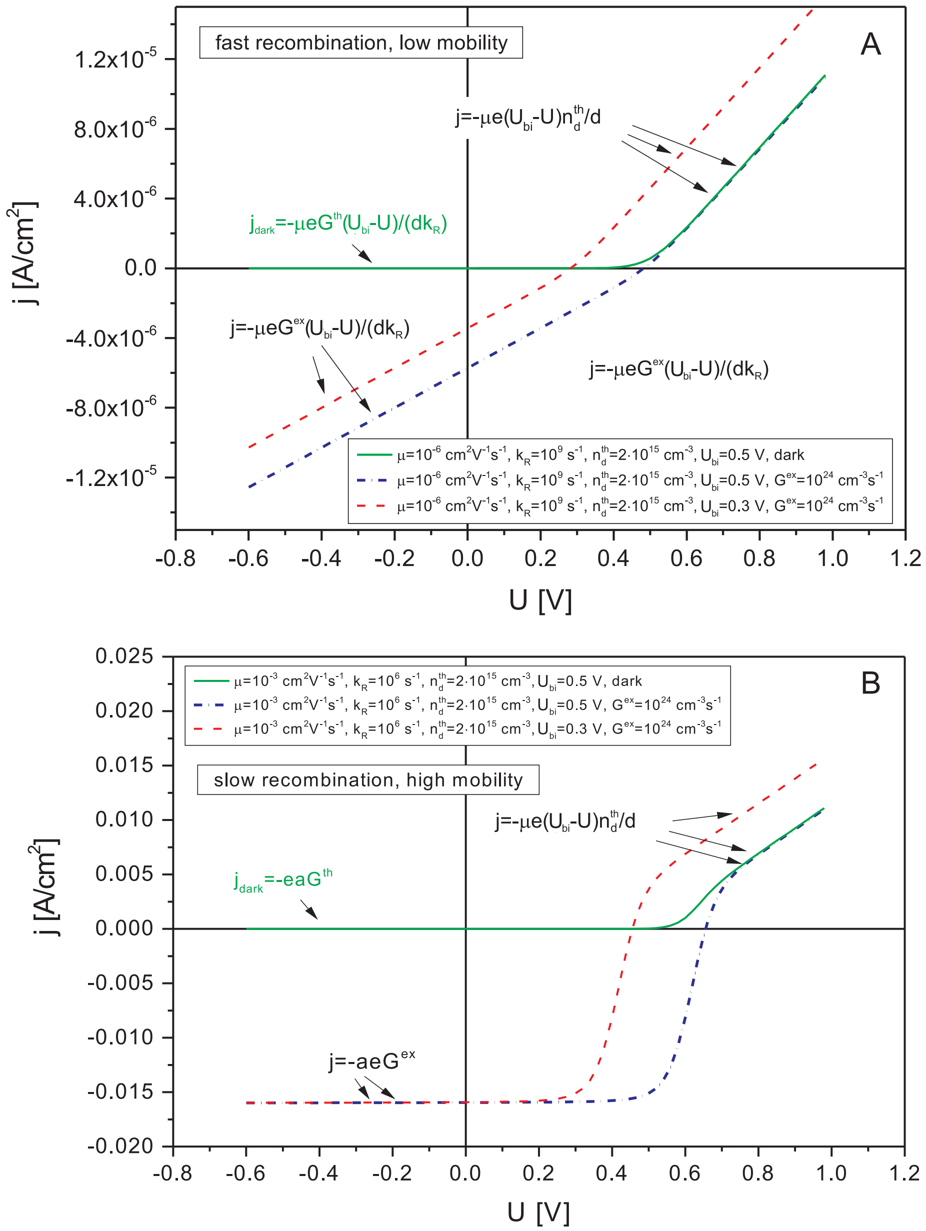

Figure 4.4: Influence of chosen parameters on the current-voltage characteristics of a single layer cell in case of fast recombination and low electron mobility (A) or slow recombination and high electron mobility (B) for the derived CFA model.

It is worth noting, that electron collection efficiency is a function of the built-in voltage (see Fig. 4.3) and is the lowest in the absence of the built-in field

$$\varphi_{Cmin} = \frac{1}{1 + ak_R \frac{d}{\mu} \cdot \frac{e}{kT}} = \frac{1}{1 + \frac{v_R}{v_d^T}} \ , \tag{4.57}$$

where v_d^T is the drift velocity of electrons under thermal voltage. When electron mobility is high drift velocity is much greater than $v_R - aG^{th}/n_d^{th}$ and electron collection efficiency reaches its maximum value equal to 1. If the photogeneration rate G^{ex} can be expressed in terms of exciton concentration at this interface $S(0)$, i.e. when

$$G^{ex} = \varphi_{diss} k_{diss} S(0) \ , \tag{4.58}$$

where φ_{diss} is the exciton-electron conversion efficiency and k_{diss} is the exciton dissociation rate constant, short-circuit current density may be written as follows

$$j_{sc} = -ea\varphi_C G^{ex} = -e\varphi_C \varphi_{diss} sS(0) = -e\varphi_C \varphi_{diss} \Phi_0^{ex} \ , \tag{4.59}$$

where $s = ak_{diss}$ denotes exciton annihilation velocity, while $\Phi_0^{ex} = sS(0)$ is the exciton flux density annihilation rate.
Since light intensity affects the value of $n_0 - n_0^{th}$, which is the number of free charge carriers generated at the front contact upon illumination, according to Eq. 4.53, light intensity dependence of the short-circuit current may be written as follows

$$j_{sc} \sim I_0^b \ , \tag{4.60}$$

where b is a constant dependent on recombination processes. If only monomolecular recombination is regarded b should be equal to 1.

The influence of a physical parameters, such as free electron mobility in the organic layer, recombination constant and built-in voltage on current-voltage characteristics in the regarded CFA model is shown in Fig. 4.4. On the basis of these characteristics and equations derived in this section, few conclusions can be drawn:

- built-in field has a strong effect on the open-circuit voltage
- under sufficient illumination the open-circuit voltage exceeds the built-in voltage

- monomolecular recombination decreases the open-circuit voltage
- high free charge carrier mobility and relatively low recombination constant are prerequisites for achieving high current densities and high fill factors
- built-in field strongly affects the free electron collection efficiency if mobility of these free charge carriers is low
- a kink in the current-voltage characteristics under forward bias above U_{oc} is present even if mobility of free electrons is relatively high
- such kink disappears when concentration of electrons at the rear contact and mobility of free electrons are high

4.4 Bilayer donor/acceptor systems

4.4.1 Literature overview

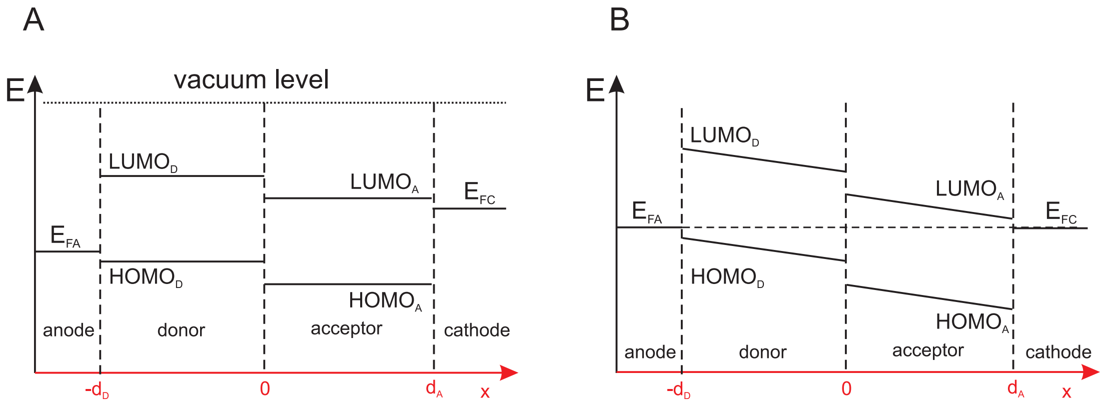

Figure 4.5: Schematic representation of relative positions of energy levels of electrodes and donor and acceptor materials before (A) and after (B) contact in bilayer donor/acceptor cells. A simple case of no surface dipoles and no band bending is considered, d_D and d_A denote the thickness of donor and acceptor layers respectively.

Lets consider one-dimensional current flow through a bilayer cell based on a planar donor/acceptor junction and proper electrodes of different work functions. Electrodes are suitable for the D/A junction if Fermi level of the anode matches the HOMO level of the donor material, while Fermi level of the cathode lies close to the LUMO level of the acceptor material and both contacts are ohmic. Bringing materials forming a cell into contact results in Fermi level alignment of the electrodes and development of electric field in both organic layers (Fig. 4.5). In the absence of light and external bias no current flows through the cell, since the current density j_0 resulting from thermal generation of free charge carriers in the bulk and at the donor/acceptor junction [83–85] and the current density $j_{in}(U=0)$ originating from thermal injection of charge carriers at the electrodes cancel each other out

$$j_0 + j_{in}(U=0) = 0 \tag{4.61}$$

According to Postcavage et al., Perez et al. and Koehler et al. [83–85], who studied small molecule/C_{60} or polymer/C_{60} cells, one can express j_0 as

$$j_0 = j_{mat} \mathrm{exp} \left(\frac{-\Delta E_{DA}}{\beta kT} \right) \ , \tag{4.62}$$

where ΔE_{DA} is the effective energy gap at the D/A interface, j_{mat} is independent of energy barrier height, but relies on donor and acceptor properties, such as reorganization energy (connected with electron transfer from D to A molecule) or recombination rate. Postcavage et al. postulated that β is the ideality factor, ranging from 1.5 to 2, resulting from misalignment of vacuum levels caused by energy level bending, interface dipoles and formation of CT states, while according to Perez et al. and Koehler et al.

$$\beta = 2m \ , \tag{4.63}$$

where m is the diode ideality factor. This factor is multiplied by 2 due to generation of a pair of free charge carriers in a single thermal activation process. As one can see, herein j_0 is independent of external bias, but depends on temperature and properties of materials forming the cell.

Recently, Richardosn et al. [25] applied asymptotic methods to model the dark current-voltage dependence for bilayer organic diodes and solar cells and they managed to extract the analytical solution of this problem basing on drift-diffusion equations. In order to find this solution some simplifications were made, including large jumps in electron affinity and ionization potential at the junction of organic materials, that ensured there are no electrons in the donor material and no holes in the acceptor material. Therefore, only Shockley-Read-Hall (SRH) recombination at the D/A junction was taken into account, though extension to other recombination mechanism was proposed. Moreover, a symmetric one-dimensional device in a steady state was considered, while Poole-Frenkel mechanism was neglected. To account for the effect of pinholes a constant shunt resistance was added. Under low reverse and forward bias U the obtained current density was expressed by the following equation

$$j_{small}(U) = \frac{U}{AR_{sh}} + j_0 \left[\exp\left(\frac{eU}{2kT} \right) - 1 \right] \ , \tag{4.64}$$

while at high bias

$$j_{large}(U) = \frac{U - U_0}{AR_s} \ , \tag{4.65}$$

where A is the active area of the cell, while U_0 is related to the built-in potential. In the intermediate voltage region another solution smoothly connecting the other two parts was found. It is worth noting, that this analytical solution is consistent with the Shockley equivalent circuit model of shunt resistance larger than series resistance and diode ideality factor of 2 originating from the SRH recombination assumption. In case of an ideal diode m=1, which means that free charge carriers recombine solely in a bimolecular manner at the donor/acceptor interface, whereas m=2 is obtained when charge carriers undergo trap-assisted (Shockley-Read-Hall) monomolecular recombination at this junction. In general, both types of recombination may operate so that $1 \leqslant m \leqslant 2$. If $m > 2$ then quality of the diode is very poor.

In practice, anode/organic material and organic material/cathode contacts are not Ohmic, so injection and extraction barriers for charge carriers are formed. Dipole layers and band bending are also very common. All these factors affect charge carrier generation, transport and extraction processes, so they have a serious impact on current-voltage characteristics of photovoltaic cells in the dark and under illumination and on their overall performance.

Short-circuit current density depends on the number of photogenerated free charge carriers. If these carriers are generated at the interface via exciton or CT state dissociation current density is depend on light intensity I_0. If both types of free charge carrier recombination operate at the same time concentrations of free charge carriers at the interface follow such general relation

$$p_i,\ n_i \sim I_0^{\alpha}\ , \tag{4.66}$$

where α is a constant ranging from 0.5 (for bimolecular recombination) to 1 (for monomolecular recombination). Short-circuit current is directly proportional to the population of free charge carriers, thus α, and so the dominating recombination type, can be determined from the light intensity dependence of the short-circuit current. Analytical model of this dependence for bilayer D/A cells with ohmic contacts and a uniform electric field within each layer was proposed by Signerski [73]. This model takes into account excitonic and thermal generation of free charge carriers, along with bimolecular and trap-assisted recombination of free charge carriers, under the assumption, that concentration of trapping cites is much higher than concentration of trapped charges. This model was successfully applied to describe the light intensity dependence of j_{sc} for CuPc/MePTCDI and PBrPc/MePTCDI cells illuminated with monochromatic light. One must bare in mind, that the incident light intensity is not the only feature of incident light affecting the photocurrent, since the latter depends on the exciton distribution in organic layers. This distribution is strongly affected by light absorption coefficient that varies with wavelength. Thus, the photocurrent value is not only a function of intensity but also a function of wavelength of the incident light.

The open-circuit voltage can be determined from Eq. 3.15 under the assumption that $R_{sh} \gg R_s$, which is valid for good photovoltaic diodes,

$$U_{oc} = \frac{mkT}{e} ln\left(\frac{j_{ph}}{j_0} + 1\right)\ . \tag{4.67}$$

Since the number of photogenerated charge carriers is much greater than the number of free charge carriers generated thermally $j_{ph} \gg j_0$, so

$$U_{oc} \approx \frac{mkT}{e} \ln\left(\frac{j_{ph}}{j_0}\right)\ . \tag{4.68}$$

According to Qi and Wang [86], for a given set of materials under 1 sun illumination and at room temperature, j_{ph} may vary in one order of magnitude, whereas j_0 can vary even in few orders of magnitude. For the aforementioned reasons,

j_0 is a crucial parameter determining the open-circuit voltage. If we combine the equation given above and Eq. 4.62, describing the dark saturation current, and assume that short-circuit current is practically the same as the generated photocurrent, we will obtain the following expression for the open-circuit voltage

$$U_{oc} = \frac{1}{e}\left[\frac{m}{\beta}\Delta E_{DA} - mkT\ln\frac{j_{mat}}{j_{sc}}\right] . \tag{4.69}$$

This expression was successfully used by Postcavage et al. to model experimental results obtained for small molecule/C_{60} cells, for which the second term of the expression given above was in the range of 0.4-0.7 eV [83].

Another simple expression for the open-circuit voltage can be obtained using Eq. 4.17, under the assumption that only one type of carriers is transported through each layer and electric field within both layers is uniform

$$U_{oc} = \frac{kT}{e}\ln\frac{n(0)p(0)}{n(d_n)p(-d_p)} , \tag{4.70}$$

where $n(0)$ and $n(d_n)$ are concentrations of electrons at the donor/acceptor and acceptor/cathode junctions, while $p(0)$ and $p(-d_p)$ stand for concentration of holes at the donor/acceptor and anode/donor interfaces respectively. If we assume that both metal/organic material contacts are ohmic, so light does not affect free charge carrier concentrations at these contacts, we will obtain the following light intensity dependence of the open-circuit voltage

$$U_{oc} = \frac{mkT}{e}\ln(cI_0) , \tag{4.71}$$

where c is a constant and $m = 2\alpha$. Thus, when free charge carriers recombine in the vicinity of the D/A junction in a monomolecular manner $m = 2$, while in case of bimolecular recombination $m = 1$. Such logarithmic light intensity dependence of the open-circuit voltage was observed for many organic systems.

More detailed analytical model, taking into account band bending in organic layers, presence of surface dipoles along with potential energy losses related to charge carrier extraction at the contacts originating from misalignment of Fermi levels of electrodes and energy levels in organic layers, was presented by Cheyns et al. [30]. Determination of band bending allowed to express the open-circuit voltage in terms of free charge carrier concentrations at the D/A interface

$$U_{oc} = \frac{1}{e}\left(|HOMO_D| - |LUMO_A| + kT\ln\frac{n_0 p_0}{N_A N_D}\right) , \tag{4.72}$$

where N_D and N_A are effective densities of states in donor and acceptor materials respectively. According to this equation, the open-circuit voltage in D/A devices does not depend on the electrode work functions and it reaches the maximum value determined by the $HOMO_D - LUMO_A$ offset when concentrations of free holes and free electrons at the D/A junction reach their maximum values, equal to the effective densities of states. If one takes the relation between free charge carrier concentrations and light intensity given by Eq. 4.66 a logarithmic dependence of the open-circuit voltage on light intensity, analogical to Eq. 4.71, will be obtained

$$U_{oc} = \frac{1}{e}\left[|HOMO_D| - |LUMO_A| + 2\alpha kT\ln(c_1 I_0)\right] \ , \tag{4.73}$$

were c_1 is a constant dependent on recombination process.

4.4.2 Constant field approximation model of a bilayer cell

Lets consider a model of a donor/acceptor junction based on the model derived for a single-layer cell. For the sake of simplicity the following assumptions are made:

1. one-dimensional bilayer planar donor/acceptor system is considered,
2. both electrode contacts, i.e. the anode/donor and acceptor/cathode contacts, are neutral (concentrations of free charge carriers at these contacts p_0 and n_d are constant, i.e. $p_0 = p_0^{th}$ and $n_d = n_d^{th}$),
3. there are no electrons in the donor layer and no holes in the acceptor layer,
4. generation and recombination of free charge carriers takes place solely in the thin generation layer placed at the D/A junction,
5. electric field within both organic layers is uniform.

Under these assumptions, current densities j_D and j_A in the donor and acceptor layers can be expressed in terms of p_j and n_j, that are free hole and free electron concentrations at the D/A junction, i.e. in the generation layer, respectively

$$
\begin{aligned}
j_D &= -\frac{\mu_p q U_D}{d_D} \frac{p_j - p_0 \exp(-\frac{q}{kT}U_D)}{1-\exp(-\frac{q}{kT}U_D)} \ , \\
j_A &= -\frac{\mu_n q U_A}{d_A} \frac{n_j - n_d \exp(-\frac{q}{kT}U_A)}{1-\exp(-\frac{q}{kT}U_A)} \ ,
\end{aligned}
\tag{4.74}
$$

where μ_p and μ_n are hole and electron mobilities in respective layers, while U_D and U_A denote the voltages across the donor and acceptor layers respectively. d_D and d_A stand for the thicknesses of these layers, whereas p_0 and n_d are free hole concentration at the anode/donor contact and free electron concentration at the acceptor/cathode interface. Voltages U_D and U_A are expressed as follows

$$U_D = U_p^{bi} - U_p \ , \tag{4.75}$$

$$U_A = U_n^{bi} - U_n \ , \tag{4.76}$$

where U_p^{bi} and U_n^{bi} are the built-in voltages in the donor and acceptor layers. Thus, their sum is the total built-in voltage U^{bi} equal to the difference of electrode work functions ΔW divided by the elementary charge

$$U_p^{bi} + U_n^{bi} = U^{bi} = \Delta W/e \ . \tag{4.77}$$

U_p and U_n are the voltages arising in the donor and acceptor layers as a result of external voltage and/or illumination, therefore

$$U_p + U_n = U \ , \tag{4.78}$$

where U stands for the total voltage measured across the device. Relations between these voltages may be found from the condition stating the continuity of the normal component of electric displacement field at the boundary of two media

$$\frac{\varepsilon_D U_D}{d_D} = \frac{\varepsilon_A U_A}{d_A} \ , \tag{4.79}$$

that leads to the following expressions

$$U_D = \frac{U^{bi} - U}{1 + \varepsilon_D d_A/(\varepsilon_A d_D)} \ , \tag{4.80}$$

$$U_A = \frac{U^{bi} - U}{1 + \varepsilon_A d_D/(\varepsilon_D d_A)} \ , \tag{4.81}$$

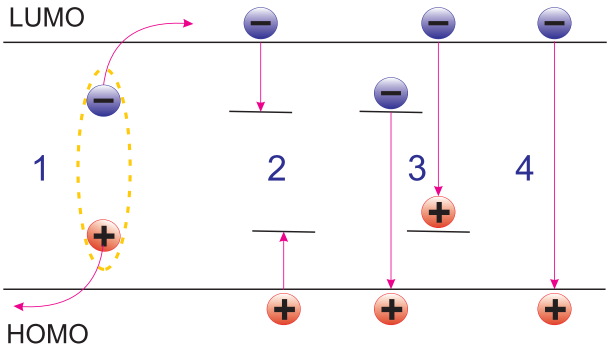

Figure 4.6: Free charge carrier generation and recombination processes taken into consideration in the CFA model of a bilayer cell: thermal or photogeneration of free charge carriers (1), monomolecular trap-assisted recombination (2), trapped electron/hole-free hole/electron recombination (3), free electron-free hole bimolecular recombination (4).

in which ε_D and ε_A stand for the dielcetric constants of donor and acceptor layers respectively. In a steady state the same current flows through both layers and its density j depends on generation and recombination processes taking place in the generation layer. In this model the following continuity equation, regarding thermal and light induced free charge carrier generation, monomolecular trap-assisted recombination, bimolecular recombination, as well as recombination of free charge carriers with trapped carriers of the opposite sign, is considered (see Fig. 4.6)

$$G^{ex} + G^{th} - k_R^n n_j - \alpha_n n_j p_{jt} - \alpha n_j p_j = -\frac{j}{ea} , \tag{4.82}$$

where G^{ex} and G^{th} are the rates of photo- and thermal generation, k_R^n, α_n and α stand for SRH recombination constant, bimolecular free electron-trapped hole recombination constant and bimolecular free electron-free hole recombination constant, while p_{jt} is the concentration of trapped holes. If Langevin recombination is considered free hole-free electron bimolecular recombination constant α is expressed as follows

$$\alpha = \frac{e(\mu_p + \mu_n)}{\varepsilon} , \tag{4.83}$$

where ε stands for the permittivity of the generation layer. In this equation, also known as the Debye-Smoluchowski equation, bimolecular recombination rate is independent of the external electric field, though there are some models that assume this process as the field and free charge carrier concentration dependent one [87].

In a steady state occupation of traps does not change, therefore the following expressions are valid

$$k_R^p p_j - \alpha_n n_j p_{jt} = 0 \quad \text{and} \tag{4.84}$$

$$k_R^n n_j - \alpha_p p_j n_{jt} = 0 \; . \tag{4.85}$$

Thus, $k_R^p p_j = \alpha_n n_j p_{jt}$ and

$$G^{ex} + G^{th} - k_R^n n_j - k_R^p p_j - \alpha n_j p_j = -\frac{j}{ea} \; . \tag{4.86}$$

According to this equation,

$$G^{th} = k_R^p p_j^{th} + k_R^n n_j^{th} + \alpha n_j^{th} p_j^{th} \; , \tag{4.87}$$

since no current flows through an unbiased device in the dark. p_j^{th} and n_j^{th} stand for the hole and electron concentrations in the generation layer under thermal equilibrium conditions. These concentrations, as well as concentrations p_j and n_j, can be extracted from the set of Eqs. 4.74. Substitution of these concentrations into the continuity equation 4.86 results in the following current-voltage characteristics of the modeled device

$$0 = -\alpha AB j^2 + \left(\frac{1}{ea} + AC + BD\right) j + G^{ex} + E \; , \tag{4.88}$$

where

$$A = \frac{d_A \left[1 - \exp\left(-\frac{eU_A}{kT}\right)\right]}{\mu_n e U_A} \ , \tag{4.89}$$

$$B = \frac{d_D \left[1 - \exp\left(-\frac{eU_D}{kT}\right)\right]}{\mu_p e U_D} \ , \tag{4.90}$$

$$C = k_R^n + \alpha p_0 \mathrm{exp}\left(-\frac{eU_D}{kT}\right) \ , \tag{4.91}$$

$$D = k_R^p + \alpha n_d \mathrm{exp}\left(-\frac{eU_A}{kT}\right) \ , \tag{4.92}$$

$$\begin{aligned} E = k_R^n n_j^{th} \left[1 - \exp\left(\frac{eU_n}{kT}\right)\right] + k_R^p p_j^{th} \left[1 - \exp\left(\frac{eU_p}{kT}\right)\right] + \\ \alpha n_j^{th} p_j^{th} \left[1 - \exp\left(\frac{eU}{kT}\right)\right] \ , \end{aligned} \tag{4.93}$$

$$n_j^{th} = n_d \mathrm{exp}\left(-\frac{eU_n^{bi}}{kT}\right) \ , \tag{4.94}$$

$$p_j^{th} = p_0 \mathrm{exp}\left(-\frac{eU_p^{bi}}{kT}\right) \ . \tag{4.95}$$

As far as one can see, even though the considered model is very simple, as it does not take into account many processes that may take place in the real device, such as exciton-exciton interactions, detrapping of charge carriers caused by light or generation and recombination of free charge carriers in the bulk of donor and acceptor layers, the obtained current-voltage characteristics is rather complex.

If bimolecular recombination can be neglected, i.e. when $\alpha \approx 0$, current-voltage relation becomes less complicated and takes the following form

$$j = -ea \, \frac{G^{ex} + k_R^n n_j^{th} \left[1 - \exp\left(\frac{eU_n}{kT}\right)\right] + k_R^p p_j^{th} \left[1 - \exp\left(\frac{eU_p}{kT}\right)\right]}{1 + eak_R^n A + eak_R^p B} \tag{4.96}$$

Therefore, two characteristic cases can be distinguished at high revers bias

1. slow recombination and high mobility of free charge carriers,

2. fast recombination and low mobility of free charge carriers.

In the first case, current densities are independent of voltage and reach their maximum values

$$j_{dark} = -eaG^{th} \text{ and} \tag{4.97}$$

$$j = -eaG^{ex} \ , \tag{4.98}$$

whereas in the second case, current-voltage response depends strongly on parameters of both layers, among which $\varepsilon_A d_D/\varepsilon_D d_A$ ratio plays one of the most important roles. If this ratio is much lower than 1, while mobilities of free charge carriers and their recombination constants are of the same magnitude, the donor layer dominates the current-voltage behavior, thus

$$j_{dark} = -\frac{e\mu_p p_j^{th}}{d_D\left(1+\frac{\varepsilon_D d_A}{\varepsilon_A d_D}\right)}\left(U^{bi}-U\right) \tag{4.99}$$

$$j = -\frac{e\mu_p G^{ex}}{k_R^p d_D\left(1+\frac{\varepsilon_D d_A}{\varepsilon_A d_D}\right)}\left(U^{bi}-U\right) \ , \tag{4.100}$$

while if $\varepsilon_A d_D/\varepsilon_D d_A$ is much greater than 1, the acceptor layer is the dominant one, and hence

$$j_{dark} = -\frac{e\mu_n n_j^{th}}{d_A\left(1+\frac{\varepsilon_A d_D}{\varepsilon_D d_A}\right)}\left(U^{bi}-U\right) \tag{4.101}$$

$$j = -\frac{e\mu_n G^{ex}}{k_R^n d_A\left(1+\frac{\varepsilon_A d_D}{\varepsilon_D d_A}\right)}\left(U^{bi}-U\right) \ . \tag{4.102}$$

In these cases, current flowing through a cell is a linear function of applied voltage. Under high forward bias current injected from the electrodes is greater than the photogeneration current ($j = j_{dark}$) and the roles of the dominant and minor layers are switched: if $\varepsilon_A d_D/\varepsilon_D d_A$ is much lower/greater than one then the acceptor/donor layer, respectively, governs the current flow. Again, current density is linearly dependent on applied voltage and

$$j = j_{dark} = -\frac{e\mu_n n_d}{d_A\left(1+\frac{\varepsilon_A d_D}{\varepsilon_D d_A}\right)}\left(U^{bi}-U\right) \text{ or} \tag{4.103}$$

$$j = j_{dark} = -\frac{e\mu_p p_0}{d_D\left(1+\frac{\varepsilon_D d_A}{\varepsilon_A d_D}\right)}\left(U^{bi}-U\right) \ , \tag{4.104}$$

respectively. In the absence of bimolecular recombination short-circuit current density is expressed by the following equation

$$j_{sc} = -\frac{eaG^{ex}}{1 + \frac{ak_R^n d_A\left[1-\exp\left(-\frac{eU_n^{bi}}{kT}\right)\right]}{\mu_n U_n^{bi}} + \frac{ak_R^p d_D\left[1-\exp\left(-\frac{eU_p^{bi}}{kT}\right)\right]}{\mu_p U_p^{bi}}}\ , \tag{4.105}$$

therefore the maximum value of j_{sc} obtained in case of low recombination constants and high mobilities of both types of free charge carriers is equal to the generation current density, i.e.

$$j_{sc} = -eaG^{ex}\ . \tag{4.106}$$

In case of relatively low free charge carrier mobilities and high recombination constants, $\varepsilon_A d_D/\varepsilon_D d_A$ ratio determines the dominant layer. If this ratio is lower/greater than one then

$$j_{sc} = -\frac{e\mu_p U_{bi} G^{ex}}{k_R^p d_D\left(1 + \frac{\varepsilon_D d_A}{\varepsilon_A d_D}\right)} \quad \text{or} \tag{4.107}$$

$$j_{sc} = -\frac{e\mu_n U_{bi} G^{ex}}{k_R^n d_A\left(1 + \frac{\varepsilon_A d_D}{\varepsilon_D d_A}\right)}\ , \tag{4.108}$$

respectively. At open-circuit no current flows through the device, therefore the open-circuit voltage can be determined from the following equation

$$G^{ex} + k_R^n n_j^{th}\left[1 - \exp\frac{eU^{oc}}{kT\left(1 + \frac{\varepsilon_A d_D}{\varepsilon_D d_A}\right)}\right] + k_R^p p_j^{th}\left[1 - \exp\frac{eU^{oc}}{kT\left(1 + \frac{\varepsilon_D d_A}{\varepsilon_A d_D}\right)}\right] = 0\ . \tag{4.109}$$

If $\varepsilon_A d_D/(\varepsilon_D d_A) = 1$, then the open-circuit voltage can be expressed in terms of photo- and thermal generation rates

$$U_{oc} = \frac{2kT}{e}\ln\left(\frac{G^{ex}}{G^{th}} + 1\right)\ . \tag{4.110}$$

If $\frac{G^{ex}}{G^{th}} \gg 1$, the open-circuit voltage may be expressed as follows

$$U_{oc} = U^{bi} + \frac{2kT}{e}\ln\frac{G^{ex}}{k_R^n n_d + k_R^p p_0} \tag{4.111}$$

and it becomes greater than the built-in voltage whenever

$$G^{ex} > k_R^n n_d + k_R^p p_0\ . \tag{4.112}$$

The influence of mono- and bimolecular recombination constants on the current-voltage characteristics and photovoltaic parameters for the modeled device is

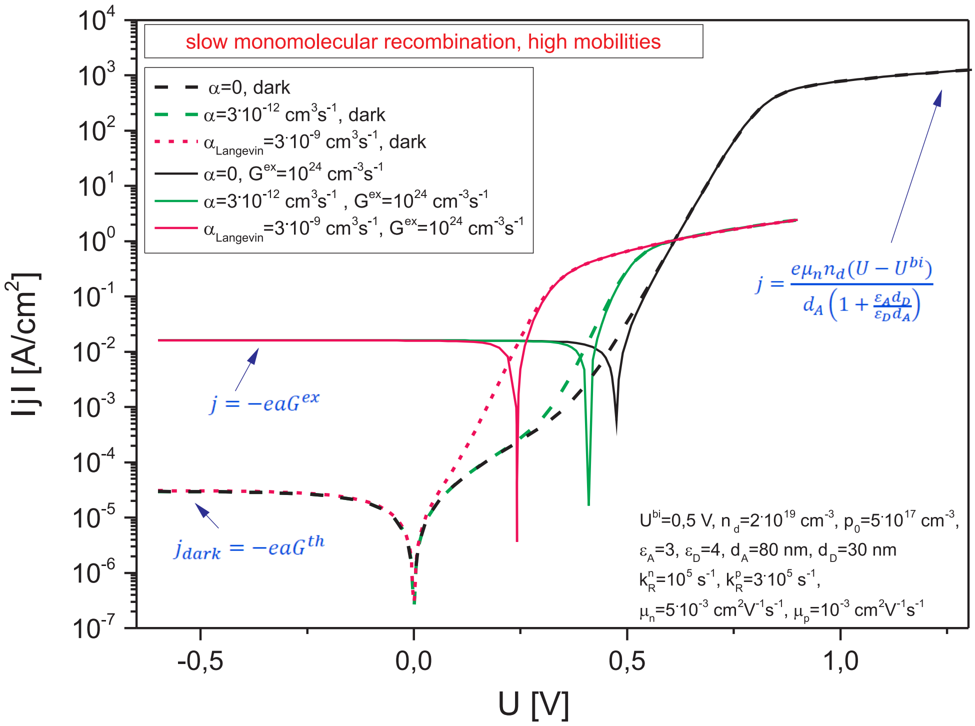

Figure 4.7: Current density as a function of applied voltage for the D/A cell according to the derived CFA model in case of low monomolecular recombination constant and high mobility in the presence and absence of bimolecular recombination in a semilog scale. Values of constants are given in the graph.

shown in Figs.4.7 and 4.8. On the basis of these graphs and derived equations the following conclusions regarding the CFA model of a bilayer D/A cell may be drawn:

- open-circuit voltage can exceed the built-in voltage,
- mobility of free charge carriers does not directly affect the open-circuit voltage,
- high values of free charge carrier mobility are prerequisites for achieving high current densities,
- bimolecular Langevin recombination has a minor impact on the short-circuit current density

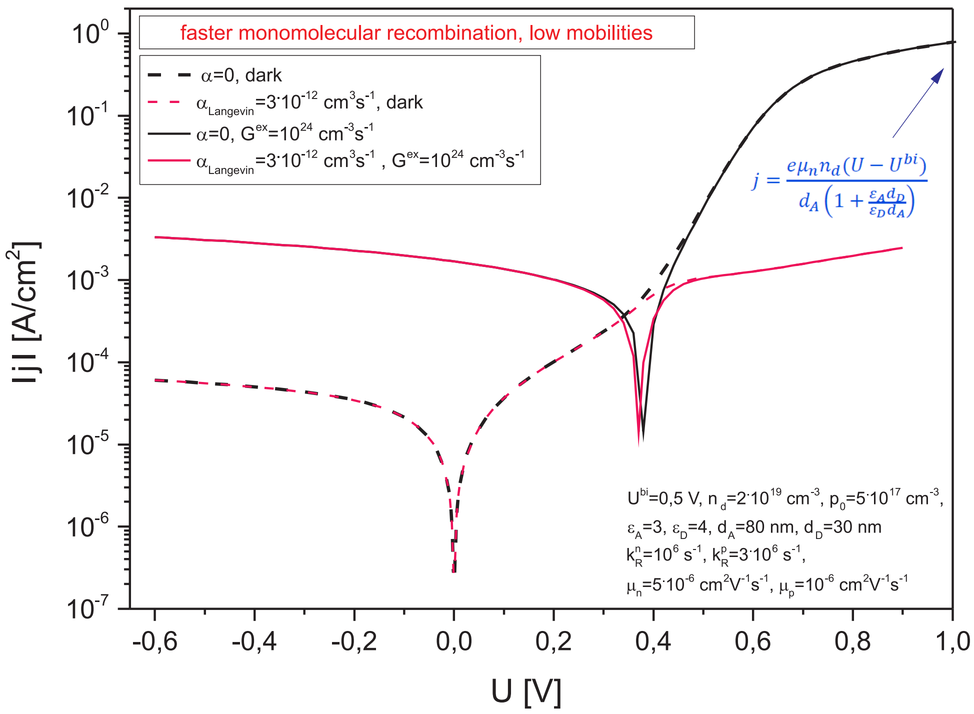

Figure 4.8: Current density as a function of applied voltage for the the D/A cell according to the derived CFA model in case of high monomolecular recombination constants and low free charge carrier mobilities in the presence and absence of bimolecular recombination in a semilog scale. Values of constants used in both cases are given in the graphs.

- the influence of monomolecular recombination on j_{sc} is strongly pronounced if free charge carrier mobilities are low

- recombination of free charge carriers strongly limits the open-circuit voltage: if free charge carrier mobility is low then bimolecular Langevin recombination constant is low and U_{oc} is reduced mainly due to monomolecular recombination, while in case of high free charge carrier mobilities bimolecular recombination becomes dominant

- recombination increases the reverse current density in the dark

- presence of bimolecular recombination practically does not influence the current-voltage curve under illumination under reverse bias and relatively low forward bias but significantly hampers the forward current around and above U_{oc}.

- relation between dielectric constants and thicknesses of donor and acceptor layers, namely the $\varepsilon_A d_D/\varepsilon_D d_A$ ratio, plays an important role, as it determines the dominant layer that governs the current flow and affects the j_{sc} and U_{oc} values

Chapter 5

Materials choice, device fabrication and characterization

5.1 Materials choice

MEH-PPV (poly[2-methoxy-5-(2-ethylhexyloxy-p-phenylenevinylene)]) and DIP (diindeno[1,2,3-cd:1’,2’,3’-lm]perylene) were chosen as donor materials to enable utilization of solar radiation in the whole visible range and to provide a suitable $\mathrm{HOMO_D}$-$\mathrm{LUMO_A}$ offset. The former is a polymer material, while the latter is a small molecule, therefore it was possible to determine the course of photovoltaic phenomenon and applicability of F_{16}ZnPc in polymer/small molecule and small molecule/small molecule types of cells. Chemical structure of organic materials

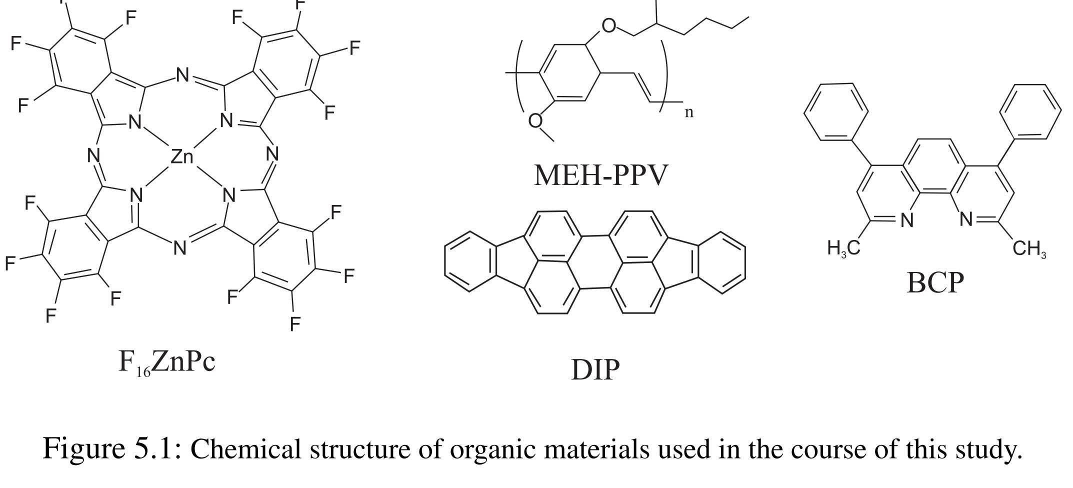

Figure 5.1: Chemical structure of organic materials used in the course of this study.

under study is shown in Fig. 5.1, while normalized absorption spectra of donor and acceptor materials, as well as, relative positions of HOMO and LUMO levels of films of these materials are shown in Fig. 5.2. These positions were not verified experimentally in the course of this study, but taken from literature, according to which, HOMO positions of MEH-PPV, DIP and F_{16}ZnPc are 5.1-5.3 eV [51, 88], 5.35 eV [89] and 6.5 eV [90], respectively, whereas LUMO positions for these materials are 2.9-3.0 eV [51, 88], 2.85 eV [89] and 4.6 eV [90] respectively. One must bare in mind, that, as it was already explained, the terms HOMO and LUMO originally refer to positions of molecular orbitals of single molecules. However, very often these terms are used to describe positions of charge (hole and electron) transporting bands in layers formed by these materials. Herein, terms HOMO and LUMO have the latter meaning.

MEH-PPV is a soluble derivative of poly(p-phenylene vinylene). It is one of the most common donor polymers used in organic bilayer and bulk heterojunction solar cells [28, 51, 91–93]. DIP, which is a derivative of a perylene die, is rather insoluble, but forms thin films of pronounced crystallinity, with molecules standing almost upright with their long axis perpendicular to the surface of a substrate, when deposited from the vapor phase under suitable conditions [94, 95]. Such structural order of DIP layers accounts for high values of free charge carrier mobility and exceptionally high values of exciton diffusion length, exceeding 100 nm, reported for this material [42].

In the course of this study the ITO and CuI anodes were used. Fermi level of ITO equals 4.7-5.0 eV [51, 96], while 5.3 eV and 2.3 eV are the positions of the valence and conduction bands of CuI respectively. Ag, for which the Fermi level position is 4.3 eV [97] was used as a cathode. To improve metal/organic material contacts, thin layers of molybdenum oxide and bathocuproine were introduced. The positions of the valence and conduction bands of MoO_3 buffer layer are 5.1-5.4 eV and 1.9-2.3 eV respectively [98, 99], while HOMO and LUMO positions of BCP are 7 eV and 3.5 eV [96]. Thin films of MoO_3 deposited on the top of ITO electrode are believed to modify ionization potential of the anode, causing a rise in the built in potential, and as a result, an increase in the open-circuit voltage [100]. It was also stated, that an interlayer made of transition metal oxides,

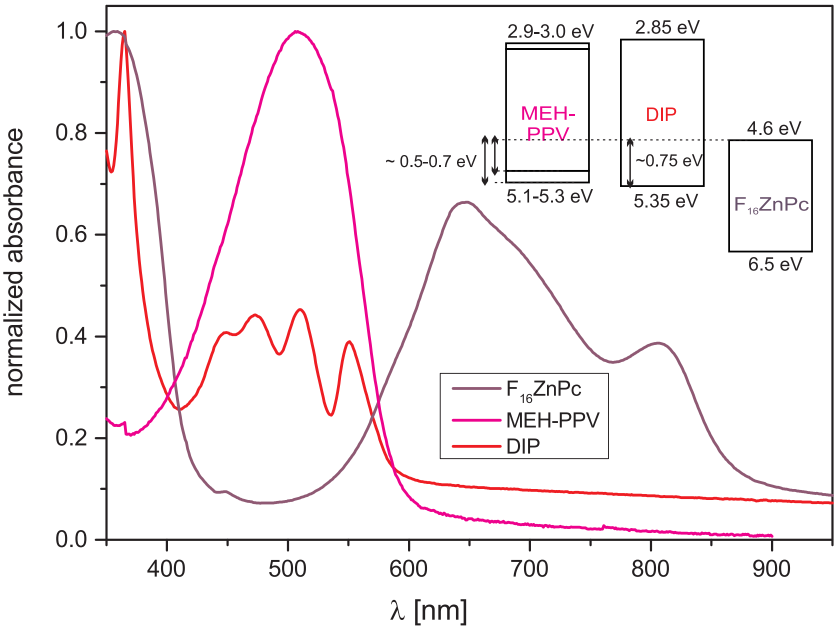

Figure 5.2: Normalized absorption spectra along with HOMO and LUMO positions of MEH-PPV, DIP and F_{16}ZnPc films.

such as MoO_3, prevents from chemical reactions between the ITO and the active layer [63]. Moreover, there are some reports, that conduction and valence bands of MoO_3 may lie much deeper (around 6.7 eV and 9.7 eV respectively) and thus the role of this interlayer is not to provide hole selectivity of the electrode due to large energy bandgap of this semiconductor and its valence band alignment with Fermi level of the anode but, similarly to strong electron-acceptor molecular dopants, to make p-type regions close to the interlayer/organic junction, as a result of electron transfer from organic material to this oxide [61, 101]. BCP was chosen since it is widely used in organic solar cells due to its exciton blocking ability [102,103] and because of the fact, that thin layers of this material are thought to protect the active layer from the damage induced during electrode evaporation, as well as, from further diffusion of metal atoms into organic materials [104]. These two processes introduce a large number of defects into organic layers. Presence of these buffer layers should eliminate some electrode effects (like formation of Schottky junctions at organic material/electrode interfaces) revealing processes taking place at the MEH-PPV/F_{16}ZnPc and DIP/F_{16}ZnPc junctions.

5.2 Device fabrication

Detailed description of techniques used for sample fabrication and characterization of individual layers can be found in the appendix.

5.2.1 Single layer cells

ITO/F_{16}ZnPc/Ag, ITO/F_{16}ZnPc/BCP/Ag and CuI/F_{16}ZnPc/BCP/Ag devices were fabricated to enable investigation of photoelectric properties of the regarded phthalocyanine and determination of its applicability in single layer cells. Samples were prepared on glass substrates partially covered by ITO of sheet resistance of 40 Ω/square, purchased from PGO, or on borosilicate glass, on the top of which a thin layer of CuI was deposited. Glass substrates were cleaned in an ultrasonic bath in acetone and isopropanol, and dried subsequently in the hot air flow. F_{16}ZnPc and BCP were purchased from Aldrich. F_{16}ZnPc was purified by means of train sublimation, whereas other materials under study were used as received. Thin layers of Cu (about 30 nm-thick) were evaporated under high vacuum on the top of borosilicate glass and then iodized. As a result, CuI layers about 50 nm-thick were obtained. F_{16}ZnPc layers of different thickness were deposited either on ITO substrates or on CuI layer by means of physical vapor deposition (Auto 306 Turbo, Edwards, p=$3 \cdot 10^{-4}$ Pa). The same way 15 nm-thick BCP layers and 40 nm-thick Ag layers were deposited. Metallic electrode was evaporated through a shadow mask, and as a result four identical devices per one cycle were fabricated. The active area of the cells ranged from 0.05 to 0.1 cm^2. Fig. 5.3 shows the schematic structure of fabricated cells. All measurements were performed in ambient air, at room temperature, without encapsulation.

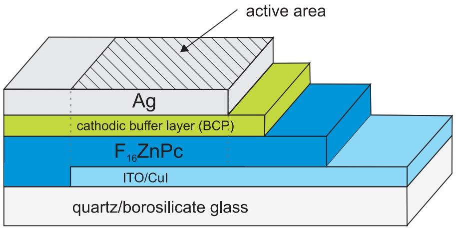

Figure 5.3: Structure of single layer cells. BCP is an optional buffer layer.

5.2.2 Bilayer cells

Planar bilayer ITO/MEH-PPV/F_{16}ZnPc/Ag, ITO/MoO_3/MEH-PPV/F_{16}ZnPc/Ag, ITO/MEH-PPV/F_{16}ZnPc/BCP/Ag, ITO/MoO_3/MEH-PPV/F_{16}ZnPc/BCP/Ag, ITO/MoO_3/DIP/F_{16}ZnPc/BCP/Ag and CuI/DIP/F_{16}ZnPc/BCP/Ag devices were fabricated in order to determine the course of photovoltaic phenomenon in donor/acceptor cells comprising the investigated F_{16}ZnPc material. Fig. 5.4 shows the schematic structure of bilayer cells with buffer layers. Simple planar structure of devices was chosen to enable determination of active junctions and processes leading to photogeneration of free charge carriers and their recombination. The same substrates as in case of single layer devices were used. MoO_3, MEH-PPV and DIP were purchased from Aldrich and used without further purification. Deposition of F_{16}ZnPc, BCP, CuI and Ag layers was desribed in the previous subsection. 5 nm-thick MoO_3 interlayers were evaporated under high vacuum. MEH-PPV was spin coated either on the top of ITO or anodic buffer layer from toluene solution of various concentrations, not exceeding 0.5 wt.%. These layers were subsequently annealed for 30 min at 100 °Cin a nitrogen flow. Thickness of the MEH-PPV layer varied with spin speed and solution concentration. More details on the fabrication of this layer are given in the appendix. DIP was deposited by means of PVD under the same conditions as other thermally evaporated materials under this study, and its thickness was 50÷60 nm. All measurements were performed in ambient air, at room temperature, without encapsulation.

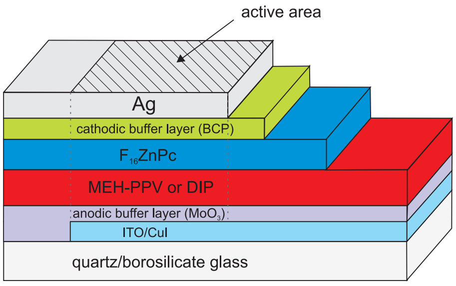

Figure 5.4: Structure of bilayer cells with a complete set of buffer layers.

5.3 Device characterization

Optoelectronic properties of materials forming the junctions, performance of fabricated cells and processes taking place in investigated systems were determined on the basis of short-circuit current density and open-circuit voltage action spectra, i.e. $j_{sc}(\lambda)$ and $U_{oc}(\lambda)$ curves, light intensity dependence of short-circuit current density and open-circuit voltage dependence, namely $j_{sc}(I_0)$ and $U_{oc}(I_0)$ curves, along with current-voltage characteristics, i.e. j-V curves, measured in the dark and under monochromatic illumination. Action spectra were recorded when solar cells were illuminated at a constant photon flux I_0 with monochromatic light of different wavelengths. Therefore, these spectra show the dependence between j_{sc} or U_{oc} and wavelength of the incident light, while during $j_{sc}(I_0)$ and $U_{oc}(I_0)$ measurements investigated cells were illuminated with monochromatic light of a chosen wavelength and light intensity was a variable. The same experimental setup shown in Fig. 5.5 was used to determine j_{sc} and U_{oc} dependences on wavelength and illumination intensity. Current-voltage curves were collected in the dark and under monochromatic or white light illumination using Keithley 6517 electrometer with computer controlled voltage source.

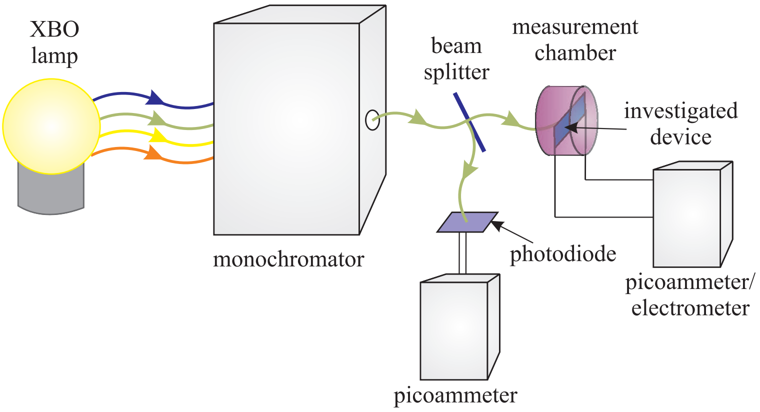

Figure 5.5: Experimental setup used for collection of $j_{sc}(\lambda)$ and $U_{oc}(\lambda)$ action spectra as well as $j_{sc}(I_0)$ and $U_{oc}(I_0)$ curves. MC110 monochromator, Keithly picoammeters and Keithly 6517 electrometer were used in the curse of this study.

Chapter 6

Photovoltaic phenomenon in single layer cells with the F_{16}ZnPc layer

6.1 Single layer cells with the ITO anode

In order to evaluate some properties of F_{16}ZnPc layer and determine the quality of its contact with Ag cathode, ITO/F_{16}ZnPc/Ag and ITO/F_{16}ZnPc/BCP/Ag cells with a 140 nm - thick phthalocyanine layer were fabricated. Energetic structure of materials forming investigated structures is shown in Fig. 6.1. Spectral response of short-circuit current, light intensity dependence of short-circuit current and open-circuit voltage as well as current-voltage characteristics for these cells were measured. Photocurrents flowing through the cells that did not have the bathocuproine buffer layer, as well as the open-circuit voltage measured for these cells, were much lower than those measured for the ITO/F_{16}ZnPc/BCP/Ag cells. This lets us infer that the quality of the F_{16}ZnPc/Ag contact is rather poor. For the aforementioned reasons only results obtained for the cells with the BCP interlayer are presented in this section.

6.1.1 Short-circuit current action spectra

From among all advantages showed by organic materials, high values of linear absorption coefficient in the visible range is the key feature of these materials making them attractive for photovoltaic applications. However, as it was men-

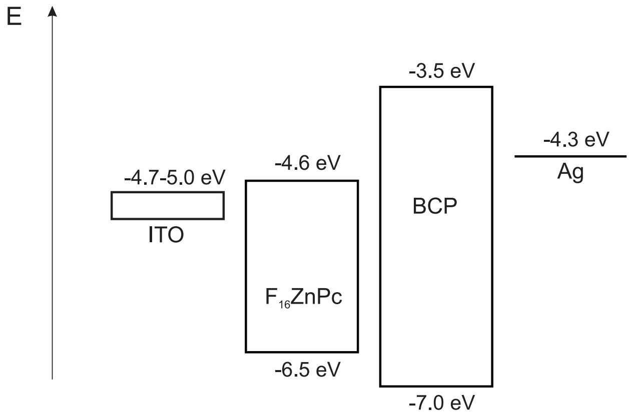

Figure 6.1: Energy level diagram of materials forming the ITO/F$_{16}$ZnPc/BCP/Ag cells.

tioned in section 3.4, exciton dissociation leading to creation of free charge carries takes place not in the bulk of the absorbing organic layer, but rather at the interface with another material. Therefore, apart from the linear absorption coefficient value κ, the exciton diffusion length L strongly affects the process of charge carrier generation, thus it should be considered as a prerequisite determining applicability of a certain organic material in the field of OPV. Unfortunately, values of exciton diffusion length showed by organic materials are relatively low. According to literature, singlet exciton diffusion length in MEH-PPV films is in the range of 5-14 nm [106], while, as it was already mentioned, exciton diffusion length in DIP layers was found to be exceptionally high. Due to lack of literature data, exciton diffusion length in the F$_{16}$ZnPc films was investigated in the course of this work. There are few different experimental methods enabling to determine the exciton diffusion length [107]. In case of F$_{16}$ZnPc a relatively simple method was chosen. This method enables to evaluate the exciton diffusion length in the single organic layer provided with electrodes, as long as excitons are generated only via light absorption, they are quenched at the electrode/organic material interface and providing that one-dimensional diffusion equation can be applied to describe concentration of excitons $S(x)$ along this layer. Such case was described in section 4.1. According to the CFA model of a single layer cell, short-circuit current density flowing through the sample under these conditions is

$$j_{sc} = e\varphi_C\varphi_{diss}sS_0, \tag{6.1}$$

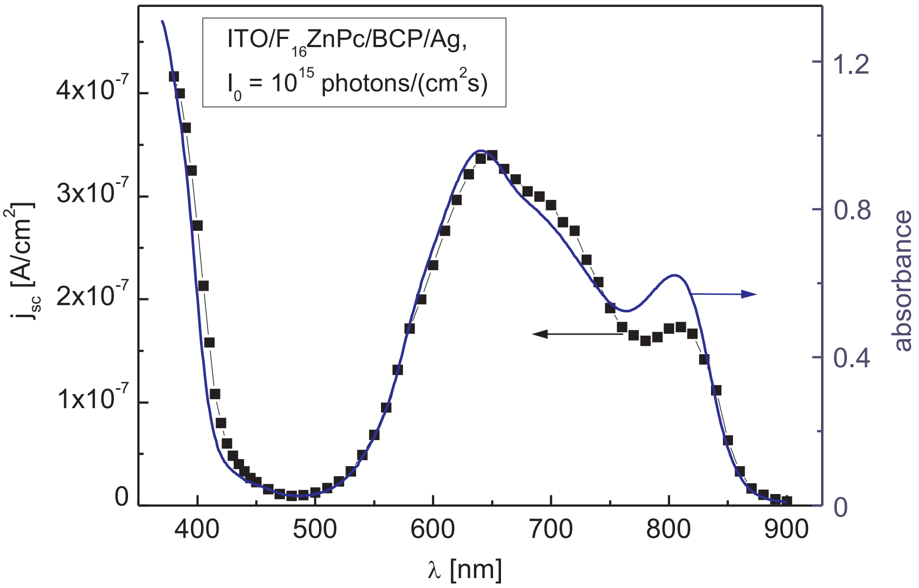

Figure 6.2: Short-circuit current density action spectrum obtained for ITO/F$_{16}$ZnPc/BCP/Ag cell with a 140nm-thick phthalocyanine layer. [105]

and since exciton concentration at the front contact $S(0)$ is expressed by Eq. 4.4 one obtains

$$j_{sc} = \frac{e\varphi_C\varphi_{diss}I_0}{(1+1/\kappa L)(1+D/sL)} \; . \tag{6.2}$$

Therefore, if one expresses ${j_{sc}}^{-1}$ as a function of κ^{-1}, a simple linear relation is obtained

$${j_{sc}}^{-1} = c + (c/L)\kappa^{-1} \; , \tag{6.3}$$

where

$$c = \frac{1+D/sL}{\varphi_C\varphi_{diss}eI_0} \; . \tag{6.4}$$

In such case, according to Eq. 6.3, exciton diffusion length L can be calculated knowing the slope of ${j_{sc}}^{-1}(\kappa^{-1})$ curve and its y-intercept. Short-circuit current density action spectrum of ITO/F$_{16}$ZnPc/BCP/Ag cells illuminated from the ITO side with a constant photon flux density of $I_0 = 10^{15}$ photons/(cm^{2}s) is shown in Fig. 6.2. Photocurrents flowing through these cells are symbatic within the whole investigated spectral range, so in this case measured photocurrent is limited by

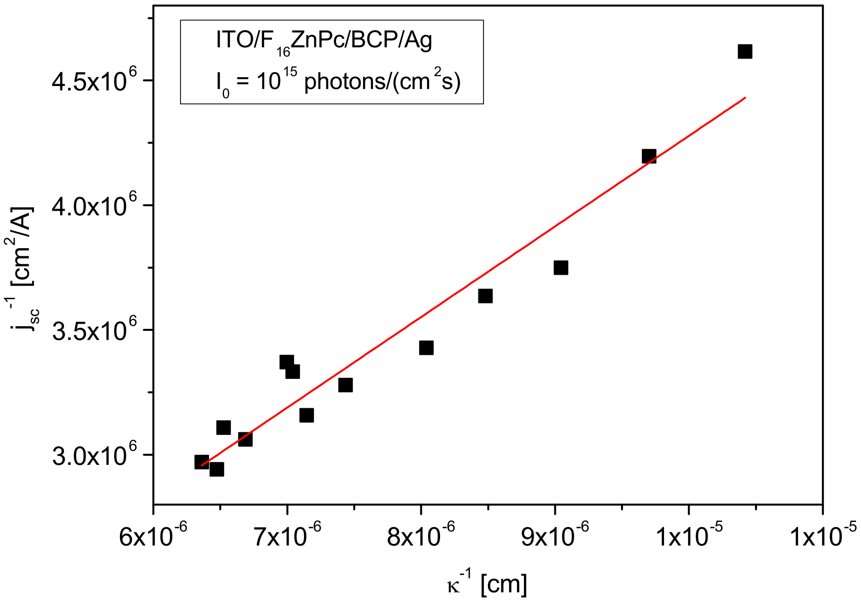

Figure 6.3: Inverse of the short-circuit current density obtained for ITO/F$_{16}$ZnPc/BCP/Ag cell with a 140nm-thick phthalocyanine layer vs. the reciprocal of linear absorption coefficient of F$_{16}$ZnPc within 620 nm - 740nm range. [105]

excitonic processes occurring near the illuminated ITO electrode, which makes the ITO/F$_{16}$ZnPc junction an active interface. Moreover, in the 620 nm-740 nm range absorption coefficient of F$_{16}$ZnPc is high enough to fulfill the $d \gg \kappa^{-1}$ condition. Furthermore, within this range ${j_{sc}}^{-1}$ is a linear function of κ^{-1} (Fig. 6.3). Thus, the method described above can be applied to calculate exciton diffusion length in the F$_{16}$ZnPc layer. Exciton diffusion length estimated using this method is (18 ± 7) nm. This value is reliable, since it is comparable to the exciton diffusion lengths found for other phthalocyanines, like CuPc and SnPc for which L=5-25 nm and L=(18.5 ± 4.8) nm respectively [76, 108–110].

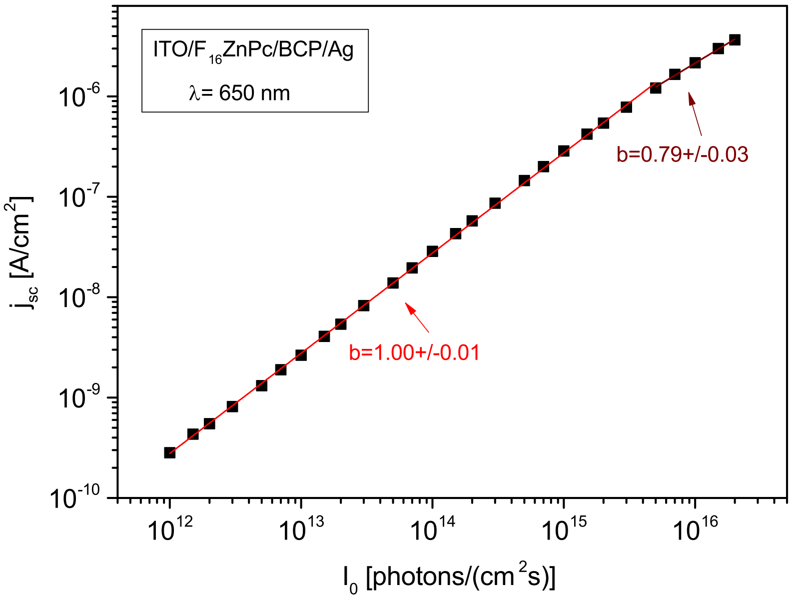

Figure 6.4: Short-circuit current density as a function of light intensity for monochromatic illumination (λ=650 nm) of the ITO/F_{16}ZnPc/BCP/Ag cell. Illumination from the ITO side.

6.1.2 Illumination intensity dependence of short-circuit current and open-circuit voltage

The effect of light intensity on short-circuit current and open-circuit voltage for monochromatic light of wavelength λ=650nm, referring to one of the absorption peaks of perfluorozincphthalocyanine, is presented in Fig. 6.4 and Fig. 6.5. Collected data, showing the relation between j_{sc} and I_0, are consistent with Eq. 4.60, therefore the dominant type of recombination can be inferred from this relation knowing the values of parameter b

- $b \approx 1$ up to $I_0 = 5 \cdot 10^{15}$ photons/(cm^{2}s),
- $b \approx 0.79$ at $I_0 > 5 \cdot 10^{15}$ photons/(cm^{2}s).

Hence, we may conclude that at low light intensities only monomolecular recombination of free charge carriers is observed, while at higher light intensities the influence of bimolecular recombination is also pronounced.

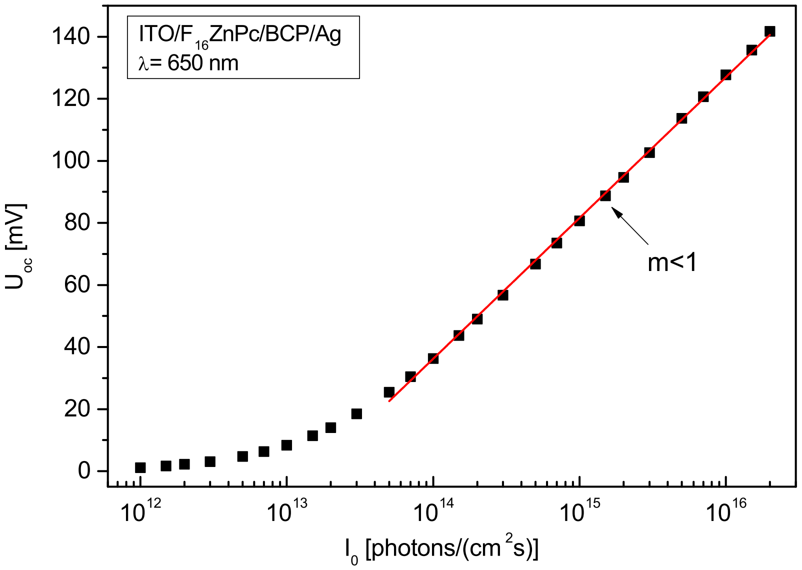

Figure 6.5: Open-circuit volatge as a function of light intensity for monochromatic illumination (λ=650 nm) of the ITO/F$_{16}$ZnPc/BCP/Ag cell. Illumination from the ITO side.

The data presented in the second graph, showing U_{oc} as a function of light intensity, fit well to the Eq. 4.51 at illumination intensities greater than $I_0 > 5 \cdot 10^{13}$ photons/(cm^{2}s) only if a prefactor m is introduced

$$U_{oc} = \frac{mkT}{e} \ln(cI_0) \ , \tag{6.5}$$

thus, they seem not to fit to the CFA model. Moreover, despite similarity of this equation and the one characteristic for an ideal diode, this prefactor can not be treated as a diode ideality factor, since its value is lower than 1 and therefore, these results can not be interpreted in terms of ideal diode device physics. Such dependence between the open-circuit voltage and illumination intensity might follow from exciton-charge carrier interactions.

6.1.3 Current-voltage characteristics

The role of the BCP layer and its influence on currents flowing through F$_{16}$ZnPc/Ag junction will be discussed in the next chapter, where it will be shown, that in the

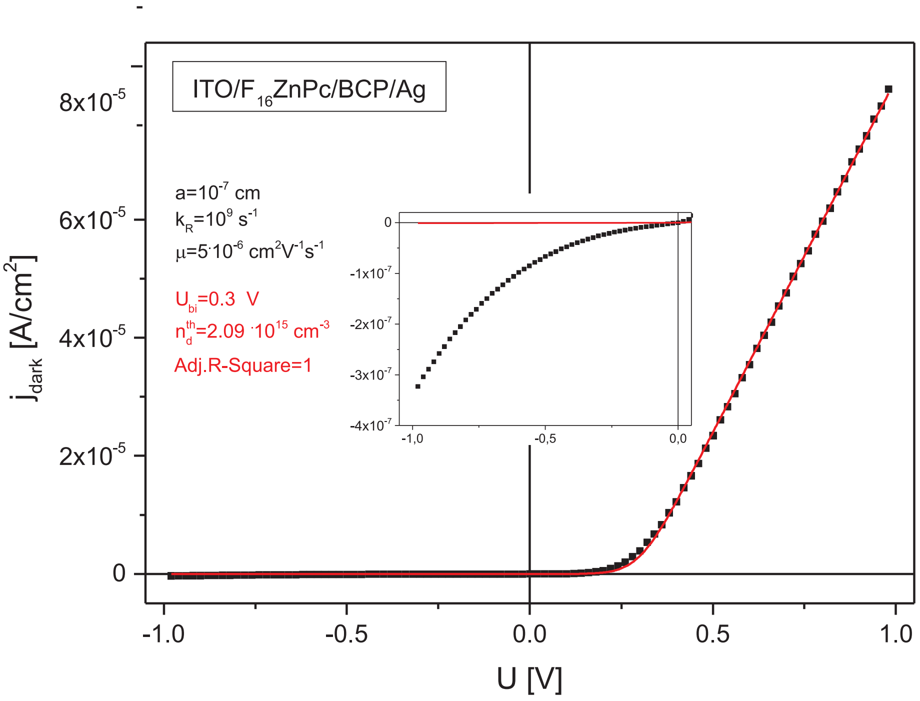

Figure 6.6: Current-volatge characteristics of the ITO/F_{16}ZnPc/BCP/Ag cell measured in the dark. U is the potential applied to the ITO electrode. Red lines and values of U_{bi} and n_d^{th} marked in red result from fitting the experimental data to Eq. 4.40 assuming that $k_R = 10^9$ 1/s, $a = 10^{-7}$ cm and $\mu = 5 \cdot 10^{-6}\ \mathrm{cm}^2/(\mathrm{Vs})$.

presence of this interlayer F_{16}ZnPc/Ag contact becomes Ohmic for the injection of electrons. On the basis of the action spectra measured for investigated cells and the direction of the current flow we may conclude that the ITO/F_{16}ZnPc contact is the active rectifying contact for electrons, and that under illumination at short-circuit holes are injected from the phthalocyanine layer to the ITO electrode, whereas electrons are transported through this layer toward Ag electrode. Forward/reverse polarization of the cell is the one for which positive/negative potential is applied to the ITO electrode respectively. Therefore, currents flowing through ITO/F_{16}ZnPc/BCP/Ag cells under forward bias (positive polarization of ITO with respect to Ag) should be much higher than the ones flowing through these samples under reverse bias.

Current-voltage characteristics were collected in the dark and under monochro-

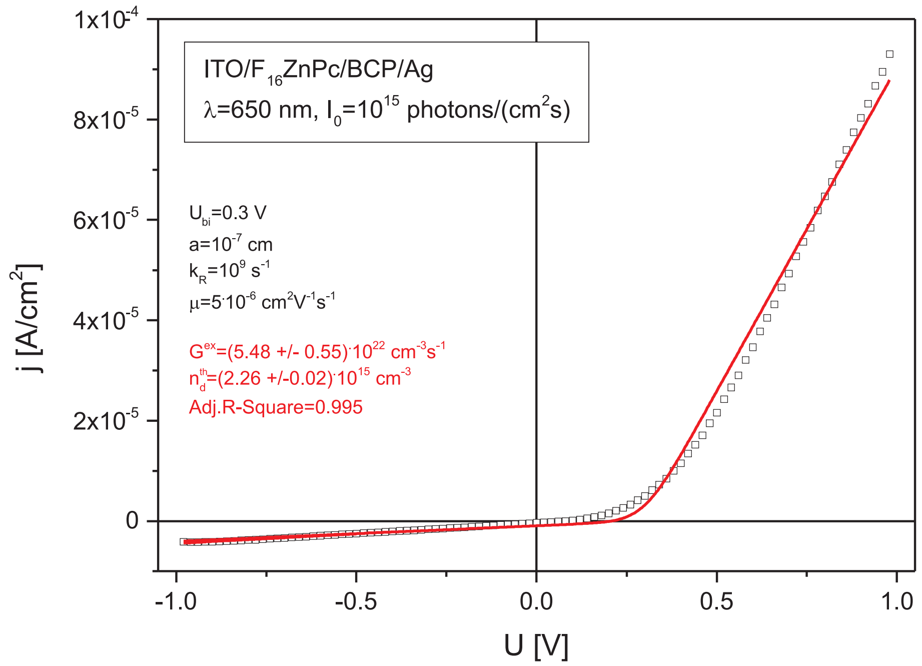

Figure 6.7: Current-volatge characteristics of the ITO/F_{16}ZnPc/BCP/Ag cell measured under monochromatic illumination of λ=650 nm (B). U is the potential applied to the ITO electrode. Red lines and values of U_{bi}, n_d^{th} and G^{ex} marked in red result from fitting the experimental data to Eq. 4.39 assuming that $k_R = 10^9$ 1/s, $a = 10^{-7}$ cm and $\mu = 5 \cdot 10^{-6}$ $\mathrm{cm}^2/(\mathrm{Vs})$.

matic illumination of wavelength λ=650 nm and light intensity of $I_0 = 10^{15}$ photons/ (cm^{2}s) (Figs. 6.6 and 6.7). These dependencies confirm our presumptions on the type of electric contacts between electrodes and the F_{16}ZnPc layer.

Both collected curves were fitted to the CFA model of a single layer cell model, i.e. to Eqs. 4.39 and 4.40. It seems that a perfect fit, for which the adjusted R-Square equals 1, was obtained for the dark j-V curve when the following values of monomolecular recombination constant k_R, width of the generation layer a and electron mobility μ were assumed

- $k_R = 10^9$ s^{-1}, $a = 10^{-7}$ cm, $\mu = 5 \cdot 10^{-6}$ cm^{2}V^{-1}s^{-1}.

In this case the following values of the built-in electric field and the concentration of electrons at the rear contact were found

- $U_{bi} = 0.3$ V and $n_d^{th} = 2.09 \cdot 10^{15}$ cm^{-3} .

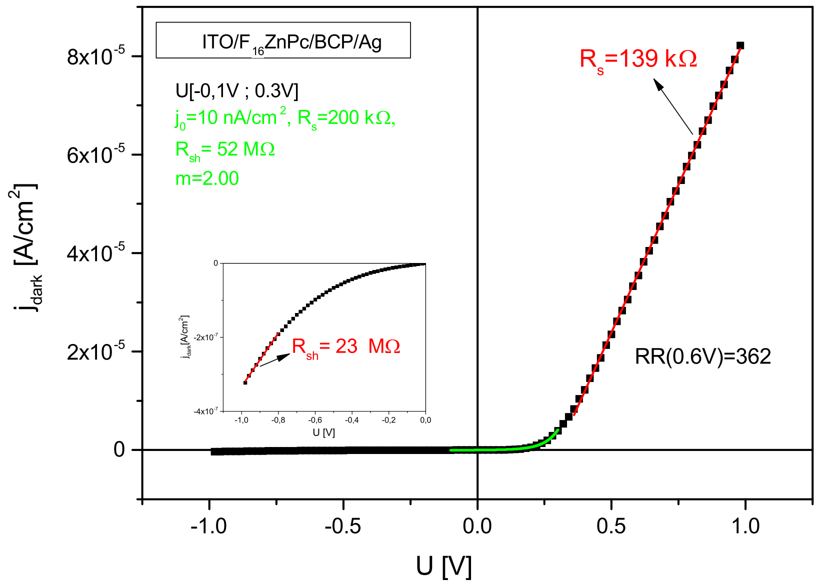

Figure 6.8: Current-volatge characteristics measured in the dark (black squares) for the ITO/F_{16}ZnPc/BCP/Ag cells. U is the potential applied to the ITO electrode. Green line and values of j_0 and m result from fitting the experimental data to Eq. 3.15 in the voltage range from -0.1 V to 0.3 V, while red lines refer to linear fits enabling estimation of resistances of the cell, RR is the rectification ratio. The inset presents magnification of the current-voltage curve under reverse bias.

It is worth noting, that although the adjusted R-Square equals 1 the fitted curve does not match the measured current-voltage characteristics under reverse bias (see the inset of the graph), for which this current is neither constant nor linearly dependent on the applied voltage. Nevertheless, quite a good fit, for which the adjusted R-Square equal to 0.995, was obtained for current-voltage characteristics of the illuminated cell for the same values of k_R, a, μ, U_{bi} and the following values of photogeneration rate and thermal concentration of electrons at the rear contact respectively

- $G^{ex} = (5.48 \pm 0.55) \cdot 10^{22}$ cm^{-3}s^{-1} and $n_d^{th} = (2.26 \pm 0.02) \cdot 10^{15}$ cm^{-3} .

This time, the CFA model matches well the experimental data collected in the whole range of applied voltages except for a narrow range of voltages around the open-circuit voltage. The measured values of this parameter, short-circuit current

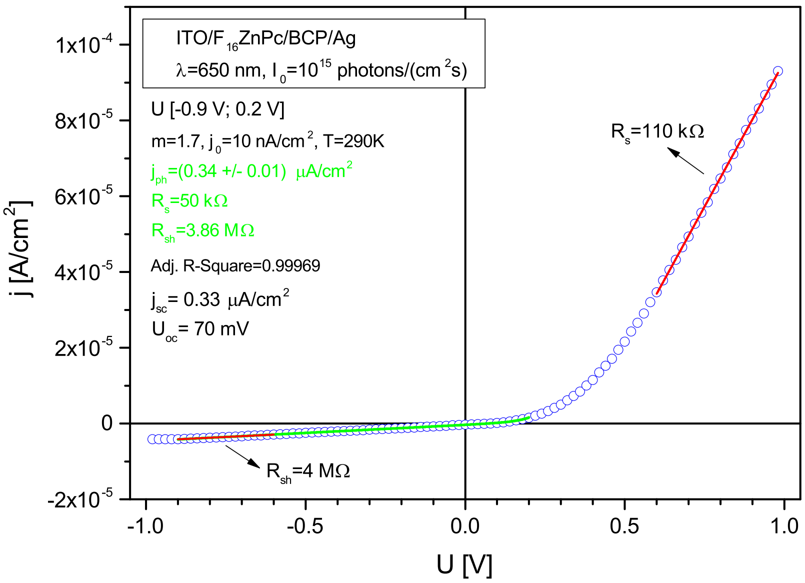

Figure 6.9: Current-volatge characteristics measured under monochromatic illumination of λ=650nm and intensity 10^{15} photons/$\mathrm{cm}^2\mathrm{s}^{-1}$ for the ITO/F$_{16}$ZnPc/BCP/Ag cells. U is the potential applied to the ITO electrode. Green line and values of j_{ph}, R_s and R_{sh} show the results of fitting the experimental data to Eq. 3.15 in the voltage range from -0.9 V to 0.2 V for m=1.7, T=290K and j_0=10 $\mathrm{nA/cm}^2$.

density and the calculated value of the fill factor under investigated illumination conditions are

- $U_{oc} = 0.07$ V, $j_{sc} = 0.33$ μAcm^{-2} and FF=0.3 ,

while the ones resulting from the CFA model are

- $U_{oc} = 0.21$ V, $j_{sc} = 0.93$ μAcm^{-2} and FF=0.34 .

Such dissimilarity between these values may follow from the fact, that the CFA model does not fit to the experimental current-voltage relation in the voltage range around the open-circuit voltage.

Knowing the value of photogeneration rate we may calculate the value of electron collection efficiency φ_C at short-circuit. The values of φ_C estimated from Eqs. 4.59 and 4.56 are consistent with each other, as they are equal to $\varphi_C \approx 0.106$ %

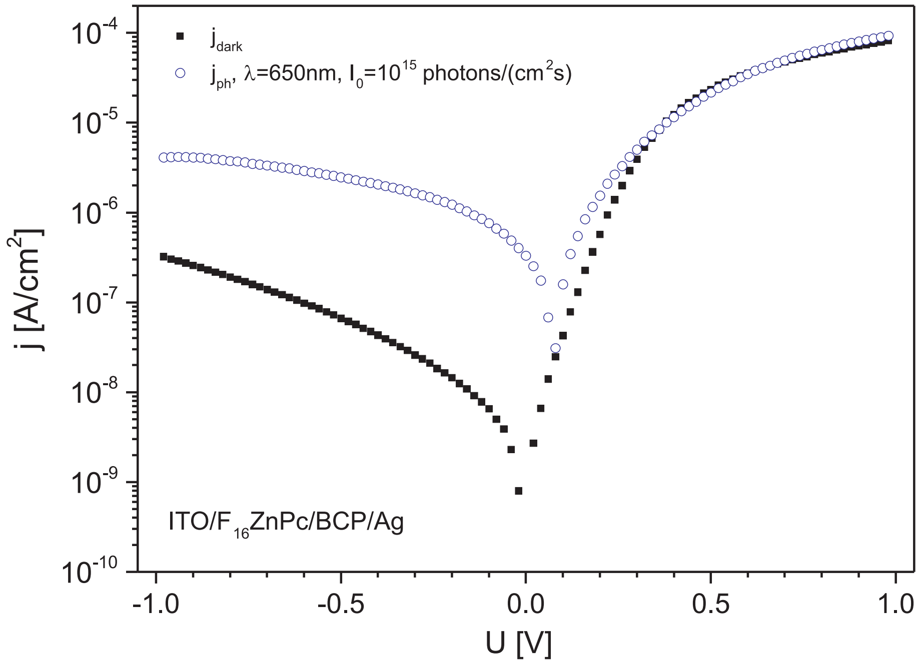

Figure 6.10: Current-volatge characteristics measured in the dark (black squares) and under monochromatic illumination of λ=650 nm and intensity 10^{15} photons/(cm^{2}s) (open circles) for the ITO/F_{16}ZnPc/BCP/Ag cells with a 140 nm-thick phthalocyanine layer.

and $\varphi_C \approx 0.1$ % respectively. This means, that the surface recombination velocity v_R is about three orders of magnitude greater than the drift velocity v_d. Such a large disproportion between these velocities arises from high recombination constant and low mobility of free charge carriers that bring about low electron collection efficiency and account for poor performance of the investigated ITO/F_{16}ZnPc/BCP/Ag system, for which the maximum power conversion efficiency under investigated illumination conditions is very low and equal to about 2.3·10^{-4}%.

Lets now try to evaluate the obtained current-voltage characteristics using the SEC model. As it was mentioned, shape of the dark j-V curve under revers bias is far from ideal diode behavior (see the insets of Figs. 6.6 and 6.8), while under forward bias greater than 0.35 V current-voltage relation becomes linear. In the intermediate voltage region ranging from -0.1 V to 0.3 V the $j_{dark}(U)$ curve can be fitted to the equation obtained for the Shockley equivalent circuit (Eq. 3.15). Parameters that are obtained from such fit are:

- saturation current density j_0,
- diode ideality factor m,
- series resistance R_s,
- shunt resistance R_{sh}.

Ranges of magnitude of these parameters should be somehow predetermined before the fitting process, since many different sets of these parameters may give a good fit to the same model. Some methods of solar cell parameter extraction can be found in [39, 111–113]. Herein, the following procedure based on the SEC model was employed:
Since the current flowing through the cell varies with voltage in the following manner

$$J = \frac{R_{sh}}{R_{sh} + R_s} \left\{ J_0 \left[exp \left(\frac{e(U - JR_s)}{mkT} \right) - 1 \right] + \frac{U}{R_{sh}} - J_{ph} \right\} \tag{6.6}$$

the first derivative of the current with respect to electric bias yields

$$\frac{\mathrm{d}J}{\mathrm{d}U} = \frac{\frac{1}{R_{sh}} + \frac{eJ_0A}{mkT}}{R_s(\frac{1}{R_{sh}} + \frac{eJ_0A}{mkT}) + 1} , \tag{6.7}$$

where

$$A = \exp \left[\frac{e(U - JR_s)}{mkT} \right] . \tag{6.8}$$

Therefore, if this derivative is a constant, two different cases can be distinguished:

a) $\frac{1}{R_{sh}} \gg \frac{eJ_0A}{mkT}$, which means that $\frac{\mathrm{d}J}{\mathrm{d}U} \approx \frac{1}{R_s+R_{sh}}$

b) $\frac{1}{R_{sh}} \ll \frac{eJ_0A}{mkT}$, thus $\frac{\mathrm{d}J}{\mathrm{d}U} \approx \frac{1}{R_s}$

The first case regards the reverse bias, while the second is characteristic for the forward bias, so if linear sections of the current-voltage curve may be found at these two polarization directions, shunt and series resistances may be preliminarily estimated knowing the slopes of these linear sections. Moreover, if we rewrite Eq. 6.7 into the following form

$$x = \frac{G}{1 - GR_s} - \frac{1}{R_{sh}} , \tag{6.9}$$

where $x = eJ_0A/(mkT)$ and $G = \mathrm{d}J/\mathrm{d}U$, we will notice that

$$\ln x = \ln\frac{eJ_0}{mkT} + \frac{e}{mkT}(U - JR_s)\ . \tag{6.10}$$

Hence, if we calculate G from the set of the experimental data and use it to calculate x knowing the estimated values of shunt and series resistances, we should be able to estimate the diode ideality factor m and saturation current J_0 by plotting the natural logarithm of x versus $(U - JR_s)$. These results are regarded as initial values in the process of fitting the experimental current-voltage plots into the SEC model. The aforementioned approach may also be applied to current-voltage curves measured under illumination as long as the photogeneration current J_{ph} does not depend on the applied voltage.

Approximated value of the series resistance of the ITO/F_{16}ZnPc/BCP/Ag cell, equal to 139 kΩ, was calculated from the linear part of the curve shown in Fig. 6.8. Afterwords, approximated value of the shunt resistance, equal to 23 MΩ, was found from the short linear part of the curve under reverse bias. Since, as it was already pointed out, under such bias current-voltage curve diverges from the ideal diode behavior, the value of shunt resistance has a relatively large error and therefore x is not well defined in this case. Nevertheless, it was possible to estimate the values of m and j_0 by plotting $\ln x$ as a function of $(U - JR_s)$, which is the voltage applied to the diode. In this fashion m=1.44 and j_0=2.5 nA/cm^2 were obtained. This set of 4 parameters, i.e.

- R_s=139 kΩ, R_{sh}=23 MΩ, j_0=2.5 nA/cm^2 and m=1.44

was used in the subsequent fitting process. The best fit (shown in Fig. 6.8), for which the Adjusted R-square equals 0.994, was obtained for

- R_s=200 kΩ, R_{sh}=52 MΩ, j_0=10 nA/cm^2 and m=2.

Such a large value of the dark saturation current density accounts for the low open-circuit voltage value, while diode ideality factor equal to 2 suggests, that free charge carriers undergo trap-assisted recombination (SRH recombination) in the vicinity of the active interface.

The same method of predetermination of parameters was applied to the current-voltage relation obtained under monochromatic illumination of λ=650 nm and intensity $I_0 = 10^{15}$ photons/(cm^{2}s) shown in Fig. 6.9, but although it seems that both resistances, i.e. R_s=110 kΩ, R_{sh}=3.74 MΩ, were quite well defined for this case reliable values of m and j_0 were not found. Nevertheless, almost a perfect fit of the current-voltage curve for which the adj. R-square=0.9997 was obtained for the saturation current density of 10 nA/cm^2, calculated for this cell in the dark and the following set of parameters

- m=1.7, R_s=108 kΩ, R_{sh}=3.8 MΩ and j_{ph}=0.34 μA/cm^2.

It is worth noting, that these values are reliable, since values of both resistances are consistent with the ones found from the slopes of the linear sections of the current-voltage curve, while the obtained photogeneration current density is a bit greater than the short-circuit current density, which is equal to 0.33 μA/cm^2 under regarded illumination conditions. Estimated values of dark saturation current density, photogeneration current density, diode ideality factor under illumination and Eq. 4.22 modified by introduction of the diode ideality factor m allow for calculation of the open-circuit voltage

$$U_{oc} = \frac{mkT}{e} \ln\left(1 + j_{ph}/j_0\right) \approx 150 \text{ mV} \,. \tag{6.11}$$

This value is more than twice greater than the experimental one equal to 70 mV, but lower than the one found from the CFA model.

One must bare in mind, that the value of adjusted R-square does not determine whether the applied model is good or not, and although the fit to the SEC model seems to be practically perfect, the method of evaluating the diode ideality factor and saturation current failed in this case, which suggests that even if this model can be applied to the investigated system, photogeneration current might be dependent on voltage. Moreover, if we take a look at the revers current under illumination, we will notice that it seems to be a linear function of the applied voltage. Such a linear current-voltage characteristics under illumination at reverse bias was observed in ZnPc/C$_{60}$ cells and this phenomenon was attributed to additional hole injection at the electron contact resulting from illumination of the fullerene layer and therefore the loss of selectivity of this contact [12]. This phenomenon was called photoshunt. Authors of this work stated that presence of such photoshunt resulting from photoconductivity is an important loss mechanism limiting the fill factor of heterojunction solar cells. Since in case of the ITO/F_{16}ZnPc/BCP/Ag cells theF_{16}ZnPc layer is rather thick and spectral response of the short-circuit current suggests, that the front contact is the only active contact, there should be no photoshunt. However, it is evident that illumination of the cell causes a major drop of a shunt resistance of the cell. This could be related to bulk generation of free charge carriers, light induced detrapping process or interactions between free charge carriers or excitons. Furthermore, the value of series resistance found at a forward bias above the powergenerating region under illumination is about 20 % lower than the one found in the dark, that may follow from additional light induced mechanism of free charge carrier generation, such as detrapping of charge carriers. The diode ideality factor m found for illuminated cells is lower than the one obtained for the dark curve, which suggests that under illumination free charge carriers may undergo monomolecular trap-assisted recombination, as well as, bimolecular recombination.

It is worth noting, that the dark saturation current related to thermal generation of free charge carriers should not depend on illumination or its lack, and indeed in case of the investigated ITO/F_{16}ZnPc/BCP/Ag cells values of j_0 evaluated from both current-voltage plots are identical. However, if we set the value of series resistance in the dark to be equal to the one found from the slope of the current-voltage curve then value of j_0 obtained from the fit to the SEC model will be equal to 18 nA/cm^2 and will differ from the one obtained under illumination. If we present j_{dark} vs voltage and j under illumination vs voltage on the same graph in the log-log scale (Fig. 6.10) we will notice, that under higher forward bias these two plots practically overlap each other. This is consistent with Eq. 3.11, according to which $j \approx j_{dark}$ when dark current injected from electrodes is much greater than the photogenerated one.

Lets know try to compare both models applied herein, i.e. the CFA model and the SEC model. Unfortunately, the adjusted R-square is not a parameter that allows for determination of more suitable model. We may only notice, that the CFA model fits the experimental current-voltage relation in a much wider range of voltages than the SEC one does. Although these models seem to differ a lot, some similarities may be found that allow for interpretation of the parameters characteristic for the SEC model in terms of the ones describing the CFA model:

- Series and shunt resistances, that characterize the behavior of an ideal diode, can be derived from Eqs. 4.44, 4.45 and 4.48. In the dark

  $$\frac{1}{AA(R_s + R_{sh})} = \frac{\mu e G^{th}}{k_R d} \ , \tag{6.12}$$

  whereas under illumination

  $$\frac{1}{AA(R_s + R_{sh})} = \frac{\mu e G^{ex}}{k_R d} \ , \tag{6.13}$$

  while disregarding illumination

  $$\frac{1}{AAR_s} = \frac{\mu e n_d^{th}}{d} = \frac{\mu e G^{th}}{k_R d \exp[-eU_{bi}/(kT)]} \ , \tag{6.14}$$

  where AA is the active area of the sample. Thus,

  $$R_s = \frac{d}{\mu e n_d^{th}} AA^{-1} \ , \tag{6.15}$$

  $$R_{sh}^{dark} = \frac{k_R d}{\mu e G^{th}} \left(1 - exp[-eU_{bi}/(kT)]\right) AA^{-1} \ , \tag{6.16}$$

  while

  $$R_{sh}^{ill} = \frac{k_R d}{\mu e} \left(\frac{1}{G^{ex}} - \frac{1}{n_d^{th} k_R} \right) AA^{-1} \ . \tag{6.17}$$

  These equations indicate, that series resistance of a cell is constant, while shunt resistance strongly depends on illumination conditions, i.e. decreases with increasing light intensity, which is consistent with the results of our measurements. Moreover, both these resistances depend on mobility of free charge carriers, organic layer thickness, concentration of free charge carriers at electrodes in thermal equilibrium and the built-in field. Since a good diode is a diode of high shunt resistance and low series resistance, R_{sh}^{dark}/R_s and R_{sh}^{ill}/R_s ratios should be as high as possible. According to equations given above, these ratios are

  $$\frac{R_{sh}^{dark}}{R_s} = \mathrm{e}^{eU_{bi}/(kT)} - 1 \ , \tag{6.18}$$

while

$$\frac{R_{sh}^{ill}}{R_s} = \frac{k_R n_d^{th}}{G^{ex}} - 1 = \frac{k_R n_0}{G^{ex}} \, \mathrm{e}^{eU_{bi}/(kT)} - 1. \tag{6.19}$$

Thus, it seems that prerequisites for good quality diodes are: high built-in electric field, i.e. high value of the difference between electrode work functions, and high free charge carrier concentration at the ohmic contact. One must remember, that according to the CFA model high value of the built-in voltage is essential for providing high free charge carrier collection efficiency, in case of cells in which mobility of free charge carriers is low and recombination of these carriers is fast (see Fig. 4.3). R_{sh}/R_s ratios can be calculated knowing U_{bi}, k_R and G^{ex} or resistances, extracted from the fits to the CFA or SEC models, respectively. These values are

- $\frac{R_{sh}^{dark}}{R_s} \approx 1.6 \cdot 10^5$ (CFA model) or $\frac{R_{sh}^{dark}}{R_s} \approx 260$ (SEC model)

while under monochromatic illumination of 10^{15} photons/(cm^{2}s)

- $\frac{R_{sh}^{ill}}{R_s} \approx 40$ (CFA model) or $\frac{R_{sh}^{ill}}{R_s} \approx 35$ (SEC model).

The values of these ratios obtained in the dark on the basis of regarded models are inconsistent with each other (it may follow from the non ideal shape of the dark j-V curve under reverse bias), while the ones found for the illuminated cell stand in a good agreement with each other. Nevertheless, these results show that the increase in the incident light intensity brings about a serious deterioration of the performance of the cell, since under relatively low illumination intensity a rapid drop of the R_{sh}/R_s ratio is observed.

- If the diode ideality factor equals m the following relation results from the modified Eq. 4.22 and Eq. 4.50 under the assumption of sufficient illumination intensity (i.e. if $G^{ex} \gg G^{th}$ and $j_{ph} \gg j_0$)

$$\frac{G^{ex}}{G^{th}} = \left(\frac{j_{ph}}{j_0}\right)^m . \tag{6.20}$$

In the CFA model eaG^{ex} is the maximum current density flowing through an ideal illuminated cell, characterized by high mobility of free charge carriers and low value of their recombination constant, while in the SEC model j_{ph}

determines the density of the photogeneration current before any loss processes. Therefore, eaG^{ex} seems to be analogous to j_{ph} and hence, eaG^{th}, that is the density of the current resulting from thermal generation of free charge carriers in the generation layer, should be analogous to the saturation current density j_0 characteristic for an ideal diode. However, the equation given above shows, that photogeneration rate/thermal generation rate ratio is proportional to photocurrent/saturation current ratio raised to power m dependent on recombination processes. In case of the ITO/F_{16}ZnPc/BCP/Ag cells

- $G^{ex}/G^{th} \approx 4000$,

while

- $(j_{ph}/j_0)^m \approx 400$,

so these two ratios differ by one order of magnitude. Such discrepancy might be a result of inaccuracy of parameters extracted from the fits, especially m and U_{bi}, since both ratios are very sensitive to these parameters.

6.2 Single layer cells with the CuI anode

ITO/F_{16}ZnPc/BCP/Ag cells have shown rather poor performance, though as it will be presented later on, the F_{16}ZnPc/BCP/Ag contact is ohmic, while the ITO/F_{16}ZnPc heterojunction is capable of dissociation of excitons. Therefore, in order to verify the applicability of F_{16}ZnPc in other single layer structures, cells comprising a thin layer of cuprous iodide (CuI) instead of ITO were fabricated. This section presents analysis of photovoltaic phenomenon in single-layer CuI/F_{16}ZnPc/BCP/Ag cells. Energy level diagram of materials forming this system is shown in Fig. 6.11. The thickness of the F_{16}ZnPc layer in the investigated cells was 80 nm.

6.2.1 Short-circuit current and open-circuit voltage action spectra

Spectral response of the short-circuit current collected under illumination $I_0 = 10^{14}$ photons/(cm^{2}s) is shown in Fig. 6.12. Under illumination through the front

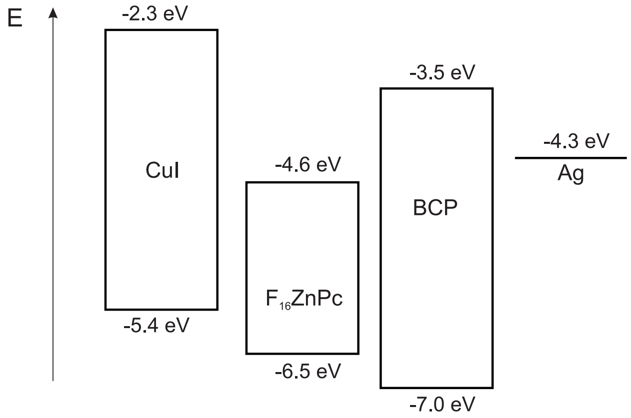

Figure 6.11: Energy level diagram of materials forming the CuI/F_{16}ZnPc/BCP/Ag cells.

electrode (in this case I_0 is the intensity of light at the CuI/F_{16}ZnPc heterojunction) j_{sc} follows the absorption of the phthalocyanine layer in the whole presented spectral range. Moreover, under illumination from the opposite side (in this case I_0 is the intensity of light at the F_{16}ZnPc/BCP heterojunction), j_{sc} is symbatic as long as absorption of the F_{16}ZnPc layer is poor and rather antibatic in case of strong absorption of this material. Hence, the CuI/F_{16}ZnPc junction seems to be the active junction in the CuI/F_{16}ZnPc/BCP/Ag system. However, if we take a closer look at the spectral response of short-circuit current obtained under illumination from the Ag side around wavelengths of 400 nm and 560 nm, where absorption of CuI is significant, we will notice that j_{sc} seems to follow the absorption of CuI, which suggests that photogeneration of free charge carriers as a result of exciton dissociation at the CuI/F_{16}ZnPc heterojunction might not be the only mechanism of free charge carrier generation in the regarded system. Another mechanism of free charge carrier generation can be related to light absorption in the CuI layer related to band to band transitions. This would mean that this layer not only forms a rectifying contact, enabling dissociation of excitons and collection of holes, but it is also one of the active materials. In order to verify this fact, spectral dependence of short-circuit current under illumination from the front side at the same value of light intensity equal to 10^{14} photons/(cm^{2}s) but at the glass/CuI junction was measured (Fig. 6.13). In this case, a peak of j_{sc} followed by a local minimum of the current around 400 nm, where absorption of CuI reaches its local maximum, is clearly pronounced. The same behavior was observed in the open-circuit voltage

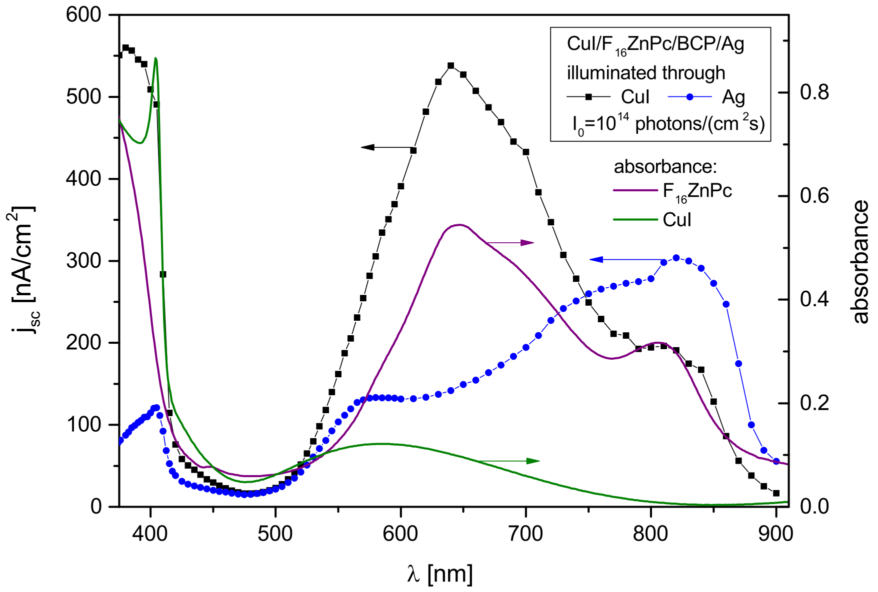

Figure 6.12: Short-circuit current density as a function of wavelength of the incident light measured for CuI/F$_{16}$ZnPc/BCP/Ag cell at light intensity $I_0 = 10^{14}$ photons/(cm^{2}s), when the cell was illuminated from the CuI (squares) or Ag (circles) side. Light intensity I_0 is the intensity of light incident on the CuI/F$_{16}$ZnPc interface (when illuminated through CuI) and on the F$_{16}$ZnPc/BCP interface (under illumination through Ag).

action spectra (Fig. 6.14). However, the origin of these peaks and local minima can be interpreted in two different ways:

1. observed minima follow from the decrease in light intensity at the active CuI/F$_{16}$ZnPc heterojunction caused by absorption of CuI,
2. peak values result from generation of free charge carriers in the CuI layer.

It is not easy to decide which of these interpretations is correct basing solely on the action spectra, since it is rather hard to determine whether and how much the peaks of CuI absorption and these of j_{sc} and U_{oc} should be shifted with respect to each other to prove one of these interpretations right. Therefore, collected action spectra are inconclusive and other measurements have to be carried out to verify the role of CuI in the CuI/F$_{16}$ZnPc/BCP/Ag cells.

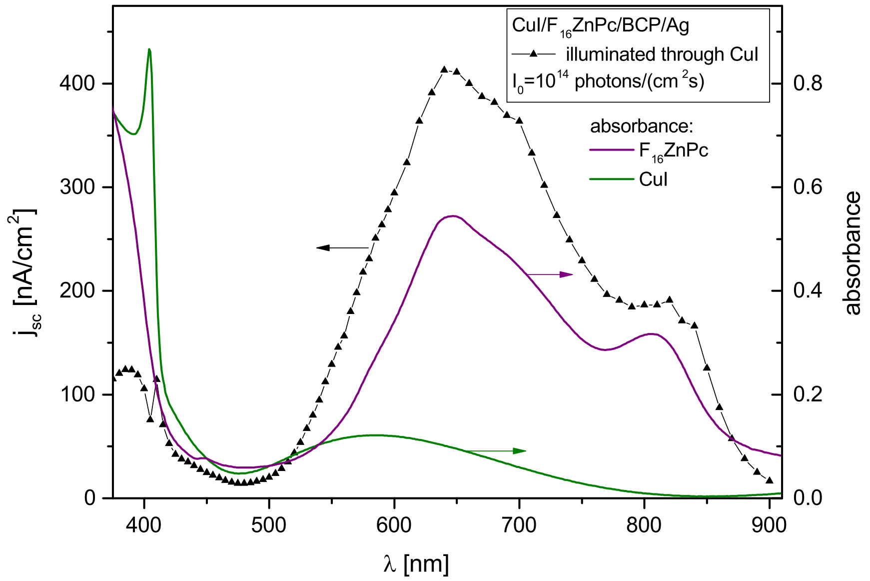

Figure 6.13: Spectral response of short-circuit current measured at light intensity $I_0 = 10^{14}$ photons/(cm^{2}s) for CuI/F$_{16}$ZnPc/BCP/Ag cell, when the cell was illuminated from the CuI side. Herein light intensity I_0 is the intensity of light incident on the glass/CuI interface.

6.2.2 Illumination intensity dependence of short-circuit current and open-circuit voltage

In order to verify the influence of light intensity on processes of generation and recombination of free charge carriers in CuI/F$_{16}$ZnPc/BCP/Ag cells, short-circuit current density and open-circuit voltage were measured as a function of this parameter. Results of these measurements carried out under monochromatic illumination of wavelength λ=650 nm, corresponding to the absorption peak of phthalocyanine layer, are shown in Figs. 6.15 and 6.16. Herein, I_0 is the intensity of light at the glass/CuI interface. As one can see form the log-log plot of j_{sc} vs I_0, even at relatively high light intensities short-circuit current is practically a linear function of light intensity, since the slope b of the curve is close to 1 $(b = 0.94)$. Therefore, a single-photon absorption is responsible for excitation of the organic layer, while monomolecular recombination of free charge carriers is a dominant quenching process under short-circuit conditions up to $I_0 = 10^{16}$ photons/(cm^{2}s).

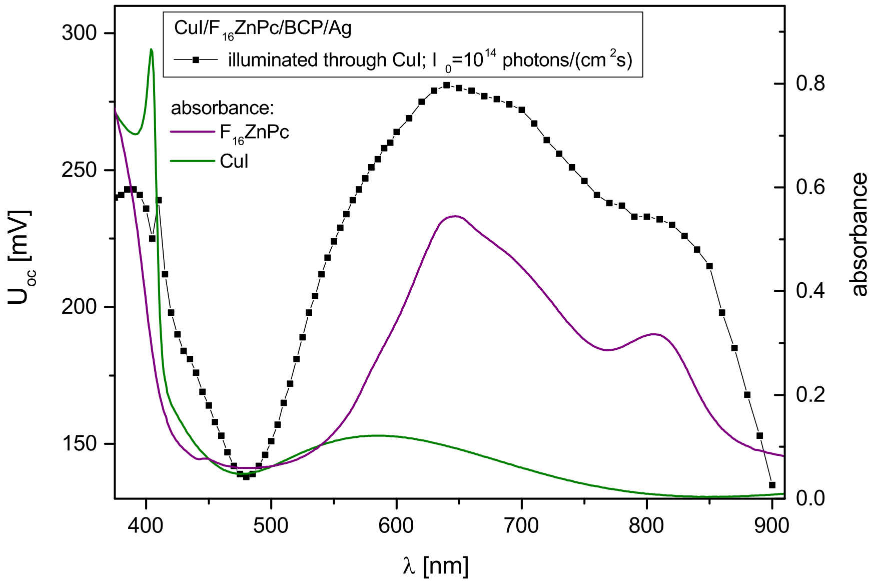

Figure 6.14: Spectral response of open-circuit voltage measured at light intensity $I_0 = 10^{14}$ photons/(cm^{2}s) for CuI/F$_{16}$ZnPc/BCP/Ag cell, when the cell was illuminated from CuI side. Herein light intensity I_0 is the intensity of light incident on the glass/CuI interface.

The slope of the $U_{oc}(I_0)$ semi-log curve gives the value of a prefactor m close to 1.6, that can be interpreted as the diode ideality factor, suggesting the presence of monomolecular trap-assisted recombination of free charge carriers at the CuI/F$_{16}$ZnPc interface and bimolecular recombination in the bulk of the phthalocyanine layer.

Knowing the dominant type of recombination at short-circuit the problem of determination of the role of CuI in CuI/F$_{16}$ZnPc/BCP/Ag cells, stated in the previous subsection, can be addressed. Lets assume that absorption of light by CuI does not result in free charge carrier generation, and therefore it does not contribute to the current flow causing only a decrease in the light intensity reaching the CuI/F$_{16}$ZnPcinterface. In such case, the ratio of short-circuit current measured when light intensity I_0 is the incident light intensity at the glass/CuI interface and short-circuit current measured when I_0 is the intensity of light incident on the CuI/F$_{16}$ZnPc interface, namely j_{sc1}/j_{sc}, should be equal to the ratio of light intensities at the CuI/F$_{16}$ZnPc interface in these two cases raised to power b=0.94

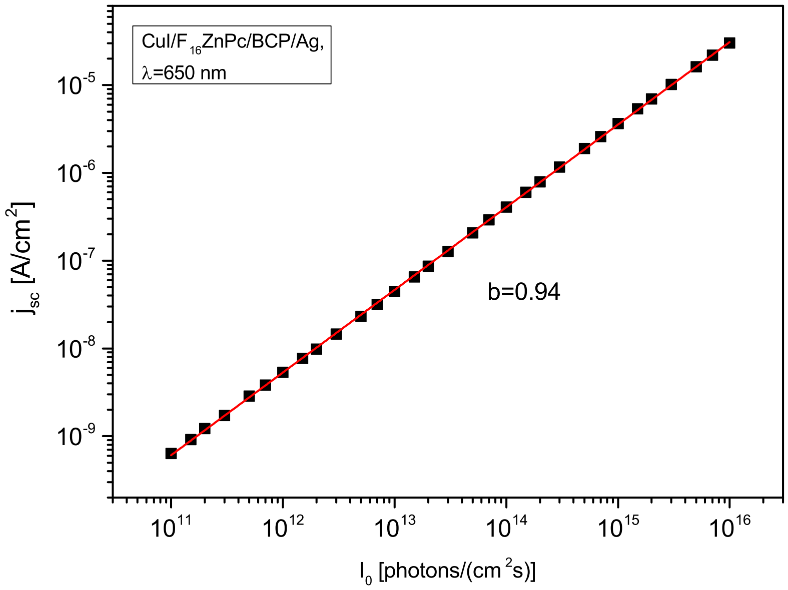

Figure 6.15: Light intensity dependence of short-circuit current density for CuI/F_{16}ZnPc/BCP/Ag cells. Cells were illuminated from the CuI side with monochromatic light of wavelength λ=650 nm. I_0 is the intensity of light at the glass/CuI interface.

accounting for recombination of free charge carriers, i.e. $(I_{01}/I_0)^{0.94}$. This relation follows from the fact, that $j_{sc} \sim {I_0}^b$, and in this case $b = 0.94$ in the whole investigated range of light intensities. Light intensity I_{01} at the CuI/F_{16}ZnPc junction with respect to illumination intensity I_0 incident on the glass/CuI interface is found knowing the absorbance of the CuI layer. These two ratios calculated for illumination intensity $I_0 = 10^{14}$ photons/(cm^{2}s) in the range of wavelengths from 350 nm to 900 nm are shown in Fig. 6.17. As one can see, their values match each other very well in the whole spectral range, that confirms the assumption made above about the role of CuI in the investigated system: CuI forms an active junction with the phthalocyanine layer, but its absorption does not enhance photogeneration of free charge carriers. It is worth noting, that the largest deviations between the plotted parameters are found in spectral ranges corresponding to low short-circuit currents and may be attributed to experimental errors arising during measurements of such low current values.

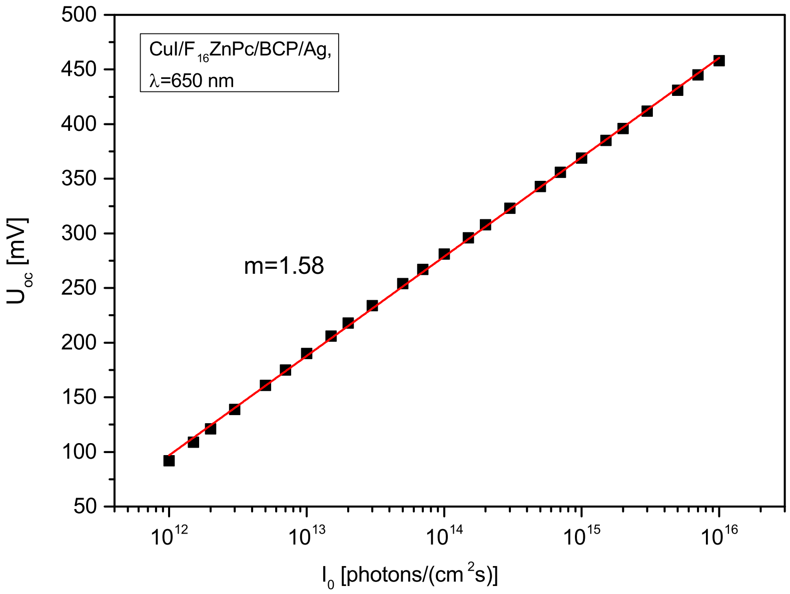

Figure 6.16: Light intensity dependence of open-circuit voltage for CuI/F$_{16}$ZnPc/BCP/Ag cells. Cells were illuminated from the CuI side with monochromatic light of wavelength λ=650 nm. I_0 is the intensity of light at the glass/CuI interface.

6.2.3 Current-voltage characteristics

Current-voltage characteristics were collected in the dark, under monochromatic illumination of wavelength λ=650 nm and light intensity of $I_0 = 10^{15}$ photons/(cm^{2}s) as well as under white light illumination of intensities equal to 20 mWcm^{-2} and 100 mWcm^{-2}. Schematic diagram of energy levels of materials forming the investigated cells was shown in Fig. 6.11. Analogically to the previous type of cells with the ITO anode, we may point out the front electrode, i.e. CuI, as the active rectifying contact for electrons. Therefore, terms forward and reverse bias for cells with the CuI anode refer to the same polarization directions as in case of cells comprising the ITO layer. Hence, currents flowing through CuI/F$_{16}$ZnPc/BCP/Ag cells at positive polarization of CuI with respect to Ag are expected to be much higher than the ones obtained for the opposite polarization. Relation between the dark current density and applied voltage obtained for CuI/F$_{16}$ZnPc/BCP/Ag cells is shown in Fig. 6.18 and it is consistent with our expectations. Rectifying behav-

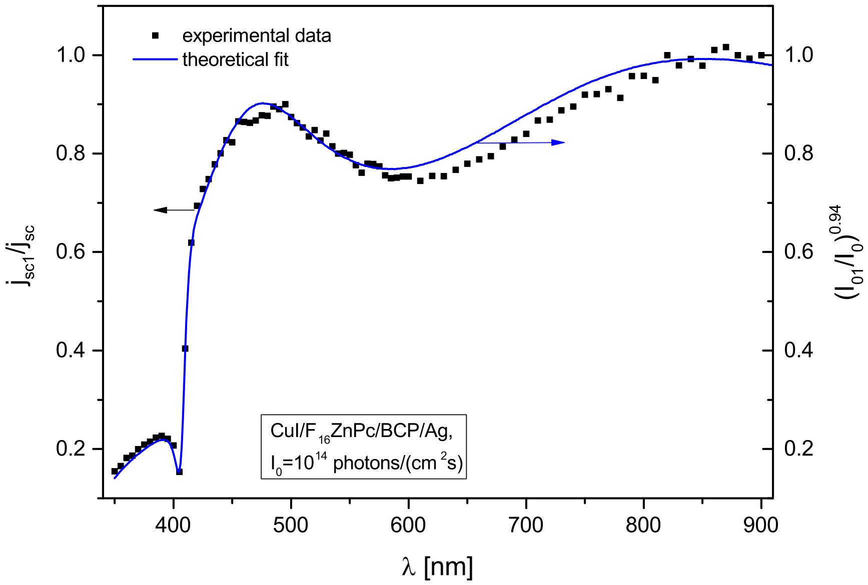

Figure 6.17: j_{sc1}/j_{sc} - ratio of short-circuit current densities measured for CuI/F$_{16}$ZnPc/BCP/Ag cells illuminated through CuI with light of intensity $I_0 = 10^{14}$ photons/(cm^{2}s) at the glass/CuI and the CuI/F$_{16}$ZnPc interfaces; $(I_{01}/I_0)^{0.94}$ - calculated ratio of light intensities at CuI/F$_{16}$ZnPc interface in these two cases raised to power b=0.94.

ior is quite well pronounced. The value of RR found at ± 0.6 V is equal to 705. All collected current-voltage characteristics, presented in Figs. 6.18-6.21 were fitted to the CFA model of a single layer cell, i.e. to Eqs. 4.39 and 4.40. The same values of free electron mobility, recombination constant and width of the generation layer as in case of single layer cells with the ITO anode, i.e. $\mu = 5 \cdot 10^{-6}$ cm^2(Vs)$^{-1}$, $k_R = 10^9$ s^{-1} and $a = 10^{-7}$ cm, were used during the fitting process. The following values of the built-in potential, concentration of free electrons at the rear contact and photogeneration rate were determined from the best fit of each experimental curve:

- in the dark
  $U_{bi} = (0.54 \pm 0.01)$ V, $n_d^{th} = (1.57 \pm 0.04) \cdot 10^{15}$ cm^{-3}
- under monochromatic illumination of wavelength λ=650 nm, and intensity I_0= 10^{15} photons/(cm^{2}s)

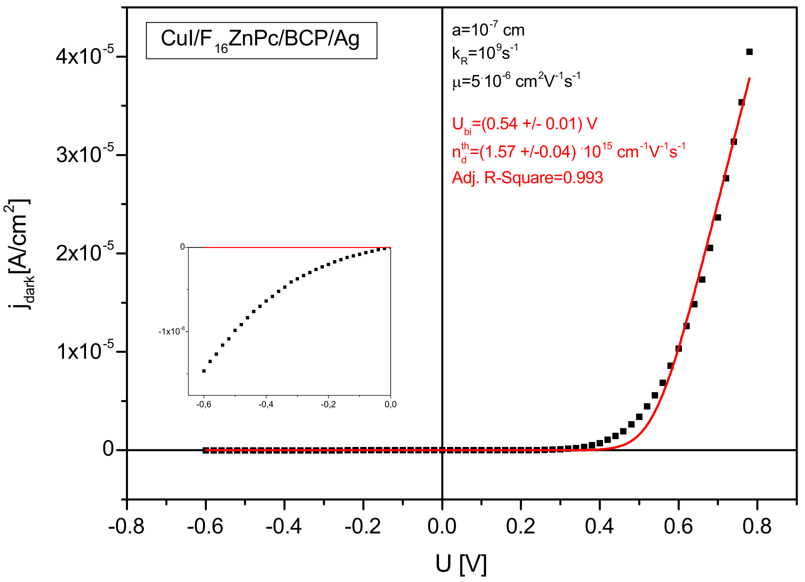

Figure 6.18: Dark current-voltage characteristics of the CuI/F$_{16}$ZnPc/BCP/Ag cell. U is the potential applied to the CuI electrode. Red lines and values of U_{bi} and n_d^{th} marked in red result from fitting the experimental data to Eq.4.40 assuming that $k_R = 10^9$ s^{-1}, $a = 10^{-7}$ cm and $\mu = 5 \cdot 10^{-6}$ cm^2/(Vs).

$U_{bi} = (0.52 \pm 0.01)$ V, $n_d^{th} = (2.85 \pm 0.06) \cdot 10^{15}$ cm^{-3},
$G^{ex} = (6.1 \pm 0.3) \cdot 10^{22}$ cm^{-3}s^{-1}

- under white light illumination of intensity I_0=20 mW/cm^2
  $U_{bi} = (0.57 \pm 0.01)$ V, $n_d^{th} = (5.67 \pm 0.15) \cdot 10^{15}$ cm^{-3},
  $G^{ex} = (1.85 \pm 0.01) \cdot 10^{24}$ cm^{-3}s^{-1}

- under white light illumination of intensity I_0=100 mW/cm^2
  $U_{bi} = (0.56 \pm 0.01)$ V, $n_d^{th} = (4.62 \pm 0.04) \cdot 10^{15}$ cm^{-3},
  $G^{ex} = (3.78 \pm 0.02) \cdot 10^{24}$ cm^{-3}s^{-1}

Just as in case of single layer cells with the ITO electrode, the CFA model does not match the dark current-voltage relation under reverse bias (see the inset of Fig. 6.18). The fit is far from perfect also in the narrow voltage range around the derived value of U_{bi}. Fits found for the current-voltage curves measured under illumination of the cell are quite good, as they follow the experimental data

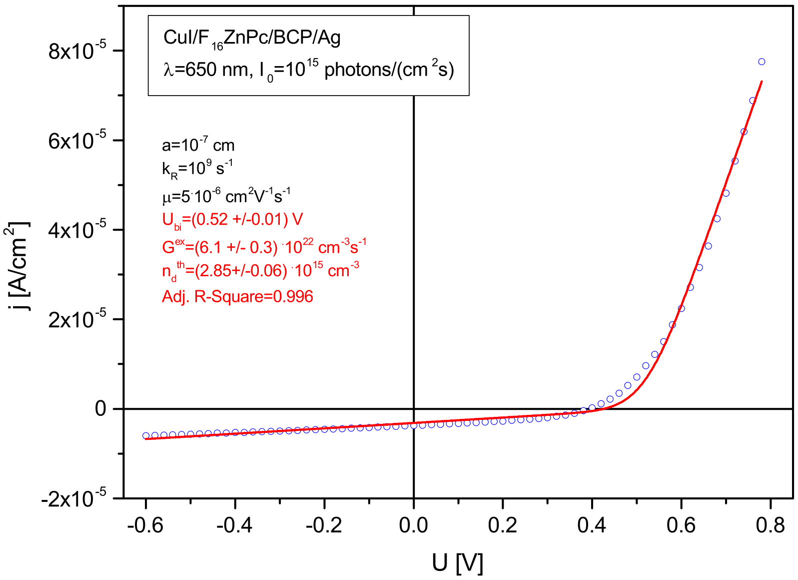

Figure 6.19: Current-voltage characteristics of the CuI/F_{16}ZnPc/BCP/Ag cell under monochromatic illumination of λ=650 nm and illumination intensity 10^{15} photons/$(\mathrm{cm}^2\mathrm{s})$. Red lines and values of U_{bi}, n_d^{th} and G^{ex} marked in red result from fitting the experimental data to Eq.4.39 assuming that $k_R = 10^9$ s^{-1}, $a = 10^{-7}$ cm and $\mu = 5 \cdot 10^{-6}$ cm$^2/(\mathrm{Vs})$.

practically in whole investigated voltage ranges. The value of the built-in voltage resulting from all fits ranges from 0.52 V to 0.57 V, therefore we may regard it as a constant. However, the value of free electron concentration at the rear contact derived during the fitting process is not constant, since it changes from about $1.6 \cdot 10^{15}$ cm^{-3} up to $5.7 \cdot 10^{15}$ cm^{-3} depending on illumination conditions. Moreover, values of n_d^{th} found for cells with ITO and CuI anodes should be identical, since rear contacts of these cells are identical. Therefore, change in the anode material should cause a change in the built in field leaving the n_d^{th} value unaffected. n_d^{th} dependence on illumination is inconsistent with the assumptions made in the derived CFA model. If this parameter is kept constant during the fitting process mobility becomes the parameter that increases upon illumination, since the slope of the j-V curve depends on these two constants. Illumination intensity dependence of n_d^{th} or μ implies the series resistance dependence on I_0. According to Vissenberg [114], mobility enhancement in organic materials is possible if con-

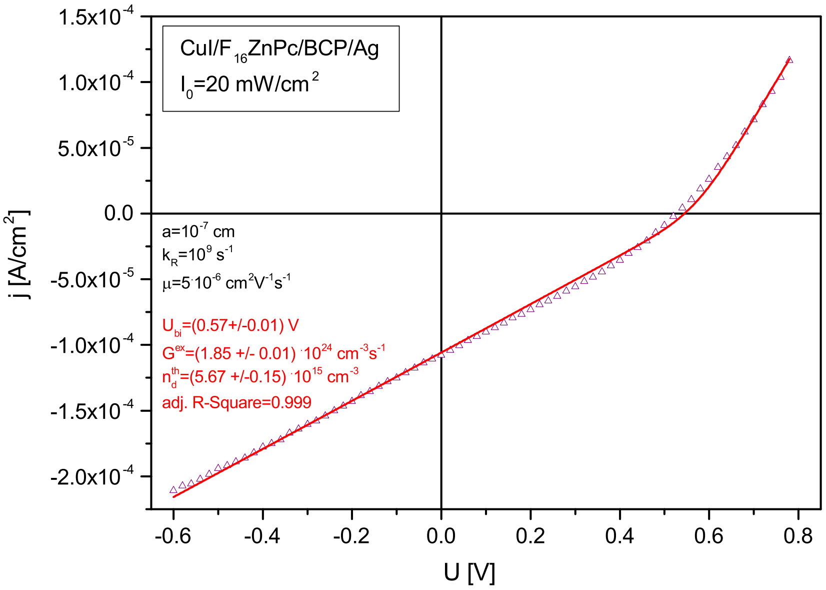

Figure 6.20: Current-voltage characteristics of the CuI/F$_{16}$ZnPc/BCP/Ag cell under white light illumination of intensity $I_0 = 20$ mW/cm^2. Red lines and values of U_{bi}, n_d^{th} and G^{ex} marked in red result from fitting the experimental data to Eq.4.39 assuming that $k_R = 10^9$ s^{-1}, $a = 10^{-7}$ cm and $\mu = 5 \cdot 10^{-6}$ cm^2/(Vs).

centration of free charge carriers is relatively high, i.e. when it approaches the density of states. However, the most probable reason for the observed photoconductivity of the regarded system is free charge carrier detrapping induced by illumination. This process was not regarded in the CFA model and that is why one of the parameters, namely n_d^{th} or μ change with illumination. It is worth noting, that photoconductivity that could be associated with light induced free charge carrier detrapping process was also reported for other systems comprising F$_{16}$ZnPc and other phthalocyanines [6, 115–117].

Photovoltaic parameters of the investigated CuI/F$_{16}$ZnPc/BCP/Ag cells extracted from the experimental data are given below

- λ=650 nm, I_0= 10^{15} photons/(cm^{2}s)
  j_{sc}=3.7 μA/cm^2, U_{oc}=0.39 V, FF=0.42, η=0.2 %,

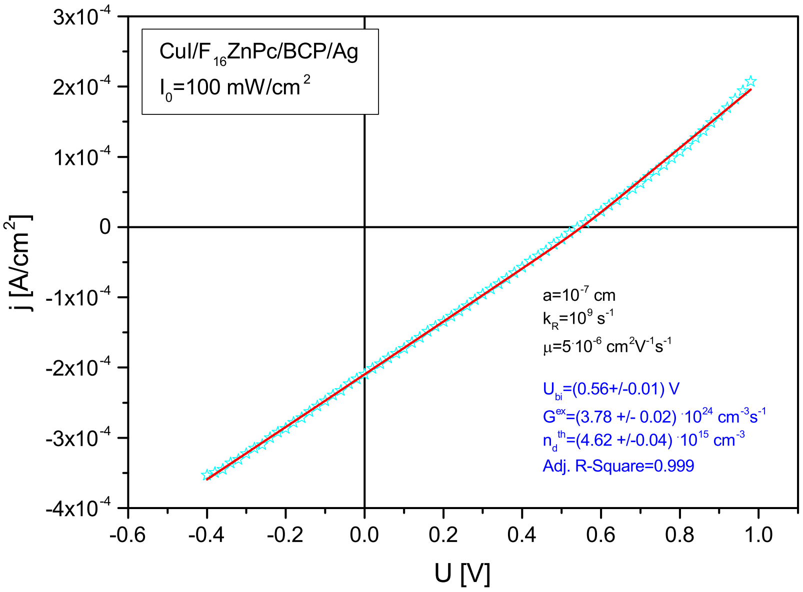

Figure 6.21: Current-voltage characteristics of the CuI/F$_{16}$ZnPc/BCP/Ag cell under white light illumination of intensity $I_0 = 100$ mW/cm^2. Red lines and values of U_{bi}, n_d^{th} and G^{ex} marked in red result from fitting the experimental data to Eq.4.39 assuming that $k_R = 10^9$ s^{-1}, $a = 10^{-7}$ cm and $\mu = 5 \cdot 10^{-6}$ cm$^2/(\mathrm{Vs})$.

- white light illumination of intensity I_0=20 mW/cm^2
  j_{sc}=0.11 mA/cm^2, U_{oc}=0.53 V, FF=0.29, η=0.084 %,

- white light illumination of intensity I_0=100 mW/cm^2
  j_{sc}=0.21 mA/cm^2, U_{oc}=0.55 V, FF=0.25, η=0.03 %,

Values of these parameters resulting from the fits are

- λ=650 nm, I_0= 10^{15} photons/(cm^{2}s)
  j_{sc}=3.14 $\mu\mathrm{A/cm}^2$, U_{oc}=0.42 V, FF=0.31
- white light illumination of intensity I_0=20 mW/cm^2
  j_{sc}=0.106 mA/cm^2, U_{oc}=0.545 V, FF=0.26
- white light illumination of intensity I_0=100 mW/cm^2
  j_{sc}=0.21 mA/cm^2, U_{oc}=0.55 V, FF=0.25.

Noticeable discrepancy between the experimental values and the ones resulting from the fits was obtained only under monochromatic illumination. Electron collection efficiencies at short-circuit φ_C calculated from the CFA model under investigated illumination conditions knowing G^{ex} are 0.32 %, 0.35 % and 0.34 %, respectively and these results are consistent with the value of φ_C equal to 0.3 % estimated on the basis of drift and surface recombination velocities. Such value of φ_C implies, that the surface recombination velocity is about two orders of magnitude greater than the drift velocity. Moreover, this free electron collection efficiency is three times greater than the one calculated for the ITO/F_{16}ZnPc/BCP/Ag cells. Such improvement in free charge carrier collection efficiency follows from the rise in the built-in field and decrease in the phthalocyanine thickness, but it is still insufficient to enable good photovoltaic performance of the investigated system.
One must bare in mind, that according to the CFA model high value of φ_C, i.e. high value of drift velocity (resulting from high free charge carrier mobility, high built-in voltage and small layer thickness) as and low value of surface recombination velocity (originating from low recombination constant), is not the only prerequisite for obtaining good photovoltaic performance. Efficient photoexcitation followed by effective exciton dissociation, that determine the photogeneration rate, are the processes of fundamental importance. It is evident, that under white light illumination of investigated cells photogeneration rate is a sublinear function of light intensity, since a fivefold increase in I_0 brings about only a twofold rise in G^{ex}. According to the CFA model, $j_{sc} \sim G^{ex}$ and this accounts for the observed twofold increase in the short-circuit current density. Therefore, although the increase in the illumination intensity causes the increase in j_{sc} and U_{oc}, fill factor decreases and so does the efficiency of the cell. It is also worth noting, that under white light illumination of 20 mW/cm^2 the open-circuit voltage is practically saturated and approaches the value of the built-in voltage. Saturation of this parameter may be attributed to sublinearity of light intensity dependence of the photogeneration rate.

Lets now analyze the current-voltage behavior of the investigated CuI/F_{16}ZnPc/BCP/Ag cells in terms of the SEC model. Just as in case of cells with ITO anode, two characteristic regimes of the dark current - voltage curve (Fig. 6.22) can be distinguished: 1) a limited range from -0.05 V to 0.35 V where a good fit to

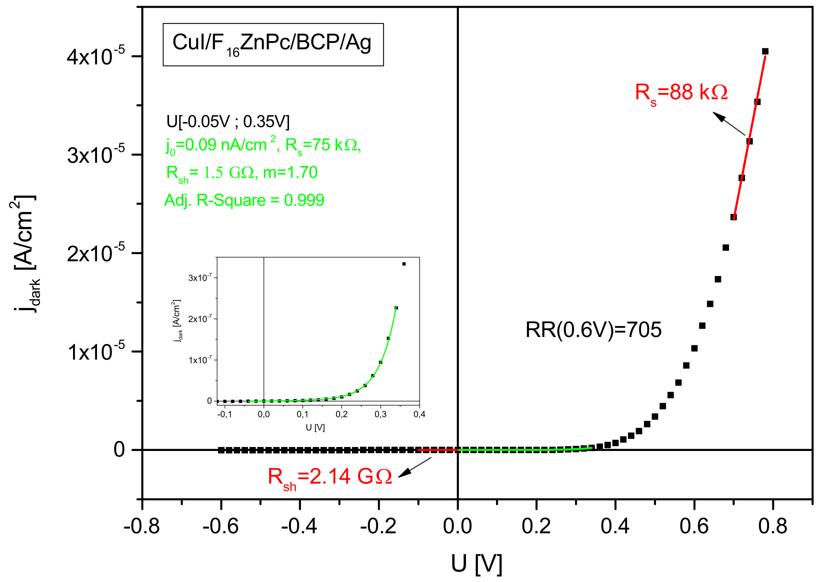

Figure 6.22: Current-volatge characteristics measured in the dark (squares) for CuI/F_{16}ZnPc/BCP/Ag cells. Green line and parameters j_0, m, R_s, R_{sh} and Adj. R-Square show the results of the fit of experimental values to the SEC model in the voltage range from -0.05 V to 0.35 V. RR is the rectification ratio calculated at ±0.6 V. Arrows point out series and shunt resistances estimated from the slopes of the linear parts of the curve.

the SEC model was found and 2) a short linear part of the curve under forward bias $\geqslant$ 0.7 V from which approximated value of the series resistance of 88 kΩ was calculated. The value of shunt resistance equal to 2.14 GΩ was estimated from the slope of the curve under reverse bias. Saturation current density equal to 0.068 nA/cm^2 and diode ideality factor of 1.65 were predetermined from the ln$x$ vs $(U - IR_s)$ plot, according to the method described in the previous section. These values, along with estimated values of series and shunt resistances, were used as initial values in the fitting process. The highest value of Adj. R-Square was obtained for the following parameters

- m=1.7, j_0=0.09 nA/cm^2, R_{sh}=1.5 GΩ and R_s=75 kΩ.

Low value of the saturation current density and high value of the shunt resistance account for good diode behavior of the investigated device. Series resistance of

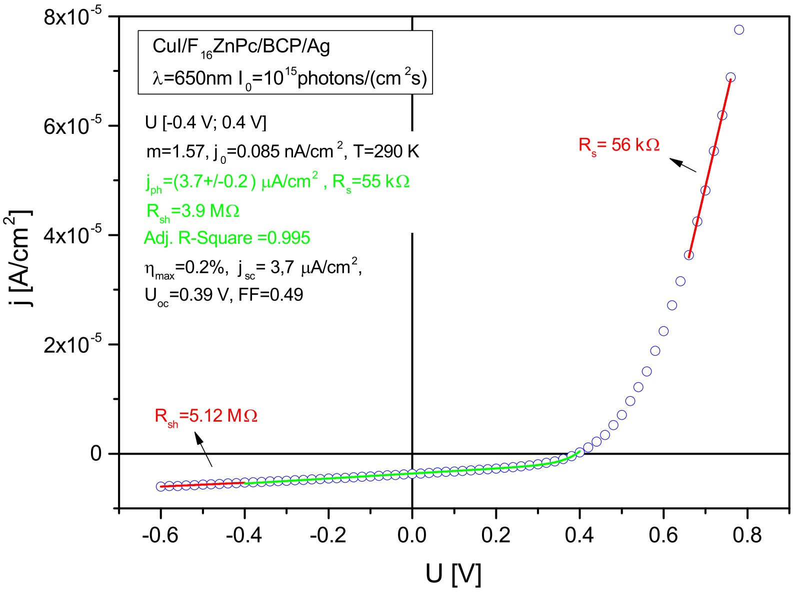

Figure 6.23: Current-volatge characteristics measured under monochromatic illumination of λ=650nm and intensity 10^{15} photons/(cm^{2}s) (circles) for CuI/F$_{16}$ZnPc/BCP/Ag cells; Green line and parameters j_0, m, j_{ph}, R_s, R_{sh} and Adj. R-Square show the results of the fit of experimental values to the SEC model in the voltage range from -0.4 V to 0.4 V. Arrows point out series and shunt resistances estimated from the slopes of the linear parts of the curve. Illumination from the front side.

this cell is comparable to the one found for the ITO/F$_{16}$ZnPc/BCP/Ag cell, therefore it can be interpreted as the bulk resistance of the device. Small dissimilarity between these resistances can be attributed to the difference in the thickness of the phthalocyanine layers. Diode ideality factor of 1.7 confirms the presence of trap-assisted monomolecular recombination of free charge carriers.

Two characteristic parts of the current-voltage curve, i.e. one corresponding to the SEC model for voltages up to the value of the open-circuit voltage and the other part corresponding to a linear dependence of the photocurrent on the applied voltage under higher forward bias, were also found under all investigated illumination conditions (see Figs. 6.23, 6.24 and 6.25). Values of shunt and series resistances were estimated from the curves and used to calculate x. In the

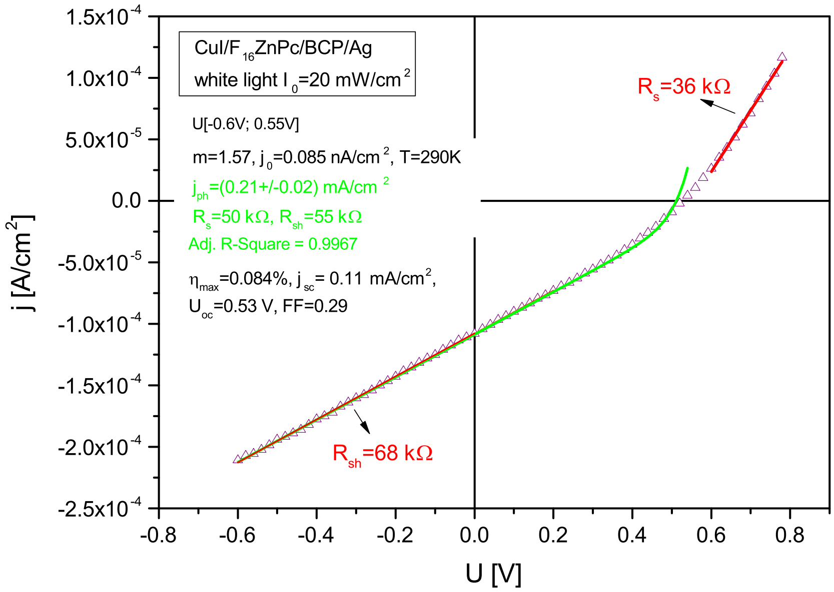

Figure 6.24: Current-volatge characteristics measured under white light illumination of 20 mW/cm^2 (triangles) for CuI/F$_{16}$ZnPc/BCP/Ag cells. Green line and parameters j_0, m, j_{ph}, R_s, R_{sh} and Adj. R-Square show the results of the fit of experimental values to the SEC model in the voltage range from -0.4 V to 0.4 V. Arrows point out series and shunt resistances estimated from the slopes of the linear parts of the curve. Illumination from the front side.

case of monochromatic illumination ln$x$ vs $(U - JR_s)$ plot was made, but unreliable results were obtained, while under white light illumination this method of parameter estimation failed. Nevertheless, good fits to the SEC model in a limited ranges of voltage were obtained in all these cases for the same value of the saturation current density j_0 equal to 85 pA/cm^2 and the diode ideality factor m=1.57. These values stand in a perfect agreement with the values of saturation current density and the diode ideality factor extracted from the dark current-voltage plot and the open-circuit voltage action spectra, respectively. Values of the parameters derived from the SEC model upon illumination of the investigated structure were as follows:

- λ=650 nm, I_0= 10^{15} photons/(cm^{2}s)
  j_{ph} = (3.7 ± 0.2) $\mu\mathrm{A/cm}^2$, R_{sh}=3.9 MΩ and R_s=55 kΩ

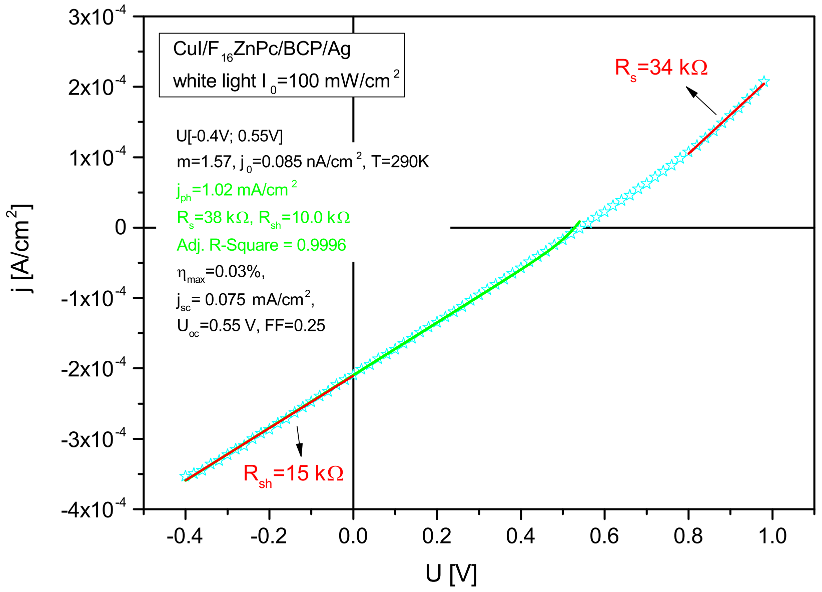

Figure 6.25: Current-volatge characteristics measured under white light illumination of 100 mW/cm^2 (stars) for CuI/F$_{16}$ZnPc/BCP/Ag cells. Green line and parameters j_0, m, j_{ph}, R_s, R_{sh} and Adj. R-Square show the results of the fit of experimental values to the SEC model in the voltage range from -0.4 V to 0.55 V. Arrows point out series and shunt resistances estimated from the slopes of the linear parts of the curve. Illumination from the front side.

- white light illumination of intensity I_0=20 mW/cm^2
  j_{ph}=(0.21 $\pm$ 0.02) mA/cm^2, R_{sh}=68 kΩ and R_s=36 kΩ
- white light illumination of intensity I_0=100 mW/cm^2
  j_{ph}=1.02 mA/cm^2, R_{sh}=10 kΩ and R_s=38 kΩ

The increase in illumination intensity brings about a significant decrease in the shunt resistance, as well as a less pronounced drop in the value of series resistance, that remains of the same order of magnitude. Decrease in the series resistance of the cell may be attributed to the light induced detrapping of free charge carriers. Furthermore, under monochromatic illumination short-circuit current density is identical as the obtained value of j_{ph}, while under white light illumination j_{sc} corresponds to only 52% and 20.5% of calculated j_{ph} upon illumination intensity of 20 mW/cm^2 and 100 mW/cm^2 respectively. Yet, the ratio of photogen-

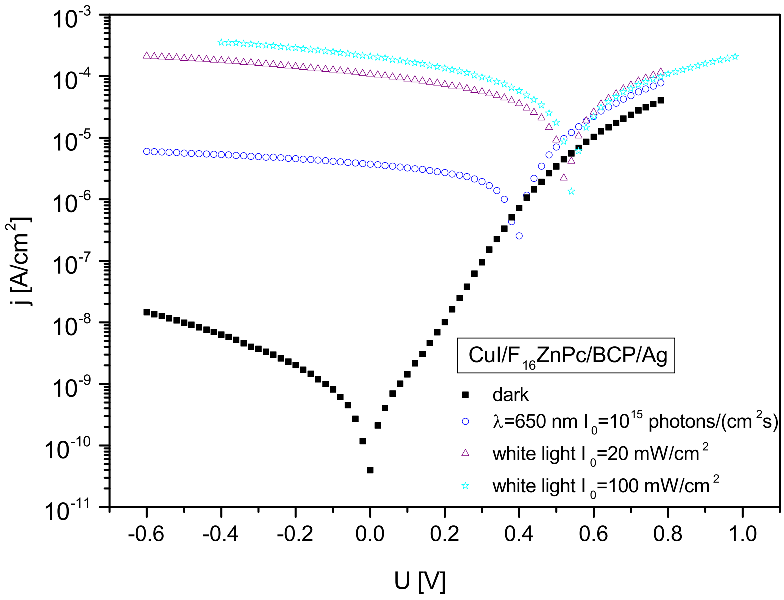

Figure 6.26: Current-volatge characteristics measured in the dark (squares), under monochromatic illumination of λ=650nm and intensity 10^{15} photons/(cm^{2}s) (circles), white light illumination of 20 mW/cm^2 (triangles) and white light illumination of 100 mW/cm^2 (stars) for CuI/F$_{16}$ZnPc/BCP/Ag cells. Illumination from the front side.

erated current densities derived from the SEC model under 100 mW/cm^2 and 20 mW/cm^2 illumination intensity is practically the same as the ratio of these light intensities, which suggests that under the investigated white light illumination intensity the photogenerated current is still a linear function of light intensity and monomolecular recombination of free charge carriers at the active junction is still a dominant quenching process at this junction. The disproportion between the calculated j_{ph} and measured j_{sc} values may follow from the major decrease in shunt resistance that causes a rapid drop in the $R_{sh}/(R_{sh}+R_s)$ ratio, since according to the resistances calculated from the fits to the SEC model, this ratio is equal to about 1, 0.65 and 0.21 under 10^{15} photons/(cm^{2}s), 20 mW/cm^2 and 100 mW/cm^2 respectively, and these values stand in a good agreement with obtained j_{sc}/j_{ph} ratios. Moreover, analysis of the SEC model based on $R_{sh}/(R_{sh}+R_s)$ ratios and values of the photogenerated currents shows that under reverse bias, for which the photogenerated current dominates the current flow, currents flowing through the investigated cell should be higher under light intensity of 100 mW/cm^2 than under 20 mW/cm^2, while under high forward bias, for which the dark injected current is much greater than the photogenerated one, current density measured under lower light intensity should be greater. Comparison of all collected current-voltage plots shown in Fig. 6.26 confirms the reasoning given above. Due to changes in the shunt resistance of the cell induced by light, current-voltage curves do not overlap each other even under high forward bias. Such a great reduction in the shunt resistance observed under illumination is consistent with the derived CFA model, since R_{sh}/R_s ratios calculated in the dark and under illumination of the cell with the CuI anode calculated on the basis of both regarded models are

- in the dark
  $\frac{R_{sh}^{dark}}{R_s} \approx 2 \cdot 10^9$ (CFA model) and $\frac{R_{sh}^{dark}}{R_s} \approx 2 \cdot 10^6$ (SEC model),
- under monochromatic illumination of 10^{15} photons/(cm^{2}s)
  $\frac{R_{sh}^{ill}}{R_s} \approx 46$ (CFA model) or $\frac{R_{sh}^{ill}}{R_s} \approx 70$ (SEC model),
- white light illumination of intensity I_0=20 mW/cm^2
  $\frac{R_{sh}^{ill}}{R_s} \approx 2.1$ (CFA model) or $\frac{R_{sh}^{ill}}{R_s} \approx 1.9$ (SEC model).
- white light illumination of intensity I_0=100 mW/cm^2
  $\frac{R_{sh}^{ill}}{R_s} \approx 0.22$ (CFA model) or $\frac{R_{sh}^{ill}}{R_s} \approx 0.26$ (SEC model).

Values of G^{ex}/G^{th} and $(j_{ph}/j_0)^m$ calculated for these two models are also consistent with each other, since their values are

- under monochromatic illumination of 10^{15} photons/(cm^{2}s)
  $G^{ex}/G^{th} \approx 3 \cdot 10^9$ (CFA model) or $(j_{ph}/j_0)^m \approx 11 \cdot 10^9$ (SEC model),
- white light illumination of intensity I_0=20 mW/cm^2
  $G^{ex}/G^{th} \approx 2.3 \cdot 10^7$ (CFA model) or $(j_{ph}/j_0)^m \approx 1.9 \cdot 10^7$ (SEC model),
- white light illumination of intensity I_0=100 mW/cm^2
  $G^{ex}/G^{th} \approx 4 \cdot 10^{10}$ (CFA model) or $(j_{ph}/j_0)^m \approx 13 \cdot 10^{10}$ (SEC model).

It is worth mentioning, that the current-voltage relation for the intensity of light of 100 mW/cm^2 was collected three weeks after the other current-voltage curves, while the calculated values of j_{ph} suggest no degradation of the cell.

6.3 Conclusions

- Both investigated systems, namely ITO/F_{16}ZnPc/BCP/Ag and CuI/F_{16}ZnPc/BCP/Ag, shown photovoltaic action resulting from exciton dissociation at the front illuminated electrode/organic material interfaces.
- Additional mechanism of free charge carrier generation in the CuI/F_{16}ZnPc/BCP/Ag cell, following from band to band transition in the bulk of the CuI layer, was not observed. Therefore, CuI plays solely the role of the electrode in the regarded system.
- Reliable value of the exciton diffusion length in the perfluorozincphthalocyanine layer of 18 ± 7 nm was determined from the short-circuit current action spectra measured for the ITO/F_{16}ZnPc/BCP/Ag cell.
- Both regarded models, i.e. CFA and SEC models, were used to describe the current-voltage behavior of the investigated single layer cells and it is impossible to determine which model is more suitable basing on the values of the adjusted R-square. However, the Shockley equivalent circuit model could be used in a limited range of voltages, while good fits to experimental data practically in the whole investigated voltage range were obtained when the derived CFA model was applied, though illumination dependence of one of the constants had to be assumed.
- Comparison of both regarded models leads to a conclusion that, as long as exciton dissociation at one of the electrode/organic material interfaces is the only process affected by illumination, series resistance of the single layer cell is constant, while shunt resistance of the cell is strongly reduced upon illumination. High free charge carrier mobility and high built-in field are prerequisites for good quality diodes of low series resistance and high shunt resistance.
- The ratio of photo and thermal generation rates characteristic for the derived CFA model is analogous to the ratio of photogeneration and saturation currents raised to power m equal to the diode ideality factor dependent on the dominant free charge carriers recombination mechanism.

- Under identical illumination conditions photogeneration rates found for both investigated systems are comparable, therefore better photovoltaic performance of the CuI/F_{16}ZnPc/BCP/Ag system may be associated with:
    - greater built-in field of this system and lower phthalocyanine layer thickness that bring about an increase in the value of U_{oc} and drift velocity v_d, and as a result enhancement of φ_C and current density (in terms of the derived CFA model),
    - lower series resistance, greater shunt resistance and lower dark saturation current density of this system (in terms of the SEC model).

- Current-voltage curves collected in the dark and under illumination do not overlap each other, suggesting light intensity dependence of concentration of free charge carriers at the rear contact, implying light intensity dependence of series resistance. Decrease in the series resistance of both investigated systems brought by illumination may be attributed to photoconductivity of the cells resulting from light induced detrapping or generation of free charge carriers in the bulk of the phthalocyanine layer, though the latter phenomenon is far less probable.

- Monomolecular trap-assisted recombination is the dominant quenching process in regarded systems under relatively low light intensities. Under higher illumination intensity the influence of bimolecular recombination is noticeable.

- Due to the fact that CuI/F_{16}ZnPc/BCP/Ag cells show relatively high j_{sc}, U_{oc}, FF and η values in the ambient air, without encapsulation and optimization, and because they are able to utilize light from quite a broad range of wavelengths, it seems that F_{16}ZnPc may be a good material for photovoltaic applications.

Chapter 7

Photovoltaic phenomenon in bilayer cells based on the donor/F_{16}ZnPc heterojunction

This chapter presents results of research concerning the photovoltaic effect taking place in bilayer polymer/F_{16}ZnPc and small molecule/F_{16}ZnPc cells with MEH-PPV and DIP donor layers respectively.

7.1 Bilayer cells based on the MEH-PPV/F_{16}ZnPc heterojunction

This section is devoted to verification of the processes leading to free charge carrier generation and determination of any loss mechanism affecting the course of photovoltaic phenomenon in the cells based on the planar MEH-PPV/F_{16}ZnPc heterojunction. Special attention is paid to the role of buffer layers in the investigated system. In order to verify the influence of bathocuproine (BCP) and molybdenum trioxide MoO_3 on the performance of cells based on the investigated junction ITO/MEH-PPV/F_{16}ZnPc/Ag, ITO/MEH-PPV/F_{16}ZnPc/BCP/Ag, ITO/MoO_3/MEH-PPV/F_{16}ZnPc/Ag and ITO/MoO_3/MEH-PPV/F_{16}ZnPc/BCP/Ag cells were fabricated. Energy band diagram of materials forming these systems is shown in Fig. 7.1

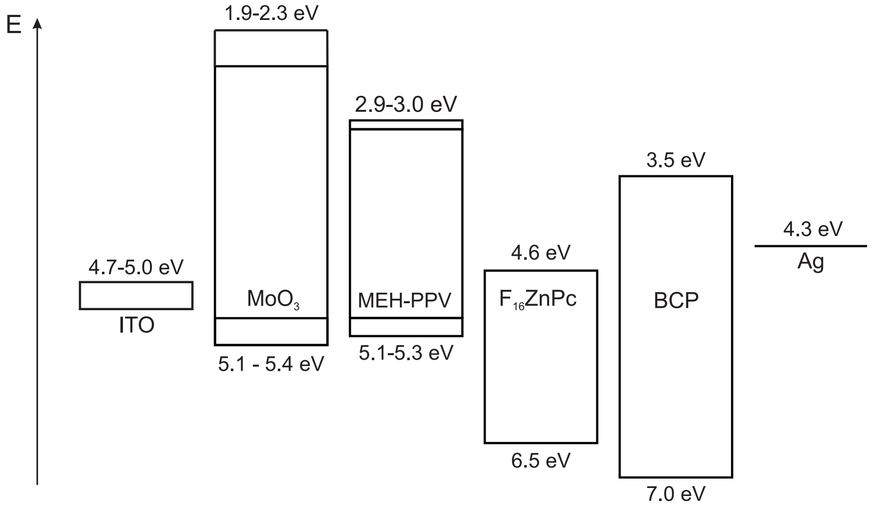

Figure 7.1: Energy level diagram of investigated materials [105].

7.1.1 Short-circuit current and open-circuit voltage action spectra

MEH-PPV was chosen as a donor material due to its absorption spectrum and sufficient offset between its HOMO/LUMO positions and HOMO/LUMO positions of the investigated phthalocyanine, that should enable efficient exciton dissociation at the junction of these materials. Short-circuit current and open-circuit voltage action spectra presented in Fig. 7.2 were collected in order to verify this assumption. These spectra show the wavelength dependence of j_{sc} and U_{oc} for the cell without buffer layers, illuminated through the ITO electrode at a constant light intensity of 10^{15} photons/(cm^{2}s). Absorption spectra of donor and acceptor layers of thickness equal to about 100 nm are also included in the graphs. Both obtained action spectra are symbatic in the region of F_{16}ZnPc absorption, while in the spectral range of intensive absorption of MEH-PPV, in which absorption of F_{16}ZnPc is negligible, j_{sc} and U_{oc} spectra are not clearly antibatic, but the peak values of short-circuit current density and open-circuit voltage are certainly blueshifted toward the region of lower polymer absorption. Such a spectral response proves that generation of free charge carriers occurs via exciton photogeneration in polymer and/or phthalocyanine layer and subsequent dissociation of excited states at the MEH-PPV/F_{16}ZnPc interface, which makes this interface an active junction in the considered system. Direction of the current flow shows, that during the ex-

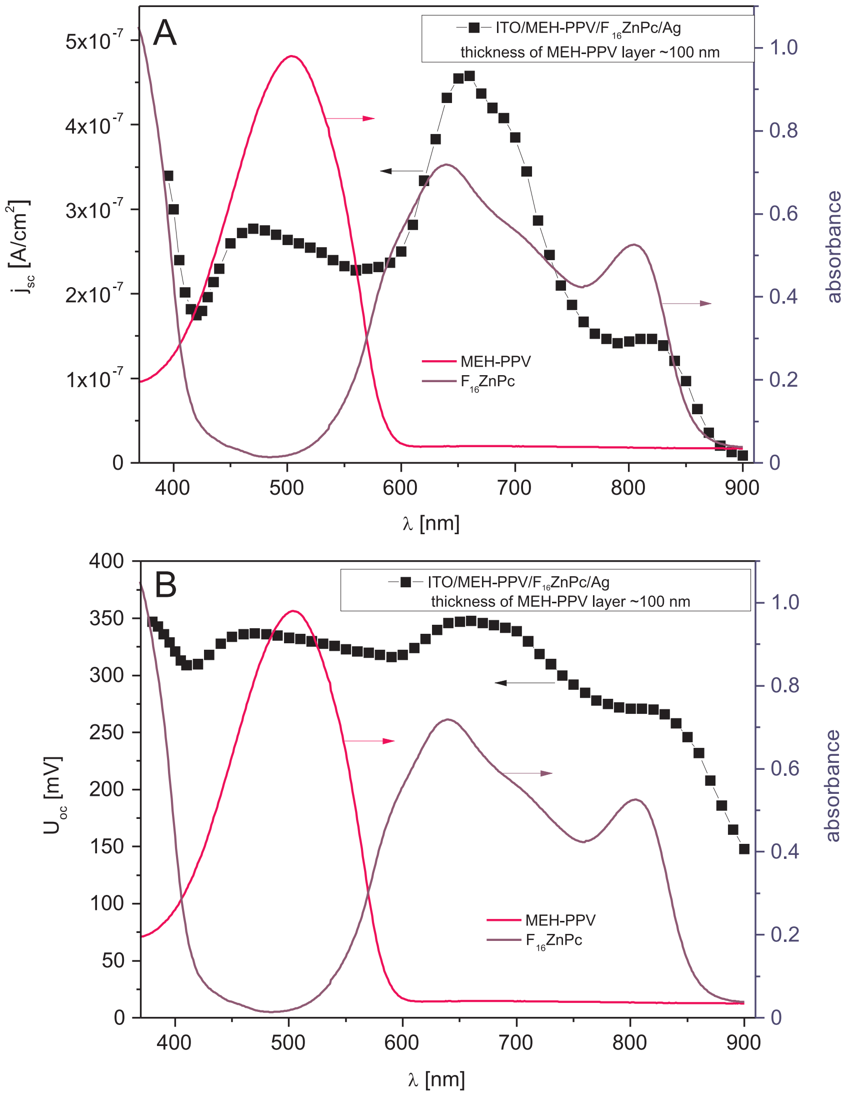

Figure 7.2: Spectral response of short-circuit current (A) and open-circuit voltage (B) of the ITO/MEH-PPV/F$_{16}$ZnPc/Ag cell illuminated through the ITO electrode with light of intensity $I_0 = 10^{15}$ photons/(cm^{2}s) (black squares), MEH-PPV absorption spectrum (pink line) and F$_{16}$ZnPc absorption spectrum (purple line). Thickness of the MEH-PPV layer $\sim$ 100 nm.

citon dissociation process at the D/A junction holes are injected to the polymer layer, whereas electrons are injected to the phthalocyanine layer. According to the action spectra recorded for cells having MEH-PPV layers of different thickness (Figs. 7.2-7.5), only excitons created in the vicinity of the active junction are able to dissociate into free charge carriers at the regarded D/A interface and to

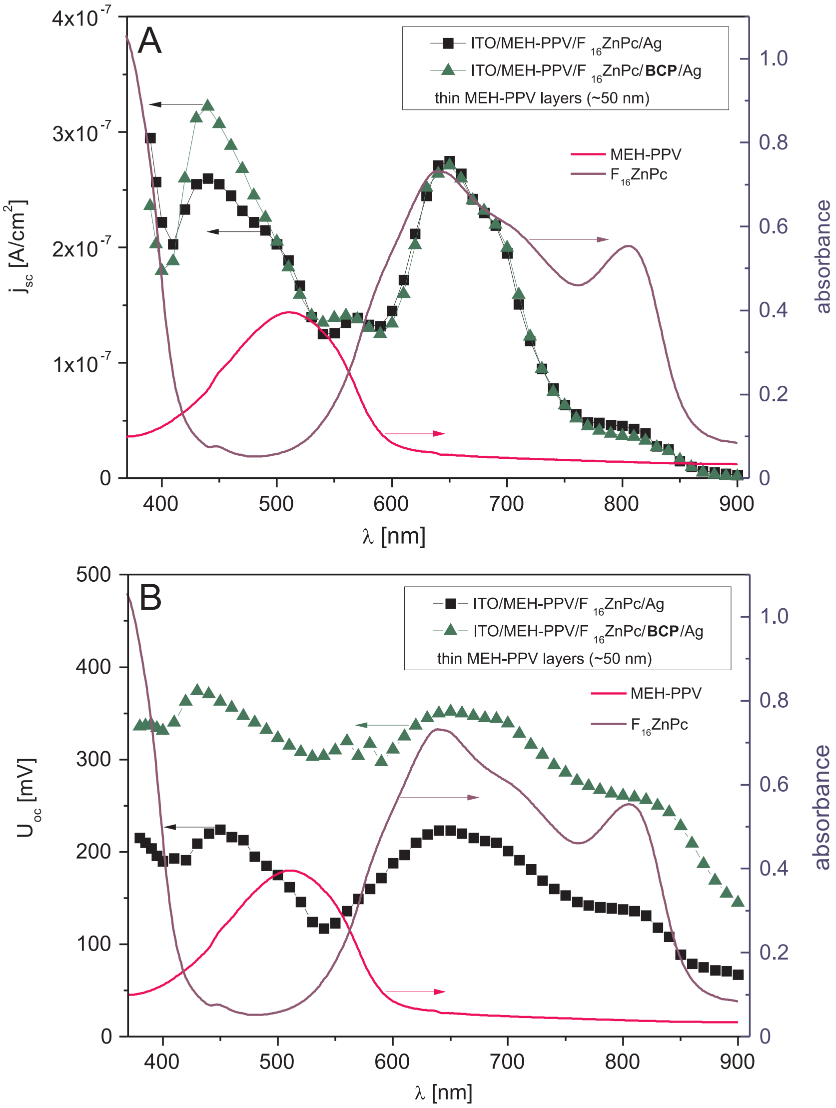

Figure 7.3: Spectral response of short-circuit current (A) and open-circuit voltage (B) of the ITO/MEH-PPV/F_{16}ZnPc/Ag cell (squares) and ITO/MEH-PPV/F_{16}ZnPc/BCP/Ag cell (triangles), MEH-PPV absorption spectrum (pink line) and F_{16}ZnPc absorption spectrum (purple line). Thickness of the MEH-PPV layer $\sim$ 50 nm, samples fabricated in the same cycle. $I_0 = 10^{15}$ photons/(cm^{2}s), illumination from the ITO side.

give their contribution to electric current flow or to the open-circuit voltage, since action spectra obtained for all investigated cells illuminated through ITO electrode are symbatic in the region of phthalocyanine absorption, but the thicker the MEH-PPV layer is the more antibatic j_{sc} and U_{oc} spectra are in the region of polymer

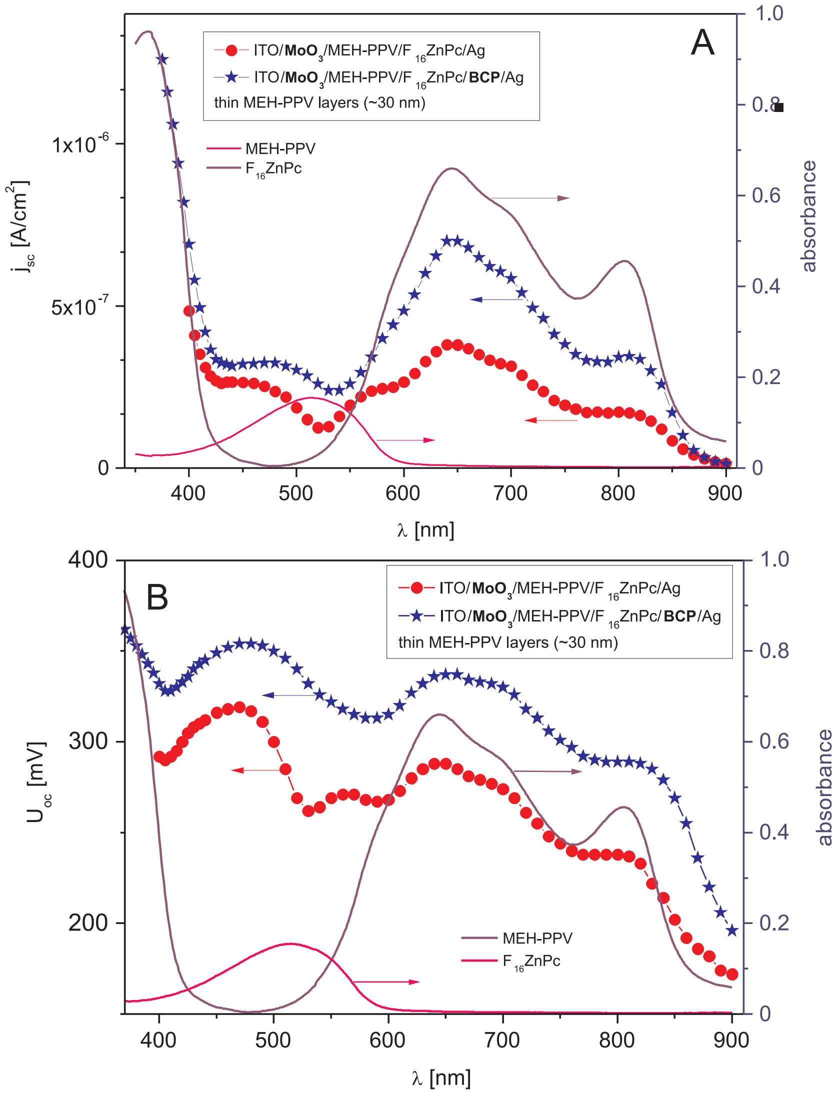

Figure 7.4: Spectral response of short-circuit current (A) and open-circuit voltage (B) of the ITO/MoO_3/MEH-PPV/F_{16}ZnPc/Ag cell (circles) and ITO/MoO_3/MEH-PPV/F_{16}ZnPc/BCP/Ag cell (stars) [105], MEH-PPV absorption spectrum (pink line) and F_{16}ZnPc absorption spectrum (purple line). Thickness of the MEH-PPV layer ~ 30 nm, samples fabricated in the same cycle. $I_0 = 10^{15}$ photons/(cm^2s), illumination from the ITO side.

absorption. It is not surprising that the thicker the polymer layer is the lower is the value of the short-circuit current density, especially in the region of strong absorption of this material. This may be a result of a short exciton diffusion length in the MEH-PPV layer and bulk resistance of this layer. The former reason can also ac-

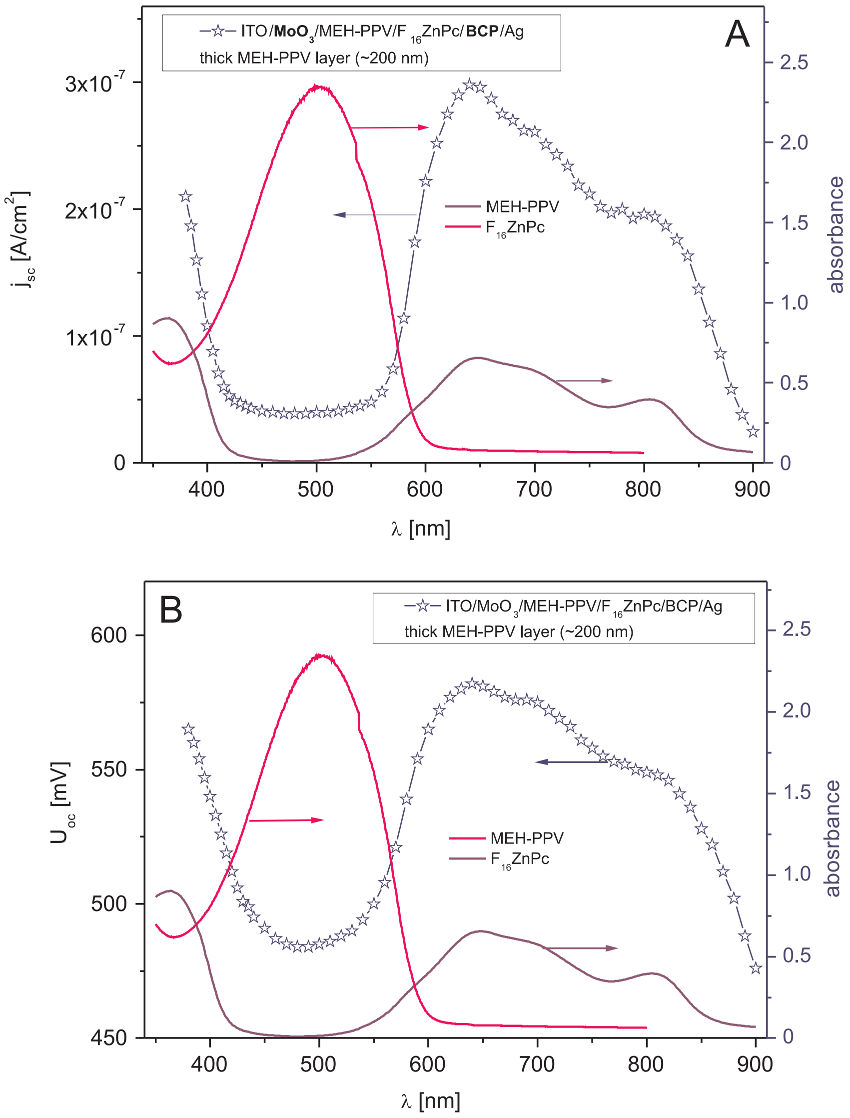

Figure 7.5: Spectral response of A) short-circuit current and B) open-circuit voltage of the ITO/MoO_3/MEH-PPV/F_{16}ZnPc/BCP/Ag cell with a thick $\sim$ 200 nm MEH-PPV layer (open stars), MEH-PPV absorption spectrum (pink line) and F_{16}ZnPc absorption spectrum (purple line). $I_0 = 10^{15}$ photons/(cm^2s), illumination from the ITO side.

count for the fact, that if the thickness of MEH-PPV is $\geqslant$ 30 nm, which is the case of all investigated cells, photocurrent density is hardly ever higher in the spectral range of MEH-PPV absorption than in the spectral range of intensive absorption of F_{16}ZnPc, while regardless of buffer layers, devices with thick MEH-PPV layers show higher maximum values of the open-circuit voltage in the acceptor absorption range, whereas those having thin MEH-PPV layers in the spectral range of donor absorption. It is also noticeable, that the thicker the polymer is the higher is the value of U_{oc} in the whole investigated spectral range, which is characteristic for all fabricated photovoltaic cells. This can result from the fact, that the surface of the MEH-PPV layer (check supplementary material) is rather uneven, therefore this layer may not be homogeneous, which in case of thin layers increases the risk of shorting and lowers the open-circuit voltage value.

There is no doubt that introduction of buffer layers has a significant impact on j_{sc} and U_{oc} action spectra. It seems that introduction of any interlayers should lead to an increase in the series resistance of a cell. Thus, at least a small drop in the short-circuit current value in the whole spectral range should be expected [118], but Figs. 7.3 and 7.4 show something different. Even though additional BCP layer was incorporated to investigated cells, values of short-circuit current density have increased in case of cells with both buffer layers. Such a result suggests a rise in charge carrier photogeneration efficiency and/or a drop in the bulk recombination rate of charge carriers and decrease in series resistance. All these effects could be related to better quality of the organic active layer having lower number of defect states. This quality improvement can originate from presence of the BCP interlayer during thermal evaporation of a silver electrode, since as it was already mentioned, during this process silver atoms may diffuse into bare organic layers causing severe damage to the active layer. Moreover, reduction of potential barrier heights for charge carrier injection at anode/organic material and organic material/cathode interfaces caused by incorporation of buffer layers is also possible, as it can account for the increase of j_{sc} as well. Furthermore, introduction of any additional layers to the investigated system for sure changes the optical field distribution in this system, due to optical effects such as reflection of light at interfaces and interference of light within the bulk of a sample. Thus, differences in the shape of action spectra resulting from incorporation of MoO_3 and BCP buffer layers can be explained this way. It is worth noting, that it is rather unlikely that excitons reflected from the BCP buffer layer, which is regarded as an exciton blocking layer (EBL), reach the active donor/acceptor interface and contribute to current generation. They rather recombine before getting to that junction due to a relatively high thickness of the phthalocyanine layer ($\sim$ 100 nm) and a relatively low value of the exciton diffusion length $(L \sim$ 18 nm$)$ in this material.

7.1.2 Light intensity dependence of short-circuit current and open-circuit voltage

Figure 7.6 shows short-circuit current density as a function of incident light intensity for diodes with thin, i.e. $\leqslant$ 50 nm, MEH-PPV layers. All cells were illuminated through the ITO electrode with monochromatic light of wavelength 650 nm, for which short-circuit currents reach peak values. For all investigated structures the same relation between j_{sc} and I_0 as in case of single layer cells was found, i.e. $j_{sc} \sim {I_0}^b$. At low light intensities, not exceeding $2 \cdot 10^{14}$ photons/(cm^{2}s), 0.92$\leqslant$ b $\leqslant$0.96 disregarding the presence of buffer layers. It means that at low illumination intensity excitons are created in the process of single-photon absorption and photocurrent is limited by monomolecular recombination of free charge carriers resulting from the presence of trapping sites. However, as the light intensity increases influence of buffer layers becomes evident. In the absence of the BCP b drops to about 0.8, that suggests the presence of bimolecular recombination. It is also possible, that at higher illumination intensities photocurrent is affected by space charge created as a result of low conductivity of organic layers and poor collection of free charge carriers at respective electrodes [119]. Better j_{sc} response to light intensity was obtained for cells with the BCP interlayer. At higher illumination intensities b drops to 0.9 and 0.86 for cells with the BCP and both buffer layers, respectively, which means that bimolecular recombination is less pronounced in these cases. This could follow from more effective collection of charge carriers at electrodes. Moreover, though the presence of the BCP layer influences the value of b, which means it affects the type of recombination, it does not shift the $j_{sc}(I_0)$ curve upwards (see Fig. 7.6A). This upward shift is present only when both buffer layers are used (Fig. 7.6B), which was also seen on the short-circuit current action spectra (Figs. 7.3A and 7.4A) and indicates a positive role of the anodic MoO$_3$ layer on j_{sc} but only in the presence of the BCP layer. Improvement caused by incorporation of the anodic buffer layer may not be observed in the absence of BCP due to damage caused by evaporation of silver electrode. It is worth noting, that the presence of buffer layers is not the only fac-

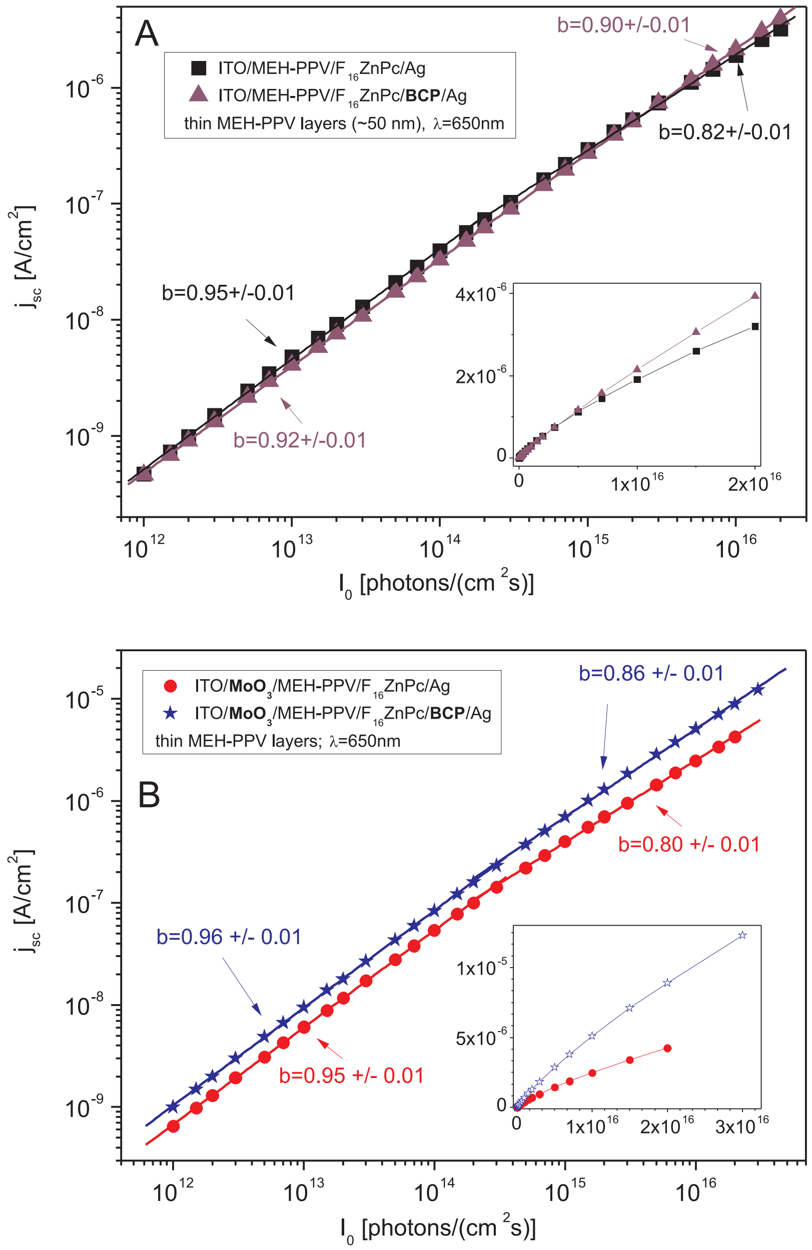

Figure 7.6: Short-circuit current density as a function of incident light intensity for ITO/MEH-PPV/F_{16}ZnPc/Ag (squares) and ITO/MEH-PPV/F_{16}ZnPc/BCP/Ag cell (traingles) fabricated in the same cycle (A), ITO/MoO_3/MEH-PPV/F_{16}ZnPc/Ag cell (circles) and ITO/MoO_3/MEH-PPV/F_{16}ZnPc/BCP/Ag cell (stars) fabricated in the same cycle (B) [105]. λ=650 nm, illumination from the ITO side, thin polymer layers.

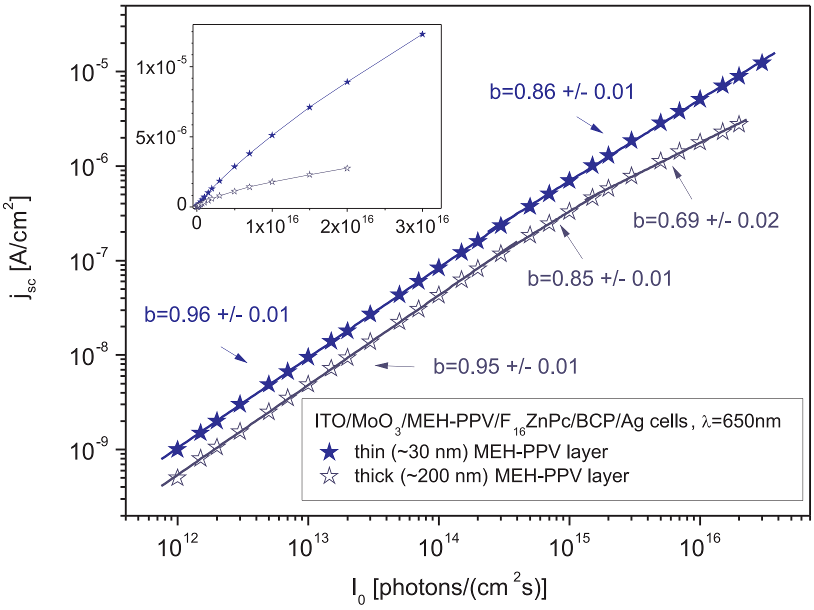

Figure 7.7: Short-circuit current density as a function of incident light intensity for ITO/MoO_3/MEH-PPV/F_{16}ZnPc/BCP/Ag cells with a thin (stars) and thick (open stars) polymer layer. λ=650 nm, illumination from the ITO side.

tor affecting recombination of free charge carriers. Fig. 7.7 shows the influence of polymer thickness on light intensity dependence of j_{sc} for cells with both buffer layers. It confirms our previous conclusions, that due to short exciton diffusion length, the thicker MEH-PPV layer is the lower is the number of excitons reaching the active interface and the lower is the photogeneration yield. Increase in series resistance, originating from increase in the thickness of polymer layer and poor conductivity, hampers charge collection enhancing free charge carrier recombination. Therefore, a rapid drop in b to 0.69 at higher light intensity, i.e. at $I_0 > 10^{15}$ photons/(cm^{2}s), is observed for cells with MEH-PPV layer thickness exceeding 100 nm.

The effect of buffer layers, polymer thickness and wavelength of incident light on open-circuit voltage under different illumination intensities is presented in Figs. 7.8, 7.9 and 7.10. The presence of the anodic buffer layer seems not to affect the U_{oc} of MEH-PPV/ F_{16}ZnPc cells, but undoubtedly, introduction of the BCP buffer layer causes two positive effects. The first one is a clear upward shift of the U_{oc} in the whole investigated I_0 range. This effect can be explained in a few different

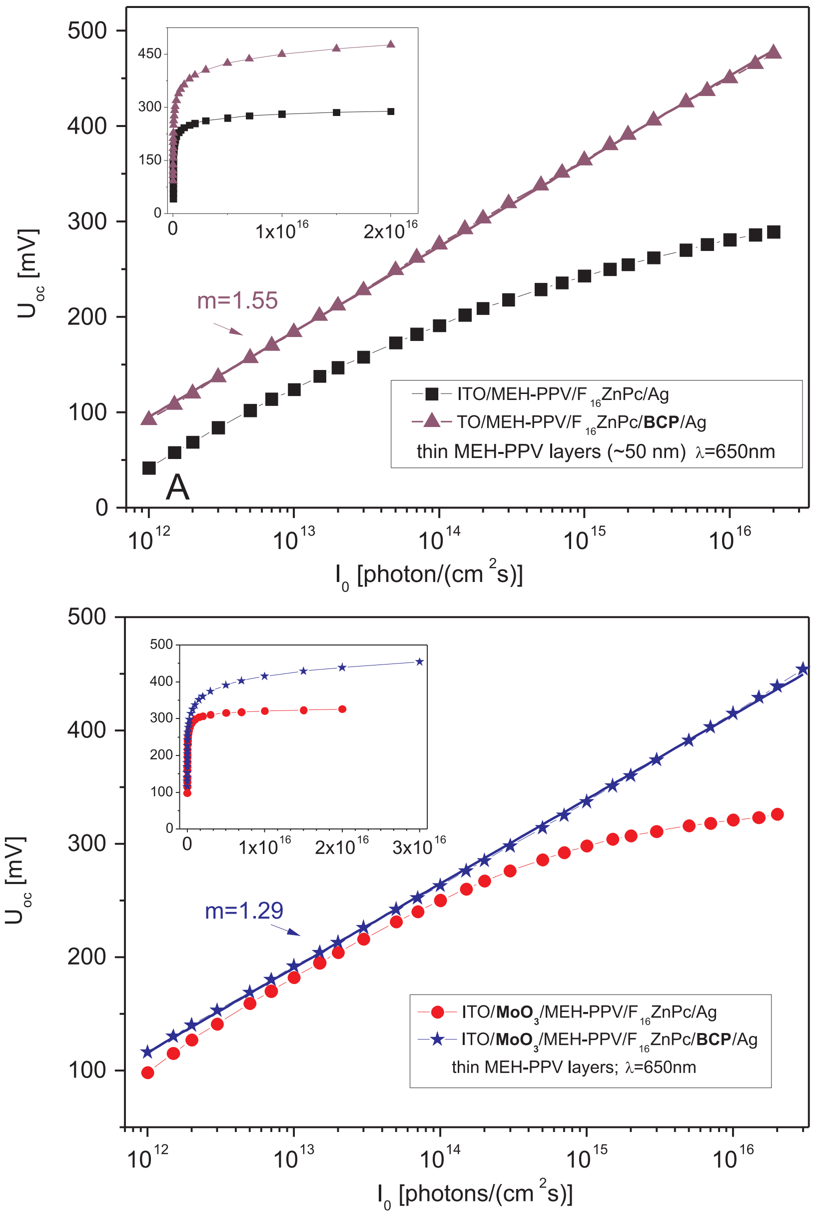

Figure 7.8: Open-circuit voltage as a function of incident light intensity for ITO/MEH-PPV/F_{16}ZnPc/Ag cell (squares) and ITO/MEH-PPV/F_{16}ZnPc/BCP/Ag cell (traingles) fabricated in the same cycle (A), ITO/MoO_3/MEH-PPV/F_{16}ZnPc/Ag cell (circles) and ITO/MoO_3/MEH-PPV/F_{16}ZnPc/BCP/Ag cell (stars) fabricated in the same cycle (B) [105]. λ=650 nm, illumination from the ITO side, thin polymer layers.

ways. The first explanation concerns finite surface recombination rate of majority carriers at the cathode in the absence of BCP, which means that extraction of elec-

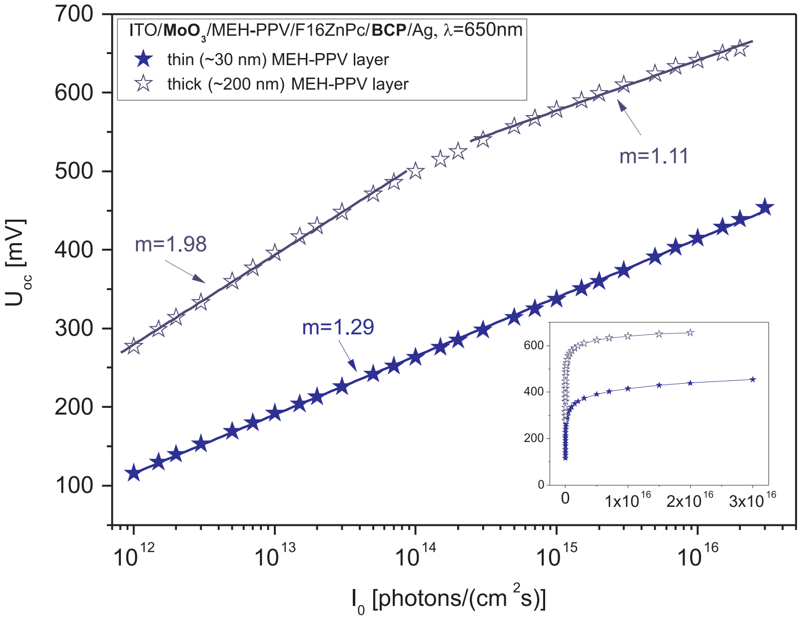

Figure 7.9: Open-circuit voltage as a function of incident light intensity for ITO/MoO$_3$/MEH-PPV/F$_{16}$ZnPc/BCP/Ag cells with a thin (stars) and thick (open stars) polymer layer. λ=650 nm, illumination from the ITO side.

trons at the F$_{16}$ZnPc/Ag contact is limited and these charge carriers accumulate at regarded interface creating space charge that reduces U_{oc} [120]. Introduction of the BCP layer might cause an improvement of electron extraction rate from the bulk to the electrode, giving rise to the open-circuit voltage. On the other hand, this upward shift of U_{oc} attributed to BCP is less pronounced in the presence of the anodic buffer layer (compare Figs. 7.8 A and B). Moreover, it is evident that another crucial factor affecting the value of U_{oc} is the polymer thickness (see Fig. 7.9) - the thicker the polymer is the higher is the value of open-circuit voltage. Therefore, thick polymer layers and presence of the BCP layer might limit the short-circuit effects (increasing shunt resistance). Another important fact is that cells without the BCP layer show fast saturation of the open-circuit voltage with increasing light intensity, whereas cells with this layer do not. The same saturation effect was found for ITO/CuPC/MePTCDI/Ag cells in the absence of the BCP interlayer [118] and was attributed to exciton quenching at the organic material/cathode interface. According to authors, introduction of the BCP interlayer disables the exciton quenching, preventing from saturation of U_{oc}. Therefore, the

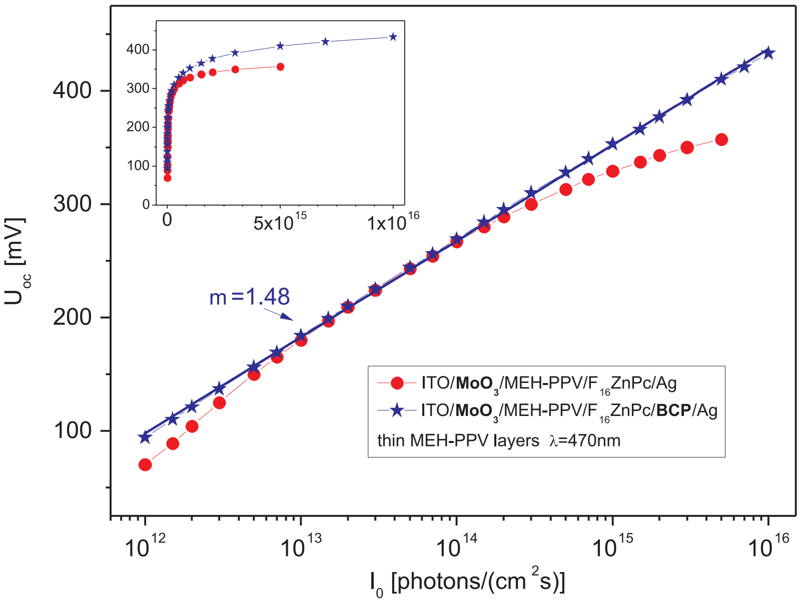

Figure 7.10: Open-circuit voltage as a function of incident light intensity for ITO/MoO_3/MEH-PPV/F_{16}ZnPc/Ag cell (circles) and ITO/MoO_3/MEH-PPV/F_{16}ZnPc/BCP/Ag cell (stars) fabricated in the same cycle. λ=470 nm, illumination from the ITO side, thin polymer layers.

role of BCP in the regarded MEH-PPV/F_{16}ZnPc system needs further consideration. Nevertheless, Eq. 4.68 can be used to describe the dependence of U_{oc} on I_0 for cells having the BCP interlayer

$$U_{oc} \approx \frac{mkT}{e} \ln\left(c_2 I_0\right) \ , \tag{7.1}$$

where m plays the role of diode ideality factor. Values of m obtained for all cells varied from 1.3 to 2.0 depending on the presence of buffer layers polymer thickness and wavelength of incident light. The lowest m value, indicating the smallest contribution of trap-assisted SRH recombination taking place at the donor/acceptor interface, was obtained for the cell with both buffer layers and thin polymer layer under monochromatic illumination of λ=650 nm (phthalocyanine absorption range). However, the same sample illuminated with monochromatic light from polymer absorption range, i.e. with λ=470 nm, showed higher m value, suggesting that processes of recombination of free charge carriers depend on the material excitons are generated in. The highest m value was found for the cell with thick polymer layer, which means that in this case free charge carriers recombine in the SRH manner at the donor/acceptor interface.

It is worth noting, that according to literature, maximum predicted value of U_{oc}, that is the difference between HOMO of the donor and LUMO of the acceptor positions divided by elementary charge, for the cells based on the MEH-PPV/F$_{16}$ZnPc junction is 0.7 V, while in the course of this research the open-circuit voltage equal to 0.65 V was obtained for cells with both buffer layers and 200 nm - thick polymer layer under monochromatic radiation of $2 \cdot 10^{16}$ photons/(cm^{2}s) and wavelength λ=650 nm, which is only 0.05 V lower than the predicted maximum value. Nevertheless, one must remember that HOMO and LUMO positions taken from literature may have an uncertainty of few tenths of eV and that might be the cause of such small difference between the predicted and experimental maximum open-circuit voltage value, since due to various unfavorable factors, maximum value of U_{oc} is usually about 0.3 V lower than the one resulting from the HOMO-LUMO offset.

7.1.3 Current - voltage characteristics

Due to the relative positions of HOMO/valence level of MEH-PPV/MoO$_3$ and Fermi level of ITO (see Fig. 7.1), the anode/donor contact should remain Ohmic for the injection of holes disregarding the presence of applied buffer layer. The F$_{16}$ZnPc/Ag contact should also be Ohmic but for the injection of electrons. The position of conduction band of BCP lets us assume that incorporation of this buffer layer should introduce a high potential barrier for the injection of electrons from both sides of the above mentioned junction, especially from the acceptor's side, for which the barrier height is at least 1.1eV. This should lead to a worse performance of the solar cell incorporating a BCP layer. However, it has been suggested that during cathode deposition process some metal atoms diffuse into a BCP layer and introduce additional sites inside its energy bandgap [121]. These sites are considered responsible for the conduction of electrons in this case. Probability that a free electron will be injected from ITO to MEH-PPV in the presence or absence of anodic buffer layer is very low, even at high negative polarizations of ITO electrode (according to literature potential barrier height is greater than 1.7 eV), just like the probability that a free hole from the cathode will be injected into F_{16}ZnPc HOMO level (potential barrier height is greater than 2.0 eV) disregarding the presence of a buffer layer and positive polarization of Ag. Thus we should expect a very low value of a dark current when a negative potential is applied to the anode. If a positive potential is applied to the latter we should observe mono and bimolecular recombination of free charge carriers (holes injected by ITO and electrons injected by Ag) at MEH-PPV/F_{16}ZnPc junction, as well as space charge limited currents (SCLC) due to high potential barriers for holes and electrons at that junction. Therefore, it is very probable that only holes contribute to the current flowing through the MEH-PPV layer and analogically, only electrons make their contribution to the current flowing through the F_{16}ZnPc layer. Structural defects of deposited layers may have additional impact on electric charge generation (e.g. thermal generation) and trapping processes, hence their presence may influence electric currents flowing through investigated cells, especially under revers bias, i.e. in case of negative polarization of ITO with respect to Ag.

Maximum dark current density values measured at a forward bias of 1 V for ITO/MEH-PPV/F_{16}ZnPc/Ag devices varied in a broad range $(10^{-7}\div10^{-5}$ A/cm$^{2})$ showing no direct dependence on the thickness of MEH-PPV layer. That could indicate a large number of defects in the investigated samples, especially in a donor layer, which means that this layer significantly contributes to a total series resistance and it may reduce the shunt resistance of a cell as well.

The effect of buffer layers on current-voltage characteristics of cells with thin MEH-PPV layers is shown in Figs. 7.11 and 7.12. Introduction of the BCP cathodic interlayer caused an increase in the dark current density under forward bias greater than 0.3 V and a reduction of one order of magnitude in the current density at a reverse bias, thus an increase in the rectification ratio - RR values calculated at ±0.3 V are 3 and 20 for the cells without and with the BCP buffer layer, respectively. On the contrary, cells provided with anodic buffer layer only had very low RR values, comparable to the ones found for cells with no buffer layers. Simultaneous insertion of the MoO_3 and BCP buffer layers brought about a notable increase in dark current density under forward bias. Currents flowing through these cells were more than two orders of magnitude higher than

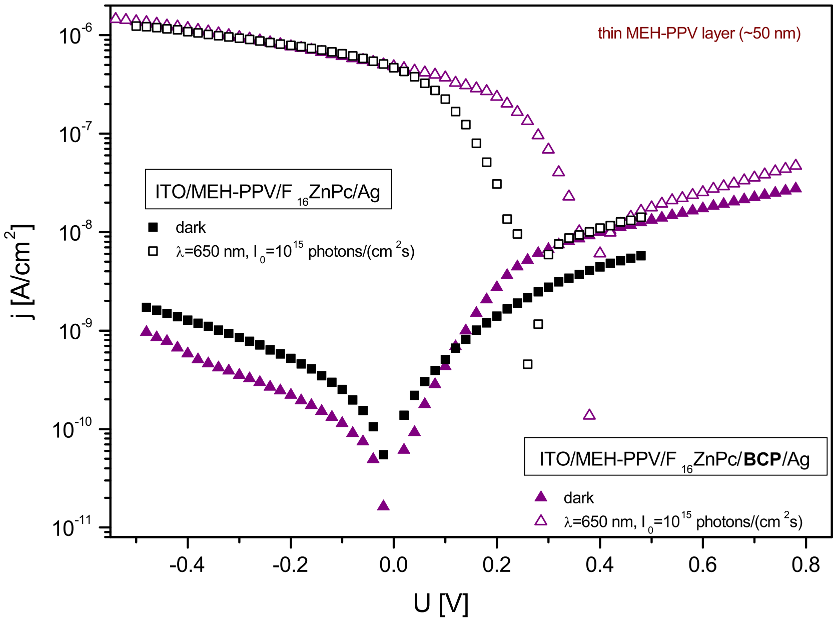

Figure 7.11: Current density vs. voltage measured in the dark and under monochromatic illumination of intensity $I_0 = 10^{15}$ photons/(cm^{2}s) and wavelength $\lambda = 650$ nm for ITO/MEH-PPV/F$_{16}$ZnPc/Ag (squares) and ITO/MEH-PPV/F$_{16}$ZnPc/BCP/Ag (triangles) cells fabricated in the same cycle.

those flowing through bare ITO/MEH-PPV/F$_{16}$ZnPc/Ag cells and the ones with MoO$_3$ layer only. As a result, high RR values exceeding 750 at ±0.3 V for devices with thin ($\sim$30 nm) polymer layers were obtained. This effect gives evidence of improved hole and electron injection from ITO and Ag electrodes to donor and acceptor layers respectively noted in the presence of both buffer layers, while reduction of the current density at the revers bias observed in the presence of BCP shows that this layer hampers the injection of holes from Ag. Such changes in the magnitude of current density may also indicate a reduction in series resistance of the cell. The same effects of simultaneous incorporation of MoO$_3$ and BCP buffer layers were observed for ITO/CuPc/MePTCDI/Ag cells [118]. The following sets of parameters describing the performance of investigated cells under monochromatic illumination of wavelength $\lambda = 650$ nm and intensity $I_0 = 10^{15}$ photons/(cm^{2}s) were obtained:

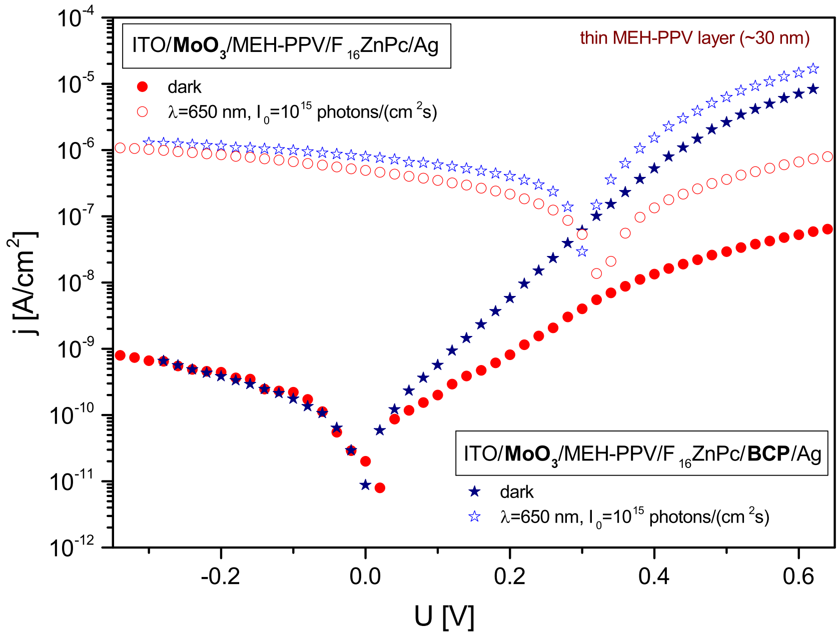

Figure 7.12: Current density vs. voltage measured in the dark and under monochromatic illumination of intensity $I_0 = 10^{15}$ photons/(cm^{2}s) and wavelength $\lambda = 650$ nm for ITO/MoO$_3$/MEH-PPV/F$_{16}$ZnPc/Ag (circles) and ITO/MoO$_3$/MEH-PPV/F$_{16}$ZnPc/BCP/Ag (stars) cells fabricated in the same cycle.

- ITO/MEH-PPV/F$_{16}$ZnPc/Ag with a 50 nm thick MEH-PPV layer
  j_{sc}=0.47 $\mu\mathrm{A/cm}^2$, U_{oc}=0.25 V, FF=0.19, η=0.007%
- ITO/MEH-PPV/F$_{16}$ZnPc/BCP/Ag with a 50 nm thick MEH-PPV layer
  j_{sc}=0.48 $\mu\mathrm{A/cm}^2$, U_{oc}=0.37 V, FF=0.27, η=0.016%
- ITO/MoO$_3$/MEH-PPV/F$_{16}$ZnPc/Ag with a 30 nm thick MEH-PPV layer
  j_{sc}=0.49 $\mu\mathrm{A/cm}^2$, U_{oc}=0.33 V, FF=0.27, η=0.014%
- ITO/MoO$_3$/MEH-PPV/F$_{16}$ZnPc/BCP/Ag with a 30 nm thick MEH-PPV layer
  j_{sc}=0.79 $\mu\mathrm{A/cm}^2$, U_{oc}=0.31 V, FF=0.33, η=0.026%

One must bare in mind, that only cells with identical thickness of both organic materials can be directly compared, since according to the CFA model current flowing through the cell and therefore all parameters characterizing the photovoltaic performance of this cell show thickness dependence. Moreover, optical field distribution that affects the performance of the cell also relies on the thickness of each layer.

S-shaped characteristics with a pronounced kink around U_{oc} and local saturation of current in the conducting direction were found for bare ITO/MEH-PPV/F_{16}ZnPc/Ag cells and those with the BCP buffer layer only. This might be a result of the already mentioned finite surface recombination rate of majority charge carriers postulated by Wagenpfhal et al. [120]. According to computer simulations run by the authors, decrease in this recombination rate limits power-conversion efficiency due to a drop in U_{oc}, j_{sc} and fill factor. However, it is evident that introduction of the BCP interlayer into ITO/MEH-PPV/F_{16}ZnPc/Ag cells causes a beneficial change in the shape of current-voltage characteristics, i.e. a notable increase in U_{oc} from 0.25 V to 0.37 V and FF from 0.19 to 0.27. However, BCP does not seem to affect j_{sc} value too much and saturation of current in the conducting direction is still present and it may follow from the problem with free charge carrier extraction at the ITO/MEH-PPV contact. Situation changes when MoO_3 is incorporated into the cell. In this case saturation of current is far less pronounced and diminishes completely in the presence of both buffer layers. Though the U_{oc} value extracted form the current-voltage characteristics for the cell with both buffer layers seems to be lower than the one of the cell with MoO_3 layer only the open-circuit voltage action spectra prove that the former cell shows higher values of U_{oc}. Therefore, we may conclude that simultaneous improvement in U_{oc}, j_{sc} and FF is observed in the presence of both buffer layers. A relatively high value of fill factor equal to 0.33 for devices fabricated, stored for few weeks and investigated in the ambient air was reached for cells with both buffer layers and a thin polymer layer, while the highest value of the open-circuit voltage of 0.61 V under these illumination conditions was obtained for diodes with both buffers but a thick polymer layer. However, thick polymer layer hampered charge transport and resulted in low rectification ratio in the dark, low current density values in the dark and under illumination and low fill factor of only 0.17.

It is worth noting that cells with high dark rectification ratios shown higher fill factors. Another fact that is worth mentioning is the difference between the shape

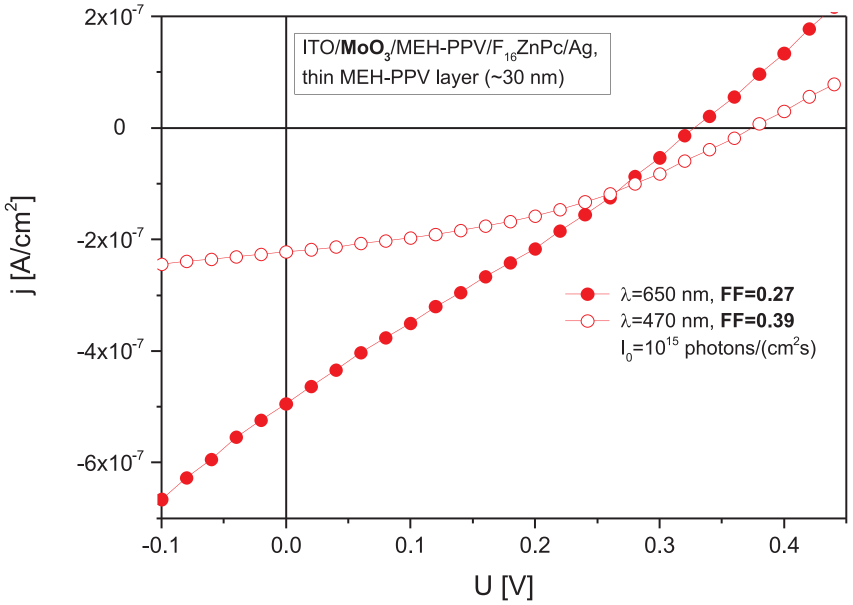

Figure 7.13: Current density versus voltage measured under monochromatic illumination of λ=650 nm (circles) and λ=470 nm (open circles) recorded for the ITO/MoO_3/MEH-PPV/F_{16}ZnPc/Ag cell at illumination intensity $I_0 > 10^{15}$ photons/(cm^2s).

of current-voltage curves obtained for the same device but illuminated with light of two different wavelengths. Fig. 7.13 shows an example of two current-voltage curves recorded for the same ITO/MoO_3/MEH-PPV/F_{16}ZnPc/Ag cell illuminated with light from donor absorption region (λ=470 nm) and acceptor absorption region (λ=650 nm). Such differences were observed for other investigated systems as well. As one may notice, short-circuit current density is much lower in the polymer absorption region but the shape of the curve at this wavelength is much closer to the ideal diode behavior and the fill factor is much higher (FF=0.39). This means it is probable that photogeneration efficiency, charge transport and/or charge collection differ depending on the material excitons are generated in. That might result from the positions of excitonic levels in donor and acceptor materials.

Since the model of a donor/acceptor junction developed in the course of this work considers devices with ohmic contacts only current-voltage data collected for the ITO/MoO_3/MEH-PPV/F_{16}ZnPc/Ag cell with a 30 nm thick polymer layer and an 80 nm thick phthalocyanine layer were fitted to this model (see Figs. 7.14 and 7.15). Good fits were obtained under the assumption that free electron concen-

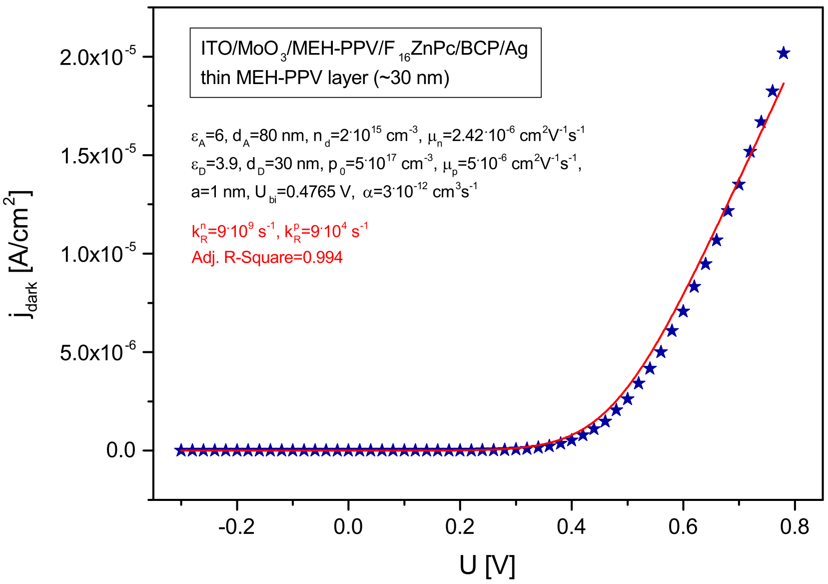

Figure 7.14: Dark current-voltage characteristics of the ITO/MoO$_3$/MEH-PPV/F$_{16}$ZnPc/Ag cell. Red line and values of k_R^p and k_R^n marked in red result from fitting the experimental data to the CFA model assuming that $\varepsilon_D = 3.9$, $p_0 = 5 \cdot 10^{17}$ cm^{-3}, $\mu_p = 5 \cdot 10^{-6}$ cm^{2}V^{-1}s^{-1}, $\varepsilon_A = 6$, $n_d = 0.986 \cdot 10^{15}$ cm^{-3}, a=1 nm, U_{bi}=0.48 V, $\mu_n = 5 \cdot 10^{-6}$ cm^{2}V^{-1}s^{-1} and $\alpha = 3.5 \cdot 10^{-12}$ cm^{3}s.

tration at the rear contact may depend on illumination conditions, while mobility of free charge carriers and free hole concentration at the front contact remain unchanged. The best fits were obtained for the following set of parameters

- $\varepsilon_D = 3.9$, $p_0 = 5 \cdot 10^{17}$ cm^{-3}, $\mu_p = 5 \cdot 10^{-6}$ cm^{2}V^{-1}s^{-1}, $\varepsilon_A = 6$, $\mu_n = 5 \cdot 10^{-6}$ cm^{2}V^{-1}s^{-1}, $a = 1$ nm, $U_{bi} = 0.48$ V, $\alpha = 3.5 \cdot 10^{-12}$ cm^{3}s

and

- $n_d = 0.986 \cdot 10^{15}$ cm^{-3}, $k_R^p = 10^5$ s^{-1}, $k_R^n = 10^{10}$ s^{-1} in the dark and
- $n_d = 1.92 \cdot 10^{15}$ cm^{-3}, $k_R^p = 10^5$ s^{-1}, $k_R^n = 9.6 \cdot 10^9$ s^{-1}, $G^{ex} = 2.5 \cdot 10^{23}$ cm^{-3}s^{-1} under monochromatic illumination of λ=650 nm and intensity $I_0 = 10^{15}$ photons/(cm^{2}s).

Illumination dependence of free electron concentration at the cathode was regarded due to the fact that, just as in case of single layer cells with CuI anode,

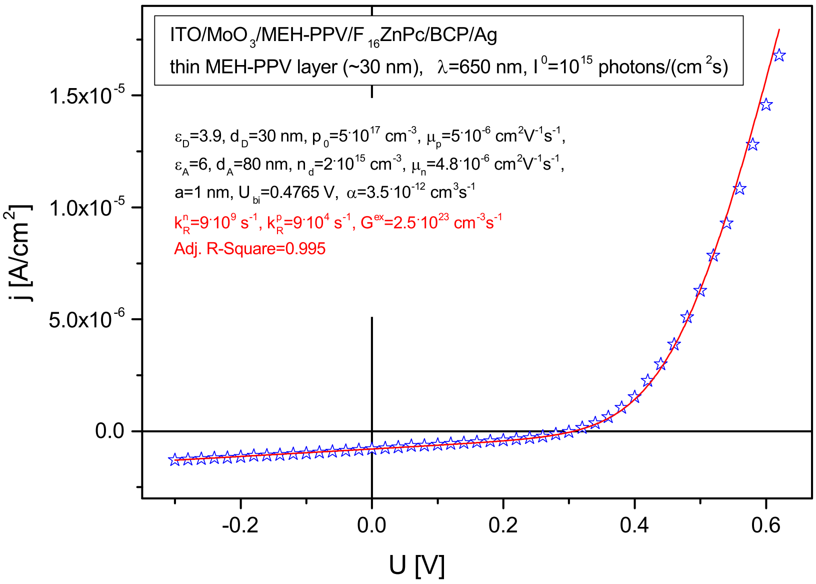

Figure 7.15: Current-voltage characteristics of the ITO/MoO$_3$/MEH-PPV/F$_{16}$ZnPc/Ag cell under monochromatic illumination of λ=650 nm and intensity $I_0 > 10^{15}$ photons/(cm^{2}s).Red line and values of k_R^p, k_R^n and G^{ex} marked in red result from fitting the experimental data to the CFA model assuming that $\varepsilon_D = 3.9$, $p_0 = 5 \cdot 10^{17}$ cm^{-3}, $\mu_p = 5 \cdot 10^{-6}$ cm^{2}V^{-1}s^{-1}, $\varepsilon_A = 6$, $n_d = 2 \cdot 10^{15}$ cm^{-3}, a=1 nm, U_{bi}=0.48 V, $\mu_n = 5 \cdot 10^{-6}$ cm^{2}V^{-1}s^{-1}, $\alpha = 3.5 \cdot 10^{-12}$ cm^{3}s^{-1}.

dark current-voltage characteristics and those collected under illumination for all bilayer MEH-PPV cells do not overlap each other, even under high forward bias. However, one must remember that this fact points out photoconductivity of the system, that can be attributed to light induced detrapping of free charge carriers that was not addressed during the derivation of the CFA model.

It has to be pointed out, that although the fits are good, monomolecular recombination constants resulting from these fits have large errors, exceeding the values of k_R^n and k_R^p. Suitable bimolecular recombination rate used during the fitting process was estimated from the Langevin model (Eq. 4.83), assuming that dielectric constant of the generation layer is equal to the average value of dielectric constants of donor and acceptor layers. The value of the built-in potential derived from the fits of current-voltage curves to the CFA model of a single layer cell with ITO anode and BCP/Ag back electrode was equal to 0.3 V, while the one found on the

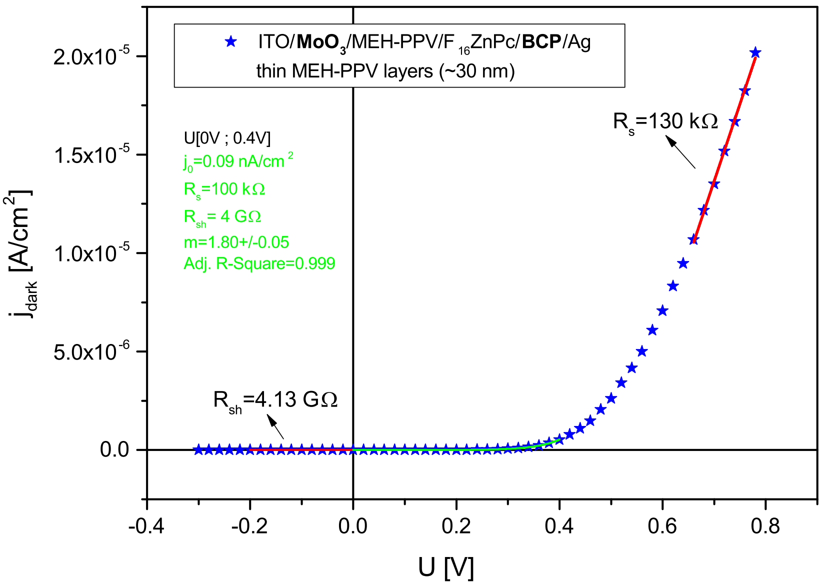

Figure 7.16: Dark current-voltage characteristics of the ITO/MoO_3/MEH-PPV/F_{16}ZnPc/Ag cell. Green line and parameters j_0, m, R_s, R_{sh} and Adj. R-Square show the results of the fit of experimental values to the SEC model in the 0÷0.4 V voltage range. Arrows point out series and shunt resistances estimated from the slopes of the linear parts of the curve.

basis of the CFA model and experimental data collected for the bilayer cell with ITO/MoO_3 front contact and BCP/Ag back contact equals 0.48 V. These results suggest that MoO_3 may modify the ITO work function enhancing the built-in field within the cell, therefore it may have a positive effect on the open-circuit voltage of the cell, as it was stated by Kinoshita et al. [100]. Furthermore, values of the open-circuit voltage found for the regarded cell exceeded the extracted value of the built-in voltage introduced by ITO/MoO_3 and BCP/Ag electrodes.

It is also worth noting, that according to the fits, monomolecular recombination rate of free holes is five orders of magnitude lower than the one found for free electrons.

The same current-voltage curves were fitted to the SEC model, according to the same procedure as previously. Initial values of resistances calculated from the linear parts of the curves, along with diode ideality factor and saturation current density resulting from the $\ln x$ vs. $(U - JRs)$ plots were

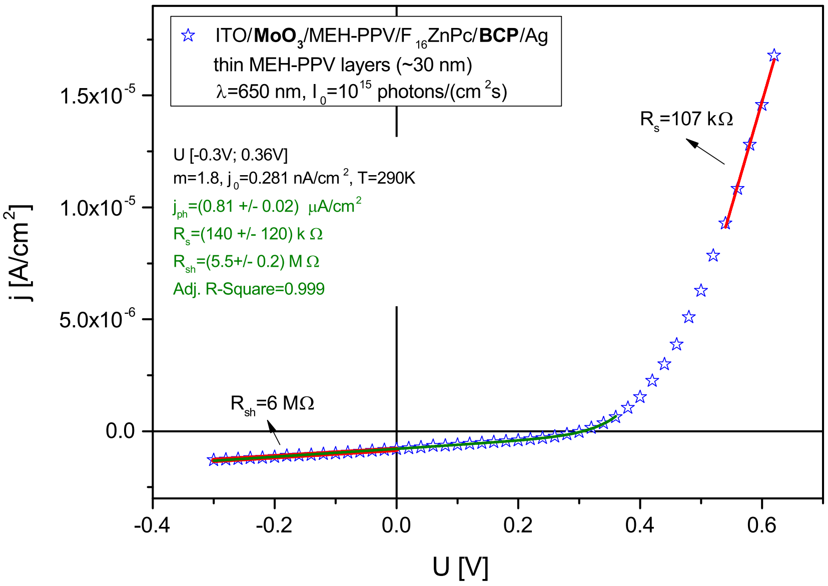

Figure 7.17: Current-voltage characteristics of the ITO/MoO$_3$/MEH-PPV/F$_{16}$ZnPc/Ag cell under monochromatic illumination of λ=650 nm and intensity $I_0 > 10^{15}$ photons/(cm^{2}s). Green line and parameters j_0, j_{ph}, m, R_s, R_{sh} and Adj. R-Square show the results of the fit of experimental values to the SEC model in the -0.3 ÷0.36 V voltage range. Arrows point out series and shunt resistances estimated from the slopes of the linear parts of the curve. Illumination from the front side.

- in the dark
  R_s=130 kΩ, R_{sh}=4.13 GΩ, j_0=0.085 nA/cm^2 and m=1.8,

- under monochromatic illumination of λ=650 nm and intensity
  $I_0 = 10^{15}$ photons/(cm^{2}s)
  R_s=107 kΩ, R_{sh}=6 MΩ, j_0=0.2 nA/cm^2 and m=1.69.

Good agreement between the experimental data and the regarded model was obtained in the dark and under illumination in limited, i.e. 0÷0.4 V and -0.3 V÷0.36 V, voltage ranges respectively and the following values of cell parameters, consistent with their initial values, were found

- in the dark
  R_s=100 kΩ, R_{sh}=4 GΩ, j_0=0.09 nA/cm^2 and m=1.8,

- under monochromatic illumination of λ=650 nm and intensity $I_0 = 10^{15}$ photons/(cm^{2}s)
  R_s=140 kΩ, R_{sh}=5.5 MΩ, j_0=0.281 nA/cm^2, j_{ph}=0.81 μA/cm^2 m=1.8.

It is worth noting, that the same diode ideality factor of 1.8 was found in the dark and under illumination, suggesting the major role of monomolecular free charge carrier recombination. Therefore, we may try to analyze parameters of the cell derived from the SEC model in terms of the drift-diffusion model neglecting bimolcecular recombination proposed in the course of this study (see Eq. 4.96). According to the latter model along with extracted values of free charge carrier mobilities and concentrations at both electrodes, as well as recombination and dielectric constants, current density under high reverse bias can be approximated with the following expressions

$$j_{dark} \approx -e\mu_n \frac{k_R^p p_j^{th} + k_R^n n_j^{th}}{k_R^n d_A \left(1 + \frac{\varepsilon_A d_D}{\varepsilon_D d_A}\right)} \left(U^{bi} - U\right) \tag{7.2}$$

$$j \approx -e\mu_n \frac{G^{ex}}{k_R^n d_A \left(1 + \frac{\varepsilon_A d_D}{\varepsilon_D d_A}\right)} \left(U^{bi} - U\right) . \tag{7.3}$$

Under high forward bias the acceptor layer governs the current flow, thus

$$j = j_{dark} \approx -\frac{e\mu_n n_d}{d_A \left(1 + \frac{\varepsilon_A d_D}{\varepsilon_D d_A}\right)} \left(U^{bi} - U\right) . \tag{7.4}$$

Since in all these cases current varies linearly with applied voltage we may relate series and shunt resistances of the cell with properties of donor and acceptor layers. Keeping in mind the illumination dependence of free electron concentration at the rear contact we obtain

$$R_s^{dark} \approx \frac{d_A \left(1 + \frac{\varepsilon_A d_D}{\varepsilon_D d_A}\right)}{e\mu_n n_d^{dark}} AA^{-1} \approx 160 \text{ k}\Omega , \tag{7.5}$$

$$R_s^{ill} \approx \frac{d_A \left(1 + \frac{\varepsilon_A d_D}{\varepsilon_D d_A}\right)}{e\mu_n n_d^{ill}} AA^{-1} \approx 80 \text{ k}\Omega , \tag{7.6}$$

$$R_{sh}^{dark} \approx \frac{d_A \left(1 + \frac{\varepsilon_A d_D}{\varepsilon_D d_A}\right)}{e\mu_n} \left[\left(\frac{k_R^p}{k_R^n} p_j^{th} + n_j^{th} \right)^{-1} - \frac{1}{n_d^{dark}} \right] AA^{-1} \approx 9.7 \text{ G}\Omega , \tag{7.7}$$

while

$$R_{sh}^{ill} \approx \frac{d_A \left(1 + \frac{\varepsilon_A d_D}{\varepsilon_D d_A}\right)}{e\mu_n} \left(\frac{k_R^n}{G^{ex}} - \frac{1}{n_d^{ill}} \right) AA^{-1} \approx 5.6 \text{ M}\Omega . \tag{7.8}$$

Resistances calculated on the basis of these simplified expressions stand in close agreement with the ones calculated from the slopes of linear parts of presented current-voltage plots. We may conclude, that as long as mobility of free charge carriers and free charge carrier concentrations at electrodes are independent of illumination series resistance remains constant. Otherwise, the latter decreases with illumination as a result of enhanced free charge carrier transport. This enhancement causes further deterioration of the shunt resistance that decreases with light intensity due to the rise in photogeneration rate. Deterioration of R_{sh} under illumination is commonly observed in case of organic solar cells. Moreover, even if one of the layers governs the current flow throughout the cell, some properties of the other layer, namely its thickness and dielectric constant, still affect both resistances. Withal, we may notice that the built-in field also plays quite a significant role as it affects thermal equilibrium concentrations of free charge carriers at the donor/acceptor junction that influence the dark shunt resistance of the cell.

Further comparison of regarded models indicates that the open-circuit voltage determined from the derived CFA model is a complicated function of a large number of parameters and even in a simple case of monomolecular recombination only (see Eq. 4.109) it is hardly ever analogous to the one given by Eq. 4.67 determining the open-circuit voltage in the SEC model. Open-circuit voltage expressions determined from these two models are consistent with each other only if $\frac{\varepsilon_A d_D}{\varepsilon_D d_A} = 1$ and $\alpha \approx 0$. Then

$$U_{oc} = \frac{2kT}{e} \ln\left(\frac{G^{ex}}{G^{th}} + 1\right) \ . \tag{7.9}$$

Therefore, we may infer that the diode ideality factor m equal to 2 does indicate that monomolecular recombination of free charge carriers within the D/A interface is the main free charge carrier quenching process, while G^{ex}/G^{th} ratio is analogous to the j_{ph}/j_0 ratio. This analogy shows that saturation current density j_0, as well as photogeneration current are dependent on the properties of the donor/acceptor junction if bulk generation can be neglected. Moreover, if $\frac{\varepsilon_A d_D}{\varepsilon_D d_A} \neq 1$ the physical meaning of the diode ideality factor can not be easily interpreted in terms of the derived CFA model.

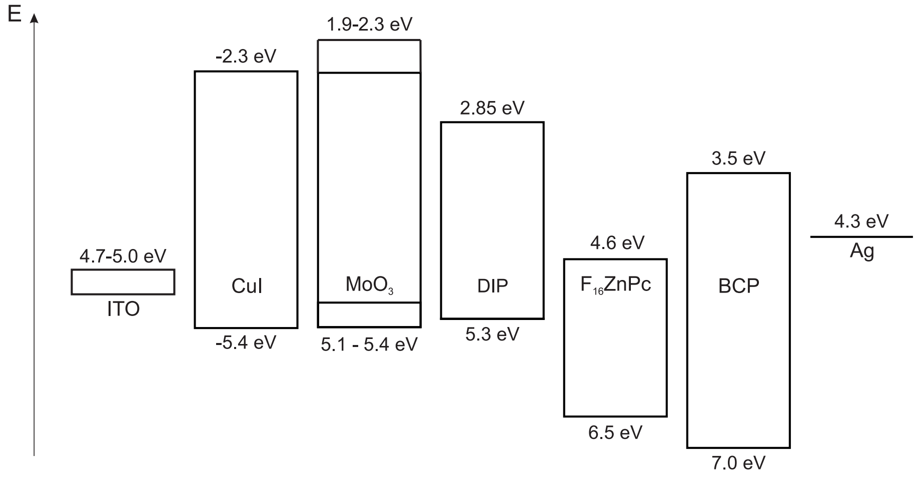

Figure 7.18: Energy level diagram of materials forming the investigated cells.

7.2 Bilayer cells based on the DIP/F_{16}ZnPc heterojunction

As absorption spectra of DIP and F_{16}ZnPc complement one another and HOMO-LUMO offset between these two materials is 0.75 eV, photovoltaic cells based on this junction should be able to harvest light quite efficiently within the whole visible range and should be able to generate voltage up to 0.75 V. Moreover, DIP has already proved its applicability in organic photovoltaics. For the aforementioned reasons ITO/MoO_3/DIP/F_{16}ZnPc/BCP/Ag cells were fabricated but their performance was very poor. Therefore, another structure containing the same donor/acceptor heterojunction but CuI instead of ITO/MoO_3 was fabricated and investigated, as such CuI anode proved its applicability in single layer cells. Selected results of the research carried out for both of the aforementioned systems, namely ITO/MoO_3/DIP/F_{16}ZnPc/BCP/Ag and CuI/DIP/F_{16}ZnPc/BCP/Ag cells are presented below. Energy band diagram of materials forming these systems is shown in Fig. 7.18.

7.2.1 Short-circuit current and open-circuit voltage action spectra

Short-circuit current action spectrum of the ITO/MoO_3/DIP/F_{16}ZnPc/BCP/Ag cell collected at constant light intensity of 10^{14} photons/(cm^{2}s) and illumination from

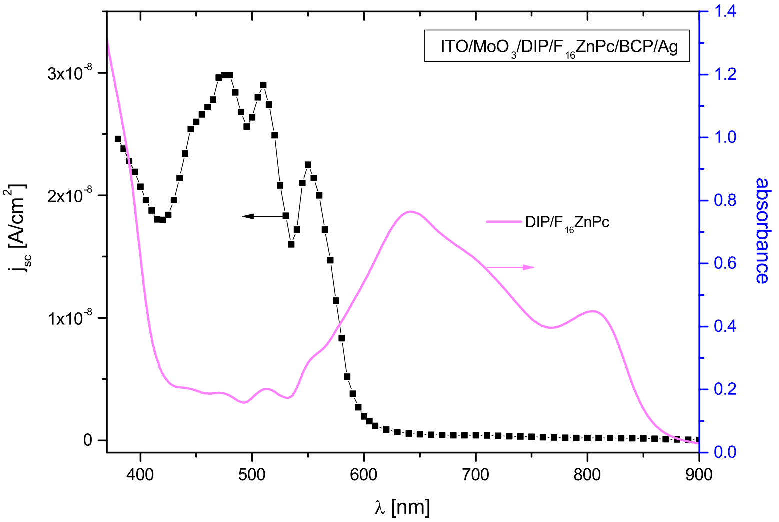

Figure 7.19: Spectral response of short-circuit current of the ITO/MoO$_3$/DIP/F$_{16}$ZnPc/Ag cell (squares) and DIP/F$_{16}$ZnPc absorption spectrum (pink line). $I_0 = 10^{14}$ photons/(cm^{2}s), illumination from the ITO side.

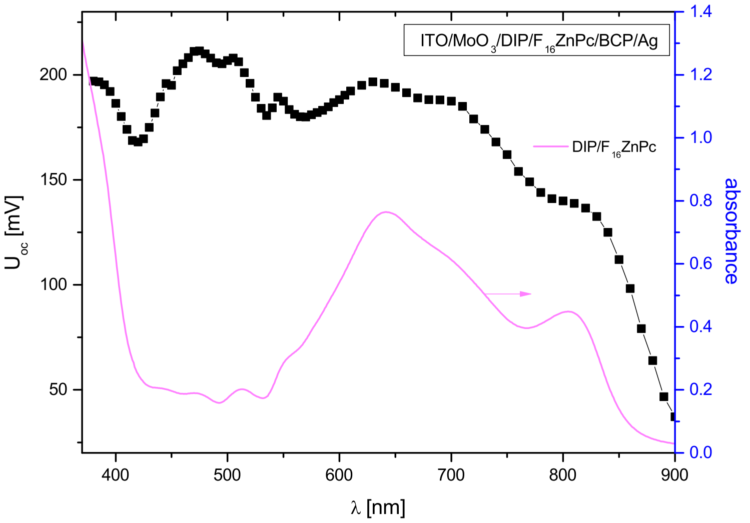

Figure 7.20: Spectral response of short-circuit current of the ITO/MoO$_3$/DIP/F$_{16}$ZnPc/Ag cell (squares) and DIP/F$_{16}$ZnPc absorption spectrum (pink line). $I_0 = 10^{14}$ photons/(cm^{2}s), illumination from the ITO side.

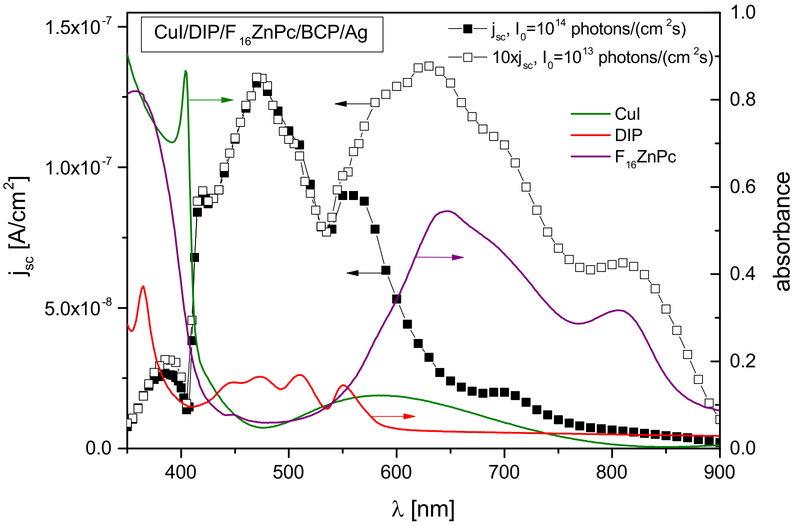

Figure 7.21: Spectral response of short-circuit current of the CuI/DIP/F$_{16}$ZnPc/Ag cell at $I_0 = 10^{14}$ photons/photons/(cm^{2}s) (black squares) and $I_0 = 10^{13}$ photons/(cm^{2}s) (open squares), absorption spectra of F$_{16}$ZnPc (violet line), DIP (red line) and CuI (green line). Illumination from the CuI side, I_0 is the intensity of light at the glass/CuI interface. Note magnification of the current measured at lower illumination intensity.

the ITO side is shown in Fig. 7.19. As one can see, though a donor/acceptor heterojunction was used currents flowing through the cell at wavelengths below 600 nm are low, since current density measured for this system is comparable to the one obtained for the single layer ITO/F$_{16}$ZnPc/BCP/Ag cells. Furthermore, j_{sc} action spectrum follows the absorption of DIP, but surprisingly, practically no current flows through the cells at wavelengths longer than 600 nm, i.e in the region of phthalocyanine absorption. This indicates that the active junction could be located not at the DIP/F$_{16}$ZnPc junction, but in the vicinity of the ITO anode. However, the open-circuit voltage action spectrum (Fig. 7.20) shows symbatic relationship with absorption spectrum of DIP/F$_{16}$ZnPc bilayer in the whole investigated spectral range, which points out that photogeneration of charge carriers takes place rather near the donor/acceptor interface. No current flow at wavelengths longer than 600 nm suggests, that for some reason there is a problem with charge carrier transport and/or collection if free charge carriers origin from photoexcitation of the acceptor layer. If we take a look at the j_{sc} action spectrum collected for the

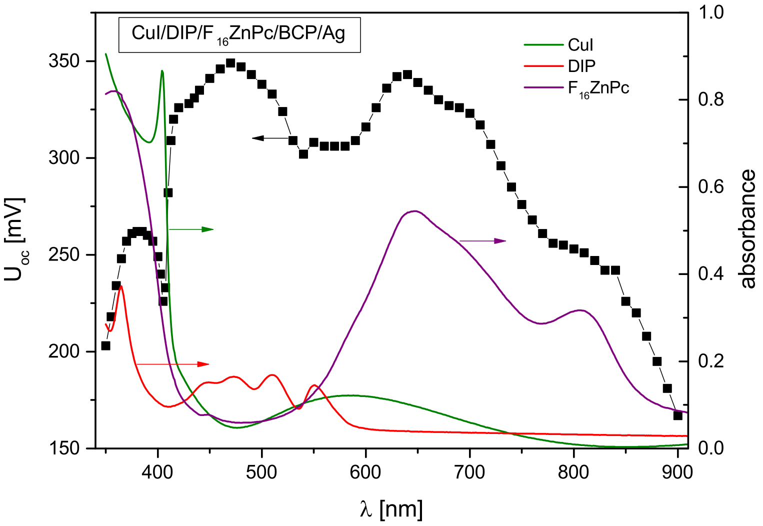

Figure 7.22: Spectral response of short-circuit current of the CuI/DIP/F_{16}ZnPc/Ag cell (squares) absorption spectra of F_{16}ZnPc (violet line), DIP (red line) and CuI (green line). $I_0 = 10^{14}$ photons/(cm^{2}s) at the glass/CuI interface, illumination from the CuI side.

cells with CuI anode under the same illumination conditions (black squares in Fig. 7.21) we will notice that

- current density is about 5 times greater than for the cells with ITO, though absorption of CuI lowers light intensity at the DIP/F_{16}ZnPc junction,
- the same problem, namely no current flow at longer wavelengths, occurs for both systems.

Situation changes when illumination intensity is one order of magnitude lower (open squares in Fig. 7.21; note magnification of the current). In this case, short-circuit current follows absorption spectra of both organic semiconductors for λ>410 nm, just like the action spectrum of U_{oc} measured at 10^{14} photons/(cm^{2}s) (Fig. 7.22). Voltage and current drop observed at shorter wavelengths can be associated with strong absorption of CuI. Therefore, it seems that the lower the number of excitons generated in the phthalocyanine layer is the higher is the efficiency of transport and/or collection of free charge carriers in both systems based on the DIP/F_{16}ZnPc heterojunction. The open-circuit voltage is about 150 mV higher

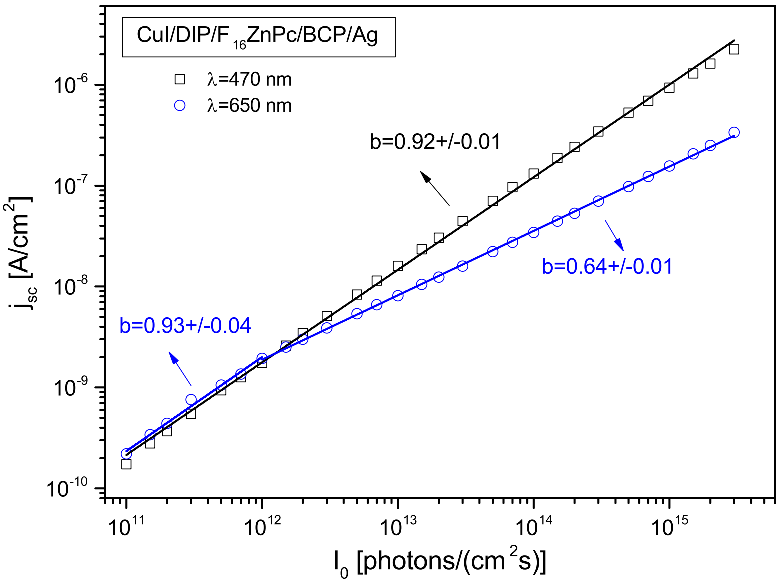

Figure 7.23: Illumination intensity dependence of short-circuit current density found for the CuI/DIP/F_{16}ZnPc/Ag cell under monochromatic illumination of wavelength λ=470 nm (open squares) or 650 nm (open circles). I_0 is the intensity of light at the glass/CuI interface, illumination from the CuI side.

for the cells with CuI anode than for the ones with ITO as long as CuI does not absorb too much light. Since former cells show better performance than the ones with ITO/MoO_3 anode, only results regarding the former system will be presented in the next part of this thesis.

7.2.2 Light intensity dependence of short-circuit current and open-circuit voltage

The effect of illumination intensity on short-circuit current density and open-circuit voltage for two different wavelengths, namely 470 nm from the DIP absorption range and 650 nm from the phthalocyanine absorption range, is presented in Figs. 7.23 and 7.24. These characteristics suggest that at short-circuit conditions monomolecular recombination of free charge carriers at the donor/acceptor junction is the main quenching process when free charge carriers are generated as

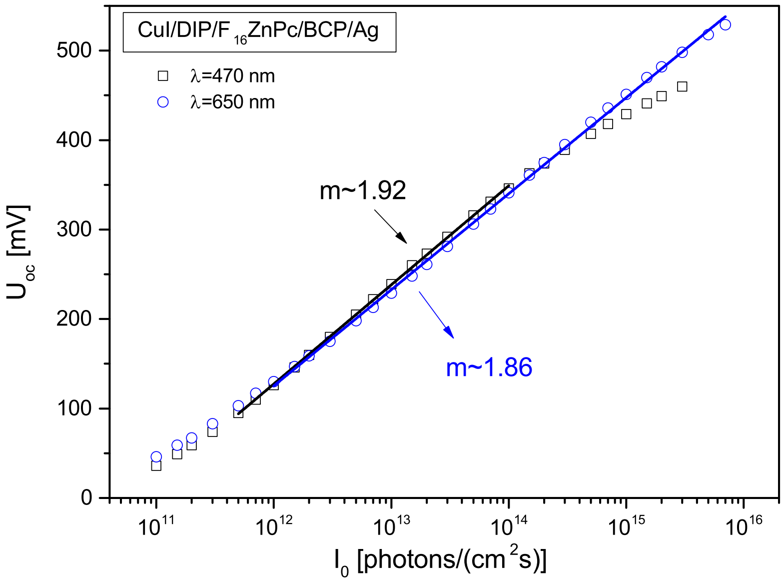

Figure 7.24: Illumination intensity dependence of open-circuit voltage found for the CuI/DIP/F_{16}ZnPc/Ag cell under monochromatic illumination of wavelength λ=470 nm (open squares) or 650 nm (open circles). I_0 is the intensity of light at the glass/CuI interface, illumination from the CuI side.

a result of photoexcitation of the DIP layer ($b \approx$ 0.92 within the whole experimental range), while even at low light intensities population of free charge carriers is diminished mainly in a bimolecular manner when these carriers origin from dissociation of excitons generated in the phthalocyanine layer ($b \approx$ 0.64 above 10^{12} photons/(cm^{2}s)). However, the diode ideality factors of 1.92 at 470 nm and 1.86 at 650 nm extracted from the $U_{oc}(I_0)$ plots imply that at open-circuit monomolecular recombination of free charge carriers is the main recombination process regardless of the wavelength. On the basis of these results the character of j_{sc} and U_{oc} action spectra can be explained. Such wavelength dependence of the dominant recombination type at short-circuit suggests that there is a problem with free charge carrier separation after exciton dissociation at the D/A junction if the acceptor layer is the absorbing one. Moreover, HOMO and LUMO levels of DIP are practically identical as the positions of HOMO and LUMO levels of MEH-PPV and current flowing through the cell with the latter donor material and the same

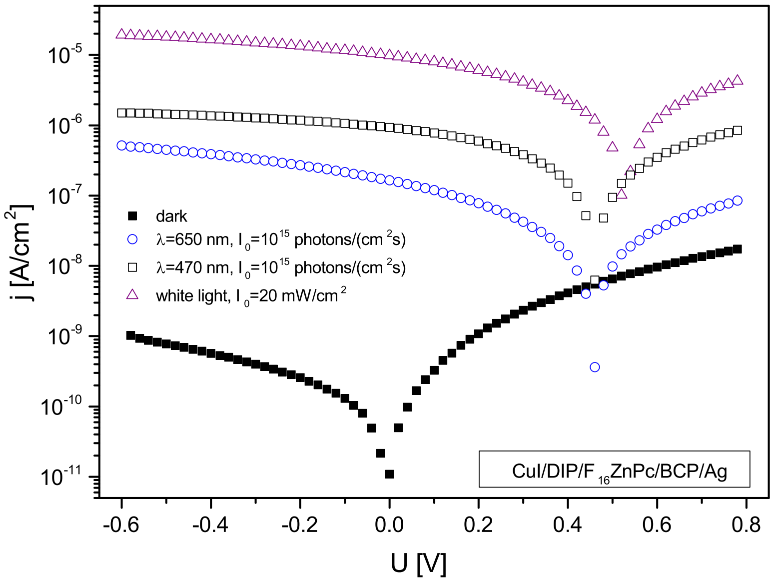

Figure 7.25: Current-voltage characteristics collected for the CuI/DIP/F_{16}ZnPc/BCP/Ag cell in the dark and under different illumination conditions. I_0 is the intensity of light at the glass/CuI interface, illumination from the CuI side.

set of electrodes upon illumination from the phthalocyanine absorption range is of the same magnitude as the on measured upon illumination from the MEH-PPV absorption range. Nevertheless, it is evident that the shape of the current-voltage curves of these cells depend on the photoexcited material. Therefore, it seems that efficiency of free charge carrier extraction, transport or collection is dependent upon relative positions of excitonic levels of donor and acceptor materials and electric field within the cell.

7.2.3 Current - voltage characteristics

According to energy level band diagram presented in Fig. 7.18, positive polarization of ITO or CuI means that the investigated cells are under forward bias. Current-voltage characteristics were collected in the dark, under monochromatic illumination of two different wavelengths, namely 470 nm and 650 nm, and intensity $I_0 = 10^{15}$ photons/(cm^{2}s) as well as under white light illumination of intensity

I_0 =20 mW/cm^2. These characteristics are shown in Fig. 7.25. Very low rectification ratio of about 9 under bias of ±0.6 V was found. Dark and photocurrents flowing through the cell under forward bias are very low suggesting free charge carrier injection/extraction and transport problems along with great recombination losses related to low mobility of free charge carriers and high recombination constants (see. Fig. 4.8). Moreover, photoconductivity of the system is strongly pronounced as the photocurrent at high forward bias is even three ranges of magnitude higher than the dark current. Photovoltaic parameters of the investigated CuI/DIP/F$_{16}$ZnPc/BCP/Ag cells extracted from the experimental data are given below

- λ=650 nm, $I_0= 10^{15}$ photons/(cm^{2}s)
  j_{sc}=0.165 μA/cm^2, U_{oc}=0.45 V, FF=0.21, η=0.005%,
- λ=470 nm, $I_0= 10^{15}$ photons/(cm^{2}s)
  j_{sc}=0.932 μA/cm^2, U_{oc}=0.47 V, FF=0.28, η=0.029%,
- white light illumination of intensity I_0=20 mW/cm^2
  j_{sc}=9.87 μA/cm^2, U_{oc}=0.53 V, FF=0.24, η=0.006%,

It is evident, that although the values of the open-circuit voltage are relatively high short circuit-current density, fill factor and as a consequence energy conversion efficiency are unsatisfactory. Just as in case of bilayer cells with the MEH-PPV layer, better performance of the cell was observed under monochromatic illumination of wavelength λ=470 nm from the donor absorption range.

Though relatively good fits of experimental data to the derived CFA model were obtained parameters resulting from these fits were inconsistent with each other, therefore this model can not be used to describe the current-voltage behavior of this system. Parameters characterizing properties of the cell according to the SEC model predetermined from the dark-current voltage curve as described before were

- m=5.3, j_0=0.3 nA/cm^2, R_{sh}=9 GΩ and R_s=0.47 GΩ ,

while the following set of data was obtained from the best fit for this model in the -0.1 V÷0.5 V range (see Fig. 7.26)

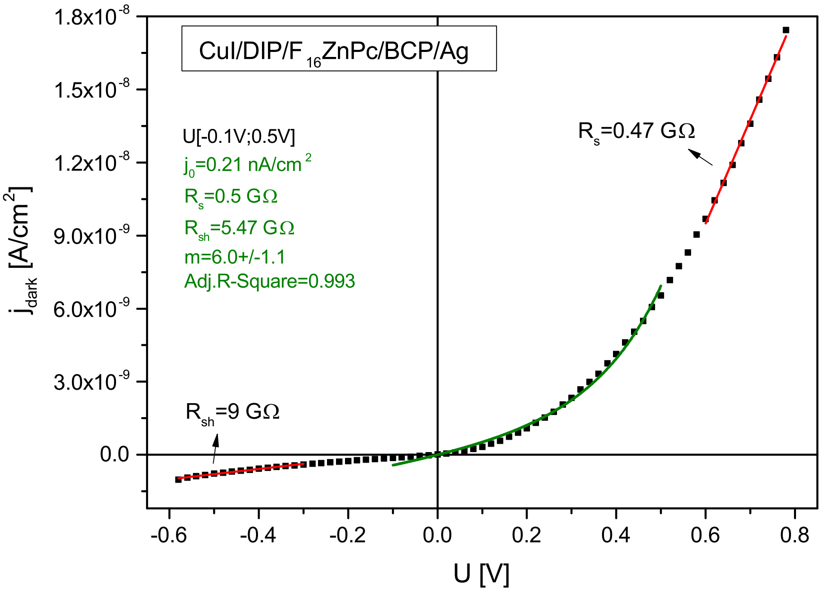

Figure 7.26: The best fit of the SEC model to the dark current-voltage characteristics collected for the CuI/DIP/F$_{16}$ZnPc/BCP/Ag cell.

- m=6.0±1.1, j_0=0.21 nA/cm^2, R_{sh}=5.47 GΩ and R_s=0.5 GΩ .

Although these values stand in close agreement with each other the diode ideality factor found for the CuI/DIP/F$_{16}$ZnPc/BCP/Ag cell is much greater than 2, therefore interpretation of the current-voltage behavior of this cell on the basis of this model is also impossible. The only reasonable conclusion that can be drawn for this system is its very high series resistance, that is three orders of magnitude greater than in case of all other investigated single and bilayer cells. Since the phthalocyanine/BCP/Ag contact is ohmic such high resistance suggests free charge carrier injection and extraction barriers at the front contact as well as problems with free charge carrier transport through the bulk of the cell. It is very probable that the CuI/DIP contact, just as the ITO/MoO$_3$/DIP one, is not ohmic and a proper anode should be found in order to improve the performance of the cell. Nevertheless, a strong dependence of cells performance on the wavelength of incident light suggests that relative positions of HOMO/LUMO and excitonic levels in these materials is disadvantageous for efficient light harvesting.

7.3 Conclusions

- Disregarding electrodes and buffer layers cells based on the investigated heterojunctions, i.e. MEH-PPV/F_{16}ZnPc and DIP/F_{16}ZnPc, shown photovoltaic action resulting from exciton dissociation at the donor/acceptor interface.

- Just as in case of single layer cells, all investigated devices show pronounced photoconductivity that may result from the free charge carrier detrapping process, since bulk generation of free charge carriers in organic materials upon illumination from the visible range is rather uncommon.

- CFA and SEC models were used to describe the current-voltage behavior of the ITO/MoO_3/MEH-PPV/F_{16}ZnPc/BCP/Ag cell. Nevertheless, due to photoconductivity, illumination dependence of free electron concentration at the rear contact and series resistance had to be assumed.

- Buffer layers, namely MoO_3 and BCP, enhance collective and injecting properties of ITO and Ag electrodes respectively. Moreover, it seems that BCP can prevent from exciton quenching at organic material/cathode interface obviating the saturation of the open-circuit voltage with light intensity. In the course of this study the direct influence of MoO_3 on the open-circuit voltage was not observed, although comparison of the collected experimental data and the derived CFA models of single and bilayer cells suggests, that MoO_3 modifies the ITO work function and enhances the built-in field within the cell, therefore it may have a positive effect on the open-circuit voltage.

- None of the regarded models is suitable for the analysis of the current-voltage behavior of the cells based on the DIP/F_{16}ZnPc heterojunction, for which the dark current under forward bias was very low, while photocurrent strongly dependent on illumination conditions. It is possible, that both models failed to fit the experimental data due to non-ohmic character of the front electrode and pronounced photoconductivity of the investigated structure.

- When the ratio $\frac{\varepsilon_A d_D}{\varepsilon_D d_A}$ equals 1 and bimolecular recombination can be neglected there is an analogy between the ratio of photo and thermal generation rates characteristic for the derived CFA model and the ratio of photogeneration and saturation currents, while the diode ideality factor is equal to 2. Otherwise, the physical meaning of the diode ideality factor is difficult to determine.

- The derived CFA model explains the origin of illumination dependence of shunt resistance of a cell.

Chapter 8

Summary

The course of photovoltaic phenomenon in organic photovoltaic cells utilizing thin layers of perfluorozincphthalocyanine was studied in few single and planar bilayer configurations. On the basis of collected experimental data mechanisms of photogeneration and recombination of free charge carriers were determined and active interfaces were localized. In case of single layer cells these interfaces were located at the front electrode/F_{16}ZnPc junctions, whereas photogeneration of free charge carriers in all investigated bilayer systems took place at the donor/acceptor junctions.

In order to relate the phenomena observed in the investigated systems with electric properties of materials forming these systems and their thickness, theoretical models describing the current-voltage behavior of single layer excitonic cells and planar bilayer cells (termed the CFA models) were developed. These models show how free charge carrier mobilities, electrode work functions, dielectric constants and thickness of donor and acceptor layers along with mono and bimolecular recombination constants affect the shape of the current-voltage curves. Knowing this dependence, such important physical quantities as the open-circuit voltage and short-circuit current were correlated with the aforementioned parameters. Subsequently, experimental data collected for all investigated systems were analyzed on the basis of the developed models and the Shockley equivalent circuit model commonly used for organic solar cells. Although good fits of the derived CFA models to experimental data, apart from the data collected for the cells based on the DIP/F_{16}ZnPc heterojunction, were obtained, light intensity dependence of free electron concentration at the rear F_{16}ZnPc/BCP/Ag contact had to be assumed, due to marked photoconductivity shown by all investigated systems. This photoconductivity may origin from the light induced free charge carrier detrapping process, since the bulk generation of free charge carriers in organic materials upon illumination in the visible range is rather uncommon. Therefore, further improvement of the CFA models via introduction of the former process into the equations describing generation-recombination kinetics may bring better understanding of photoelectric properties of single layer and bilayer systems showing pronounced photoconductivity. Nevertheless, comparison of the derived CFA models and the SEC model brought some insight on the relation between physical properties of the layers forming the modeled cells and parameters characterizing performance of a cell, such as series and shunt resistances, diode ideality factor or photogeneration and saturation currents. Inter alia, it was possible to explain the illumination dependence of the shunt resistance commonly observed in case of organic solar cells. Moreover, it was shown that one of the layers of the D/A systems may govern the current flow and that the free charge carrier mobility is not necessarily the most important factor influencing the free charge carrier transport through the cell, since the latter might be mainly affected by the $\frac{\varepsilon_A d_D}{\varepsilon_D d_A}$ ratio. Furthermore, according to the developed CFA model the open-circuit voltage can exceed the built-in voltage and the latter has a strong impact on free charge carrier collection.

Surprisingly, the best photovoltaic performance, even under white light illumination, was shown by the single layer CuI/F_{16}ZnPc/BCP/Ag cell, though in contrast to the fabricated bilayer cells it utilized light from a narrower range of wavelengths. Further increase of the performance of this system is possible if optimization of the phthalocyanine layer is made. Such optimization is also necessary in case of investigated bilayer cells. All in all, relatively high values of fill factors and open-circuit voltage obtained in the course of this study lead to the conclusion, that the investigated material, namely F_{16}ZnPc, may be a promising material for the applications in the field of organic photovoltaics.

Appendix A

Fabrication and characterization of individual layers

A.1 Coating techniques

Many different deposition techniques including PVD (physical vapor deposition), CVD (chemical vapor deposition), MBE (molecular beam epitaxy), MS (magnetron sputtering), spin coating, dip coating, inkjet printing, doctor blade and drop casting have been developed for the production of thin films of organic and inorganic materials. The choice of the most suitable method depends on a great variety of factors, among which type and solubility of deposited material as well as scale of the device play the most significant role. Herein coating techniques used to fabricate devices described in this thesis, i.e. PVD and spin coating, are presented.

- **Physical vapour deposition**
  Physical vapour deposition (PVD) is the most common method used for deposition of insoluble organic materials e.g. phthalocynanines, porphyrins, fullerenes, and inorganic materials e.g. metals, oxides and inorganic semiconductors. Furthermore, this technique can be used as alternative deposition method for some soluble materials, like P3HT [122]. A typical setup used for PVD is presented in Fig. A.1. PVD is a vacuum sublimation process taking place in a vacuum chamber under very low pressure (high vacuum). During this process small amounts of a deposited material are placed in

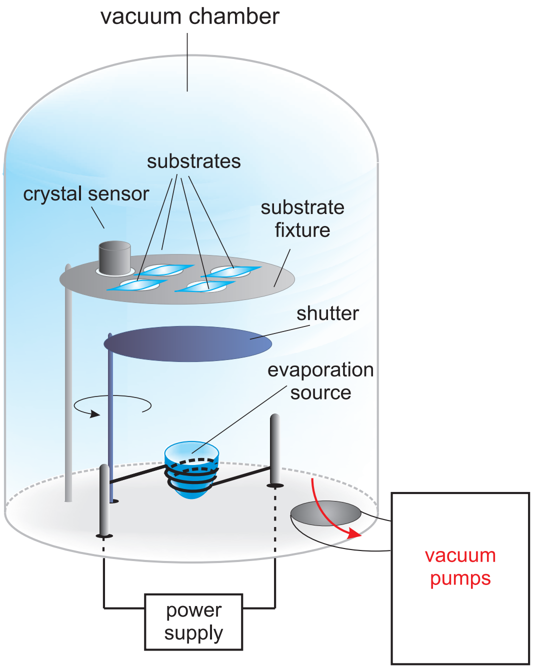

Figure A.1: Elements of a PVD system used for vacuum sublimation.

a crucible or boat, called the evaporation source, that is heated by controlled electric current flow. Glass substrates are mounted above the source behind a shutter. When the temperature of the material in the evaporation source reaches a suitable value the shutter is removed and a thin layer of material is evaporated on the substrate through a shadow mask of a chosen shape. Thickness control is usually provided via crystal sensor located near the substrate. Depending on the type of evaporated material and the structure one wants to obtain substrates may be heated or cooled during the deposition process. One must remember, that even if no heating is applied the temperature of the substrate may rise significantly during the evaporation process affecting the obtained structure. The latter, as well as thickness and quality of evaporated layers depend on many factors, including vacuum conditions, deposition rate, crucible type and the distance between evaporation source and substrates. More homogeneous layers are usually obtained when substrate fixtures with rotation about vertical axis are used. Some High-Tech systems developed especially for organic electronics are equipped with few organic low temperature evaporation sources and several high temperature metal sources. In addition, these systems often combine thermal evaporation with other vacuum deposition techniques, like magnetron sputtering, e-beam evaporation and atomic layer deposition. Thanks to these features whole device consisted of buffer layers, active layer and electrodes can be produced in one cycle without the necessity of breaking the vacuum after each evaporation step. This benefit is extremely important since organic materials show high sensitivity to water and oxygen. Another advantage of employing few evaporation sources in one system is the possibility of co-evaporation, i.e. simultaneous deposition of several different materials. Such approach enables to produce bulk heterojunctions of insoluble materials [**?**, 123, 124].

Thin films fabricated using this method are high quality layers, however the cost of their production, affected mainly by high vacuum requirement, is rather high. Moreover, such method is unsuitable for large scale devices, so it can not be implemented for the fabrication of large area low cost commercial solar cells.

- **Spin coating**

  Spin coating is a relatively simple and one of the most common solution processing techniques used for fabrication of thin films of organic and inorganic soluble materials, especially polymers. Spin coating procedure involves few steps: dispense, spin-up and drying (Fig. A.2). During the first step small volume of a solution of a material is manually or automatically dispensed on the center of a substrate mounted on a rotating chuck. Automatic dispense is much more convenient since it provides better control over the amount of deposited material and as a consequence it increases reproducibility of layer thickness and its properties. Droplet of the liquid can be deposited either on a static substrate (static dispense) or on a substrate rotating with a relatively low speed around 30 rps (dynamic dispense). Very often, after dispense step a spin-up step is carried out during which angular velocity of a substrate increases in time, usually linearly, till it reaches the final value. Since the substrate is rotating and initially there is no inward force acting on molecules of casted solution liquid starts to spread out radially on the substrate. Moreover, as a consequence of angular acceleration additional twisting force is applied to the resin so that the solution is distributed over substrate's surface more evenly. The excess of liquid that gets to the edge of the substrate is removed from the spin bowl via a series of small drains drilled in the chuck. As substrate rotates thinning of deposited layer along with solvent evaporation occurs. As a result of the latter viscosity of the resin increases to such extent that it prevents from further thinning of the layer induced by rotation. The final step involves rotation with lower spin speed and is dedicated to the drying process. This stage is especially important in case of thick films. Drying rate is dependent on many factors like volatility of used solvent and the ambient air around the substrate.

Although spin coating technique is a quite simple method final thickness, homogeneity and other properties of the spin coated layer are affected by a great variety of factors. Not only spin coating conditions, such as dispense type, spin speed, acceleration, time of each stage of the process but also properties of the initial solution, like its viscosity, concentration, solvent volatility and wetting abilities along with ambient air conditions (temperature, humidity, air flow, turbulence etc.) have a strong impact on the fabricated layer. That is why the spin coating parameters mentioned above and solvent type have to be chosen individually for each of deposited materials. Moreover, it is not so trivial to predict the thickness of deposited layer knowing these parameters. In general it is obvious that higher spin speeds and longer spin times lead to thinner layers, but there are no universal formulas that can be applied to calculate the final thickness of any material knowing these deposition conditions due to the number of factors affecting this parameter. However, Chang et al. [125] managed to develop theoretical model describing spin coating of conjugated polymers, such as MEH-PPV and P3HT, for electronic and optoelectronic applications. Despite the above mentioned complexity, once the proper solvent and spin coating parameters suitable for a given material are chosen thin layers of this material are easily fabricated. Furthermore this method is cheap and quick, but there is a serious drawback of this technique: it is not applicable to large area substrates. Hence, spin coating is suitable only for small scale laboratory devices and cannot be used for commercial production of large area electronics.

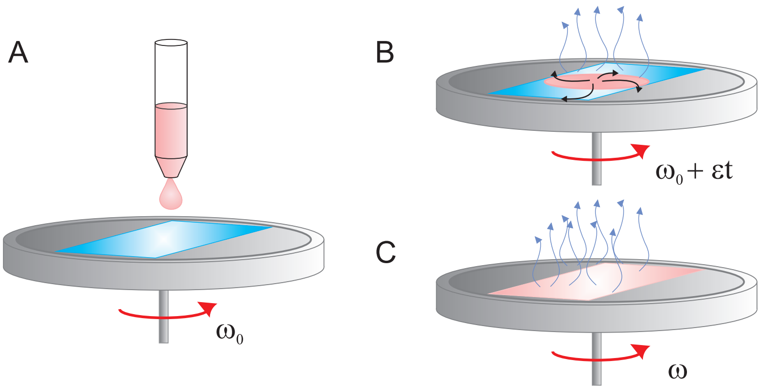

Figure A.2: Stages of a spin coating process: dispense of the liquid on a static or slowly spinning substrate (a); spin-up step, during which centrifugal force and twist cause spreading of the resin over the substrate's surface (b); drying of the layer rotating at the speed lower than the maximum speed of the spin-up step (c); ω_0-initial angular speed, ε -angular acceleration, t-time, ω -final angular speed during drying stage.

A.2 Characterization of individual layers

This section presents a short overview of methods used for characterization of surface topography, thickness and absorption of individual layers forming the devices investigated in the course of this study.

A.2.1 Atomic force microscopy

Atomic force microscopy (AFM) is one of the most common non-destructive methods used to investigate the surface structure of various materials. Operational principle of the atomic force microscope is illustrated in Fig. A.3. In contrast to scanning electron microscopy (SEM) conductivity of a sample is not a prerequisite for usage of AFM, thus the latter method was chosen to characterize surface topography of fabricated layers. In this technique dimensions of a scanned area can be tuned from few tens of microns down to few hundreds of nanometers keeping near-atomic-resolution of 3D images. These images provide information on surface roughness and feature sizes as small as few angstroms. Topography of a sample is mapped on the basis of local atomic interactions between molecules at the scanned surface and molecules at a sharp tip that is located at a cantilever scanning the sample (such cantilever with one or few tips is called a probe).

These interactions cause deflection of the cantilever. Determination of this deflection is done using a photodetector and a laser beam that is directed at a back of a cantilever. Light reflected from a deflected cantilever reaches a photodetector (usually a split photodiode) that measures the intensity of light. Knowing the changes in light intensity, molecular interactions that caused deflection of a tip are evaluated, and thus, the distance between the tip and the surface of the scanned fragment of the sample is found. Photodetector is connected to a controller that governs the position of a piezoelectric scanner which moves the probe in x, y and z directions and the acquired data are sent to a computer where a 3D image of surface topography is created.

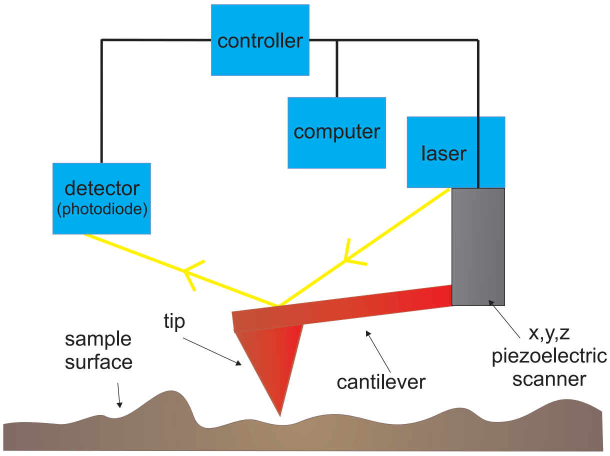

Figure A.3: Atomic force microscope setup.

A.2.2 Layer thickness and absorbance

Thickness of each layer was measured using profilometer AlphaStep 500 KLA Tencor. Absorbance measurements were carried out separately for each layer using Shimadzu 1240 UV-VIS spectrophotometer with a resolution not higher than 1 nm. Reference layers of materials used in the course of this study were deposited on thin glass substrates and used for absorption measurements and AFM measurements.

Absorbance A, also called the optical density, is defined as

$$A = \log \frac{I_0}{I} \, , \tag{A.1}$$

where I_0 is the incident light intensity and I stands for the intensity of light right behind the illuminated layer. Assuming that Lambert-Beer law holds for investigated samples and knowing the thickness of the absorbing layer and its absorbance one is able to determine the linear absorption coefficient κ of the investigated material.

A.3 Solution processing of MEH-PPV layers and their absorbance

According to Gaudin et al. [126] absorption spectrum of thin layers of MEH-PPV is dependent on the thickness of the film. Namely, the greatest peak of the absorption spectrum is blue-shifted for thicker layers. On the basis of measurements run for samples of different thickness fabricated from chlorobenzene solution of different concentrations at different spin speeds the authors inferred, that the above mentioned relation can be completely accounted for by reflection and interference effects and is not related to morphology of the film. In order to verify the thickness dependence of absorption spectrum of MEH-PPV layers cast from toluene solution films of different thickness were deposited from solutions of 0.5 wt.% concentrations on glass substrates cleaned in ultrasonic bath in acetone and isopropanol and dried in a hot air flow. As it was mentioned, MEH-PPV was purchased form Sigma-Aldrich and used as received without further purification. Dynamic dispense was applied with no spin-up stage, i.e. a droplet of the MEH-PPV solution was cast on a substrate already rotating with the desired final speed. Fig. A.4A shows absorption spectra in the 350-650 nm range recorded for MEH-PPV layers of different thickness deposited from the same solution batch. Variation of film thickness was obtained by change in spin speed and application of a multistage spin coating procedure. During this procedure few droplets of the same solution were cast one by one on the same substrate in about one-minute time intervals, so that layers of greater thickness were fabricated. Final thickness of the films was not measured, since the ratio of the thickness of samples should be equal to the ratio of absorbance values measured for these samples at the same wavelength. As one can see, there is hardly any difference in the position of the

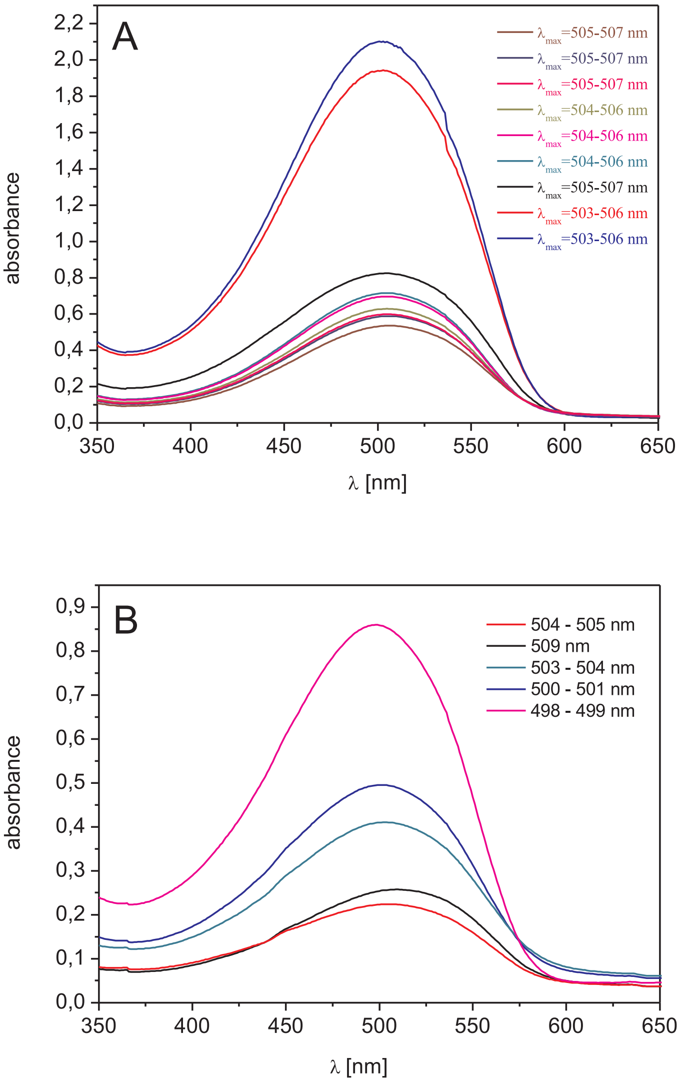

Figure A.4: Absorption spectrum of MEH-PPV layers of different thickness fabricated from the same toluene solution but at different spin speeds. $\lambda_{\max}$ denotes the position of the absorption peak (A); Absorption spectrum of MEH-PPV layers of different thickness fabricated from the same toluene solution but subjected to the ultrasonic treatment of different duration (B). The thicker the layer is, i.e. the greater its absorption is, the longer was the treatment. The thinnest layer was fabricated from the pristine solution before the ultrasound treatment.

absorption peaks $\lambda_{\max}$ for these layers even though the thickness of the thickest MEH-PPV layer is one order of magnitude greater than the thickness of the thinnest film ($\lambda_{\max}$ for these layers are 503-506 nm and 505-507 nm respectively). Differences in the position of these absorption peaks are rather within the experimental error. However, thickness dependence of the absorption spectrum was found when layers of different thickness were fabricated after ultrasonic treatment of the solution when duration of such treatment was varied. Absorption spectra of MEH-PPV films fabricated this way are shown in Fig. A.4B. The thinnest layer, i.e. the one showing the lowest absorption, was spin coated before the ultrasonic treatment. The longer the time of the treatment was the greater was the thickness of a deposited layer. A blue-shift of the absorption peak with increasing thickness of these films is pronounced in this case. Since previous investigation shown no effects of reflectance and interference on absorption of MEH-PPV layers of different thickness, the shift observed in the second case should not result from these effects either. It should be rather associated with change in morphology of the layer caused by the ultrasonic treatment that could affect the conjugation length of MEH-PPV chains. Such change in morphology could also follow from the change in solution concentration and temperature during the treatment.

A.4 Surface topography

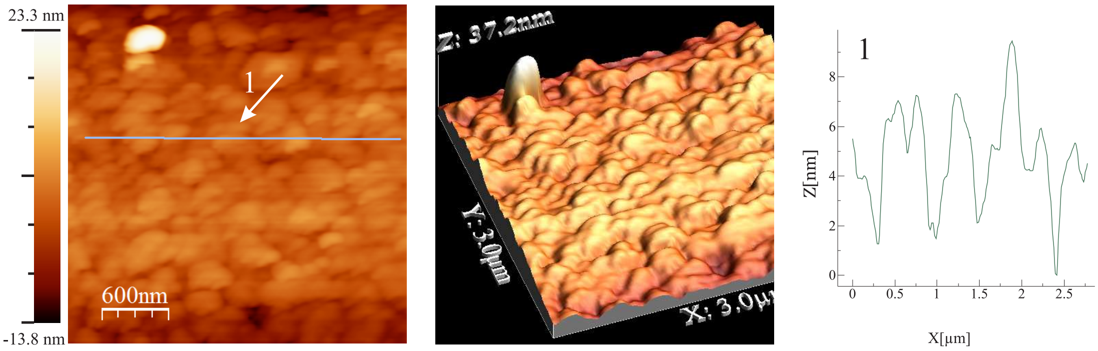

Figure A.5: AFM 2D (left) and 3D (middle) top views of a surface of ITO substrate recorded for a 3 x 3 μm fragment and a surface roughness profile 1 (right) for this fragment.

It is believed that surface of ITO is rather rough which affects the electric contact between this electrode and an adjacent organic layer and may cause shorting. It is also believed, that such negative effects can be prevented by application of

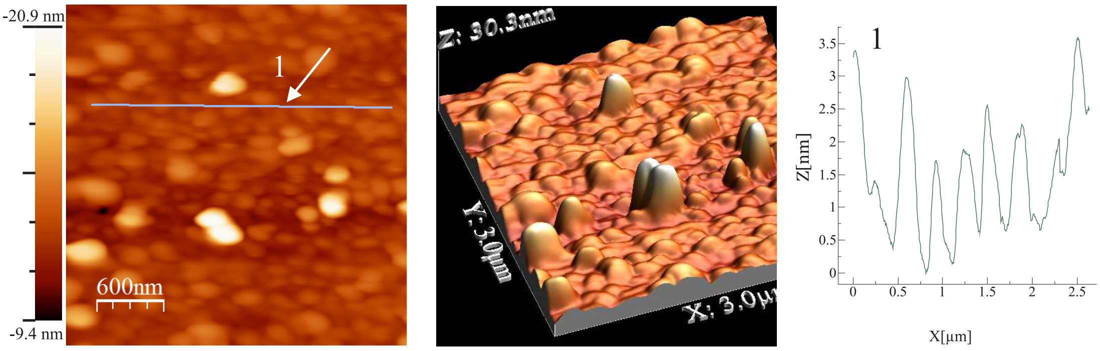

Figure A.6: AFM 2D (left) and 3D (middle) top views of a surface of 5 nm thick MoO_3 layer deposited on the top of ITO substrate recorded for a 3 x 3 μm fragment and a surface roughness profile 1 (right) for this fragment.

buffer layers [64] that may smooth out the surface of the electrode. Layer surface topography of bare ITO, MoO_3 deposited on the top of ITO, BCP and the underlying F_{16}ZnPc film was investigated by means of atomic force microscopy. Collected AFM data were processed using a freeware Nanotec WsxM Program [127] available at www.nanotec.es. Fig. A.5 shows the 2D and 3D AFM scans of a 3x3 μm ITO fragment and its roughness profile recorded along the line shown on the scan. As one can see, surface of the ITO electrode is rather smooth, with regular grain-like features about 0.5 μm wide and at most 6 nm high. Next scans shown in Fig. A.6 present 2D and 3D surface topographies and roughness profile of a 5 nm thick MoO_3 anodic buffer layer evaporated on the top of the ITO electrode. The size of the scanned fragment and magnification are the same as in case of the ITO fragments to enable comparison of surface topographies of these materials. MoO_3 deposited on the top of ITO forms very similar grain-like structures of more less the same size, though probably a bit more smooth than the ones observed for bare ITO substrates since the maximum height of the profile 1 recorded for MoO_3 scan is less than 4 nm. Thus, MoO_3 may improve the contact between the donor layer and the ITO electrode. Bright high features visible on the scans might be some MoO_3 crystallites that were torn out of the sample during transport or some impurities. Moreover, it is probable that MoO_3 does not fully cover the ITO substrate, since the thickness of this interlayer is only 5 nm. AFM top views of 100 nm - thick F_{16}ZnPc layer deposited on a glass substrate are presented in Figs. A.7 and A.8, while scans of the 15 nm - thick cathodic buffer layer evaporated on the top of the former material are shown in Fig. A.9. In the first set of images taken

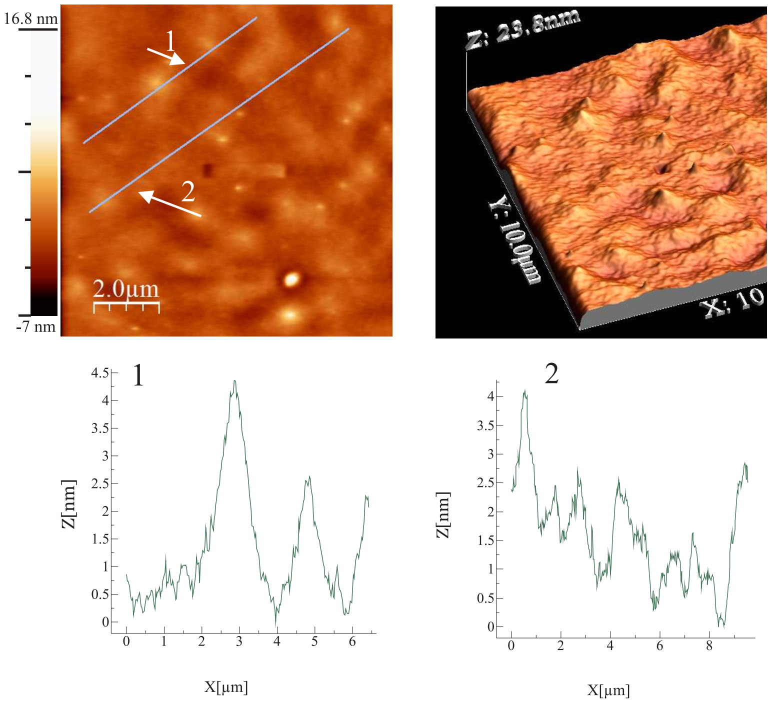

Figure A.7: AFM top views of a 100 nm thick F_{16}ZnPc layer deposited on a glass substrate. 2D image (top left), 3D image (top right), surface roughness profiles 1 and 2 (bottom), scan size 10x10 μm.

for a 10x10 μm fragment (Fig. A.7) one can distinguish quite regular crystallites about 1-2 μm wide and only few nanometers high, so the surface of the F_{16}ZnPc layer is relatively smooth. If we take a closer look at the surface topography of this layer (Fig. A.8top) we will be able to distinguish pyramid-shaped crystallites (well pronounced at a 3D image and a surface roughness profile 1), but apart from that we will also notice very regular elongated parallel stripes clearly visible on a 3D image. To estimate the width of these needles this image was flattened (Fig. A.8bottom) and a surface roughness profile 2 after flattening was drawn. The width of stripes estimated on the basis of this profile is around 10-30 nm, while their length determined from the 3D image seems to be larger than 3 microns. Similar elongated structures were observed by Torne for thin (12-34 nm) films of perfluorocopperphthalocyanine deposited on Al_2O_3 [95]. The length of these F_{16}CuPc needles was few microns while their width ranged from 20 nm to 100 nm. Interestingly, though Torne fabricated thin F_{16}CuPc layers using the

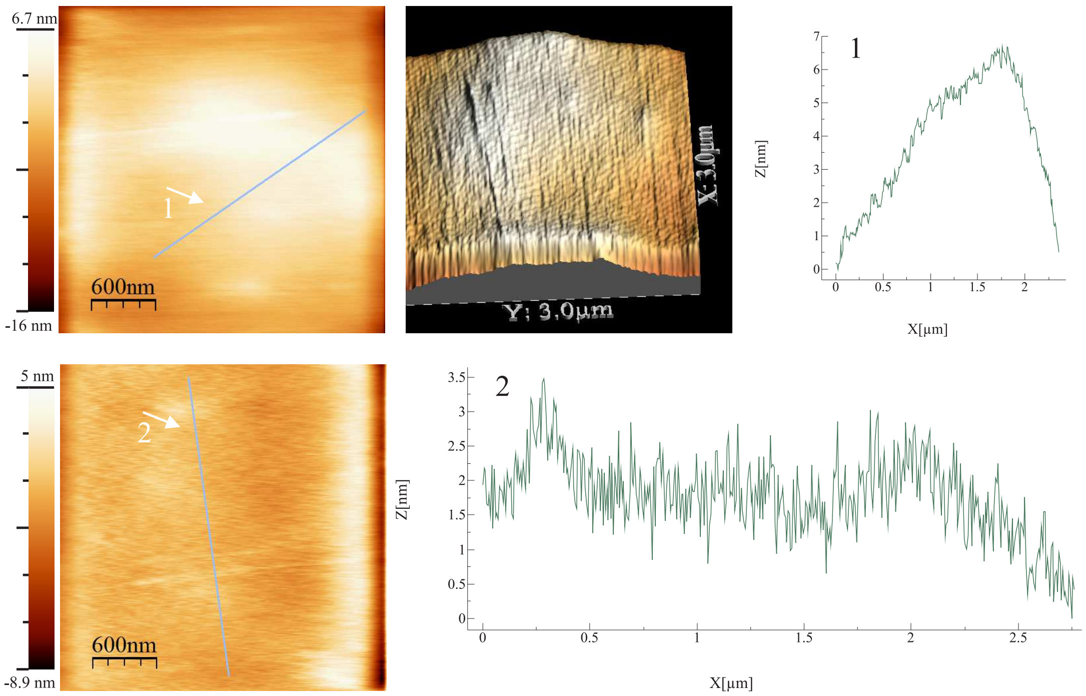

Figure A.8: AFM top views of a 100 nm thick F_{16}ZnPc layer deposited on a glass substrate: 2D image (left), 3D image (middle), surface roughness profile 1 (right) (top); flattened 2D image (left) and surface roughness profile 2 (right) found for this image (bottom). Scan size 3x3 μm.

same method (namely molecular beam epitaxy) on three different substrates, i.e. oxidized silicon wafers, sapphire (single-crystalline Al_2O_3 and MgO, he obtained such elongated highly-ordered structures, only for Al_2O_3 substrates, while in case of SiO_2 needle-shaped crystallites of much smaller size and random orientation were produced. Such highly-ordered films fabricated on Al_2O_3 shown anisotropic electrical and optical properties, like enhanced charge carrier transfer along the plane of the films caused by the upright stacking of molecules. Unfortunately, this is not the direction of electron transport in the fabricated devices. In contrast to thin F_{16}CuPc films produced on sapphire, the creation of highly-ordered needle-like F_{16}ZnPc crystallites fabricated in the course of this study should not be associated with substrate structure since the phthalocyanine layer is rather thick while the surface of glass is not ordered. This structural order should rather follow from the chosen PVD fabrication conditions. As one can see in Fig. A.9, a 15 nm thick bathocuproine layer evaporated on the top of such a highly-ordered F_{16}ZnPc film does not reproduce the topography of the latter. Moreover, the sur-

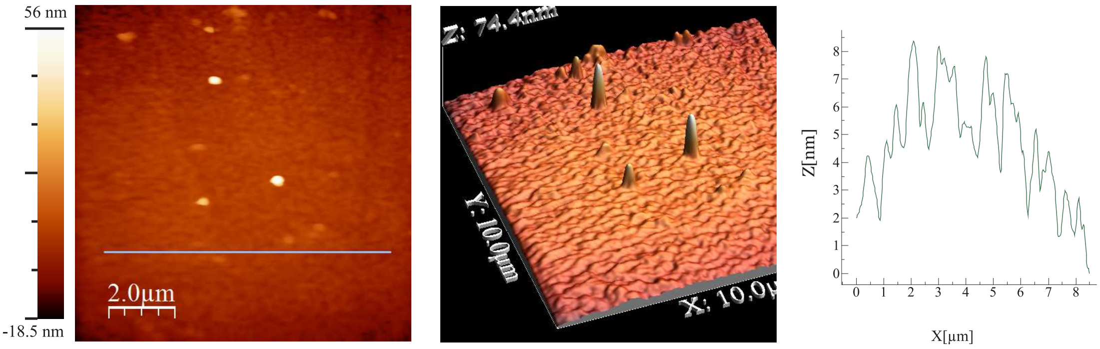

Figure A.9: 2D (left) and 3D (middle) AFM images of a 15 nm thick BCP layer deposited on the top of F_{16}ZnPc layer and a surface roughness profile 1 (right). Scan size 3x3 μm.

face of BCP evaporated on the top of perfluorozincphthalocyanine seems to be the most rough from among all layers fabricated by means of PVD in the course of this study, therefore the role of this layer is not to improve the contact with the cathode due to surface smoothing.

Bibliography

[1] M. Schubert, C. Yin, M. Castellani, S. Bange, T.L. Tam, A. Sellinger and H.-H. Hörhold, T. Kietzke, and D. Neher. Heterojunction topology versus fill factor correlations in novel hybrid small-molecular/polymeric solar cells. *J. Chem. Phys.*, 130, 2009.

[2] B. Lüssem, M. Riede, and K. Leo. Doping of organic semiconductors. *Phys. Status Solidi A*, 210:9–43, 2013.

[3] Z. Bao, A.J. Lovinger, and J. Brown. New air-stable n-channel organic thin film transistors. *J. Am. Chem. Soc.*, 120:207–208, 1998.

[4] J. L. Yang, S. Schumann, and T. S. Jones. Morphology and structure transitions of copper hexadecafluorophthalocyanine F16CuPc thin films. *J. Phys. Chem. C*, 114:10571063, 2010.

[5] D. Wróbel. Organic photovoltaic solar cells: spectroscopic and photoelectric properties of photoactive dyes. *C. R. Chimie*, 6:417429, 2003.

[6] R. Signerski, G. Jarosz, and B. Koscielska. Photovoltaic effect in hybrid heterojunction formed from cadmium telluride and zinc perfluorophthalocyanine layers. *J. Non-Cryst. Solids*, 356:20532055, 2010.

[7] T. Zhang, J. Huang, F. He, L. Chen, G. Niu, J. Pan, and Q. Song. The effect of built-in field on the interface exciton recombination and dissociation in nn type organic solar cells. *Sol. Energ. Mat. Sol. Cells*, 112:7377, 2013.

[8] Q. L. Song, H. B. Yang, Y. Gan, Ch. Gong, and Ch. Ming Li. Evidence of harvesting electricity by exciton recombination in an n-n type solar cell. *J. Am. Chem. Soc.*, 132:45544555, 2010.

[9] K.C. Kao and W. Hwang. *Electrical transport in Solids With Particular Reference to Organic Semiconductors*. Pergamon Press, 1981.

[10] H. Ishii, K. Sugiyama, E. Ito, and K. Seki. Energy level alignment and interfacial electronic structures at organic/metal and organic/organic interfaces. *Adv. Mater.*, 11:605–625, 1999.

[11] *Organic Photovoltaics: Mechanisms, Materials, and Devices*. CRC Press, 2005.

[12] W. Tress, K. Leo, and M. Riede. Photoconductivity as loss mechanism in organic solar cells. *Phys. Status Solidi RRL*, 7:401405, 2013.

[13] J. Kalinowski. *Organic Light-Emitting Diodes. Principles, characteristics, and processes.* Marcel Dekker, 2005.

[14] D. Wróbel and A. Graja. Photoinduced electron transfer processes in fullereneorganic chromophore systems. *Coord. Chem. Rev.*, 255:2555 2577, 2011.

[15] *Handbook of organic materials for optical and* (*opto*)*electronic devices*. Woodhead Publishing Limited, 2013.

[16] H. Spanggaard and F. C. Krebs. A brief history of the development of organic and polymeric photovoltaics. *Sol. Energ. Mat. Sol. Cells*, 83:125146, 2004.

[17] C.W. Tang. Two-layer organic photovoltaic cell. *Appl. Phys. Lett.*, 48(2), 1986.

[18] N. S. Sariciftci, L. Smilowitz, A. J. Heeger, and F. Wudl. Photoinduced electron transfer from a conducting polymer to buckminsterfullerene. *Science*, 258(5087):1474–1476, 1992.

[19] B. O'Regan and M. Grätzel. A low-cost, high-efficiency solar cell based on dye-sensitized colloidal TiO_2 films. *Nature*, 353:737–740, 1991.

[20] N.-G. Park. *Advanced Concepts in Photovoltaics*, chapter 7. Royal Society of Chemistry, 2014.

[21] B. Qi and J. Wang. Open-circuit voltage in organic solar cells. *J. Mater. Chem.*, 22:24315, 2012.

[22] S. Gunes, H. Neugebauer, and N.S. Sariciftci. Conjugated polymer-based organic solar cells. *Chem. Rev.*, 107:1324–1338, 2007.

[23] M.C. Scharber, D. Mhlbacher, M. Koppe, P. Denk, Ch. Waldauf, A.J. Heeger, and Ch.J. Brabec. Design rules for donors in bulk-heterojunction solar cellstowards 10 percent energy-conversion efficiency**. *Adv. Mater.*, 18:789794, 2006.

[24] M. Riede, T. Mueller, W. Tress, R. Schueppel, and K. Leo. Small-molecule solar cellsstatus and perspectives. *Nanotechnology*, 19:424001–1–12, 2008.

[25] G. Richardson, C. Please, J. Foster, and J. Kirkpatrick. Asymptotic solution of a model for bilayer organic diodes and solar cells. *SIAM J. Appl. Math.*, 72:17921817, 2012.

[26] J.M. Foster, J. Kirkpatrick, and G. Richardson. Asymptotic and numerical prediction of current-voltage curves for an organic bilayer solar cell under varying illumination and comparison to the Shockley equivalent circuit. *J. App. Phys.*, 114:104501, 2013.

[27] K. Vandewal, K. Tvingstedt, A. Gadisa, O. Ingans, and J.V. Manca. Relating the open-circuit voltage to interface molecular properties of donor:acceptor bulk heterojunction solar cells. *Phys. Rev. B*, 81:125204–1–8, 2010.

[28] F. A. de Castro, J. Heier, F. Nüesch, and R. Hany. Origin of the kink in current-density versus voltage curves and efficiency enhancement of polymer-C_{60} heterojunction solar cells. *IEEE J. Sel. Top. Quant. Electron.*, 16:1690–1699, 2010.

[29] J. Yu, J. Huang, L. Zhang, and Y. Jiang. Energy losing rate and open-circuit voltage analysis of organic solar cells based on detailed photocurrent simulation. *J. Appl. Phys.*, 106:063103, 2009.

[30] D. Cheyns, J. Poortmans, P. Heremans, C. Deibel, S. Verlaak, B.P. Rand, and J. Genoe. Analytical model for the open-circuit voltage and its associated resistance in organic planar heterojunction solar cells. *Phys. Rev. B*, 77:165332–2–10, 2008.

[31] A. Moliton and J.-M. Nunzi. How to model the behaviour of organic photovoltaic cells. *Polym. Int.*, 55:583600, 2006.

[32] A. Kumar, S. Sista, and Y. Yang. Dipole induced anomalous S-shape I-V curves in polymer solar cells. *J. App. Phys.*, 105:094512, 2009.

[33] C.W. Schlenker and M.E. Thompson. The molecular nature of photovoltage losses in organic solar cells. *Chem. Commun.*, 47:37023716, 2011.

[34] R.A. Street, A. Krakaris, and S.R. Cowan. Recombination through different types of localized states in organic solar cells. *Adv. Funct. Mater.*, 22:46084619, 2012.

[35] B.P. Rand, D.P. Burk, and S.R. Forrest. Offset energies at organic semiconductor heterojunctions and their influence on the open-circuit voltage of thin-film solar cells. *Phys. Rev. B*, 75:115327, 2007.

[36] C. Waldauf, P. Schilinsky, J. Haucha, and C. J. Brabec. Material and device concepts for organic photovoltaics: towards competitive efficiencies. *Thin Solid Films*, 451 452:503507, 2004.

[37] H.-S. Shim, F. Lin, J. Kim, B. Sim, T.-M. Kim, C.-K. Moon, C.-K. Wang, Y. Seo, K.-T. Wong, and J.-J. Kim. Efficient vacuum-deposited tandem organic solar cells with fill factors higher than single-junction subcells. *Adv. Energy Mater. 2015*, 5:1500228, 2015.

[38] S. Fonash. *Solar Cell Device Physics*. Academic Press, 2 edition, 2010.

[39] M. Turek. Current and illumination dependent series resistance of solar cells. *J. Appl. Phys.*, 115:144503–1–6, 2014.

[40] R.R. Lunt, N.C. Giebink, A.A. Belak, J.B. Benziger, and S.R. Forrest. Exciton diffusion lengths of organic semiconductor thin films measured by spectrally resolved photoluminescence quenching. *J. Appl. Phys.*, 105, 2009.

[41] C.J. Brabec, V. Dyakonov, J. Parisi, and N.S. Sariciftci. *Organic Photovoltaics: concepts and realization*. Springer-Verlag, 2003.

[42] D. Kurrle and J. Pflaum. Exciton diffusion length in the organic semiconductor diindenoperylene. *Appl. Phys. Lett.*, 92:133306–1–3, 2008.

[43] T.M. Clarke and J.R. Durrant. Charge photogeneration in organic solar cells. *Chem. Rev.*, 110:67366767, 2010.

[44] I. Bruder. *Organic solar cells: Correlation between molecular structure, morphology and device performance*. PhD thesis, University of Stuttgart, Max Planck Institute for Solid State Research, 2010.

[45] A. Petersen, A. Ojala, T. Kirchartz, T.A. Wagner, F. Würthner, and U. Rau. Field-dependent exciton dissociation in organic heterojunction solar cells. *Phys. Rev. B*, 85:245208–1–10, 2012.

[46] K. Vandewal, S. Albrecht, E.T. Hoke, K.R. Graham, J. Widmer, J.D. Douglas, M. Schubert, W.R. Mateker, J.T. Bloking, G.F. Burkhard, A. Sellinger, J.M.J. Fr$e$chet, A. Amassian, M.K. Riede, M.D. McGehee, D. Neher, and A. Salleo. Efficient charge generation by relaxed charge-transfer states at organic interfaces. *Nature Mater.*, 13:6368, 2014.

[47] M.T. Lloyd, J.E. Anthony, and G.G. Malliaras. Photovoltaics from soluble small molecules. *Mater. Today*, 10:34–41, 2007.

[48] R.A. Street. Carrier mobility, structural order, and solar cell efficiency of organic heterojunction devices. *Appl. Phys. Lett.*, 93:133308–1–3, 2008.

[49] H. Hoppe and N.S. Sariciftci. Morphology of polymer/fullerene bulk heterojunction solar cells. *J. Mater. Chem.*, 16:45–61, 2006.

[50] X. Yang, J. Loos, S.C. Veenstra, W.J.H. Verhees, M.M. Wienk, J.M. Kroon, M.A.J. Michels, and R.A.J. Janssen. Nanoscale morphology of high-performance polymer solar cells. *Nano Lett.*, 5(4), 2005.

[51] D.J. Lipomi, R.C. Chiechi, W.F. Reus, and G.M. Whitesides. Laterally ordered bulk heterojunction of conjugated polymers: Nanoskiving a jelly roll. *Adv. Funct. Mater.*, 18:34693477, 2008.

[52] T. Ameri, N. Lia, and C.J. Brabec. Highly efficient organic tandem solar cells: a follow up review. *Energy Environ. Sci.*, 6:2390, 2013.

[53] J. You, L. Dou, K. Yoshimura, T. Kato, K. Ohya, T. Moriarty, K. Emery, C.-C. Chen, J. Gao, G. Li, and Y. Yang. A polymer tandem solar cell with 10.6 percent power conversion efficiency. *Nat. Commun.*, 4:1446, 2013.

[54] J. You, C.-C. Chen, Z. Hong, K. Yoshimura, K. Ohya, R. Xu, S. Ye, J. Gao, G. Li, and Y. Yang. 10.2 percent power conversion efficiency polymer tandem solar cells consisting of two identical sub-cells. *Adv. Mater.*, 25:39733978, 2013.

[55] H. Zhou, Y. Zhang, C.-K. Mai, S.D. Collins, G.C. Bazan, T.-Q. Nguyen, and A.J. Heeger. Polymer homo-tandem solar cells with best efficiency of 11.3 percent. *Adv. Mater.*, 27:17671773, 2015.

[56] A. Yella, H.-W. Lee, H.N. Tsao, C. Yi, A.K. Chandiran, Md.K. Nazeeruddin, E. W.-G. Diau, C.-Y. Yeh, S.M. Zakeeruddin, and M. Grätzel. Porphyrin-sensitized solar cells with cobalt (II/III) based redox electrolyte exceed 12 percent efficiency. *Science*, 334:629–634, 2011.

[57] M. Grätzel. Dye-sensitized solar cells. *J. Photochem. Photobiol. C: Photochem. Rev.*, 4:145–153, 2003.

[58] Y. Bai, Y. Cao, J. Zhang, M. Wang, R. Li, P. Wang, S.M. Zaekeeruddin, and M. Grätzel. High-performance dye-sensitized solar cells based on solvent-free electrolytes produced from eutectic melts. *Nature Mater.*, 7, 2008.

[59] S. Fantacci, F. De Angelis, M. K. Nazeeruddin, and M. Grätzel. Electronic and optical properties of the Spiro-MeOTAD hole conductor in its neutral and oxidized forms: A DFT/TDDFT investigation. *J. Phys. Chem. C*, 115:2312623133, 2011.

[60] J.H. Heo, S.H. Im, J. H. Noh, T. N. Mandal, C.-S. Lim, J. Ah Chang, Y. H. Lee, H.-J. Kim, A. Sarkar, Md. K. Nazeeruddin, M. Grätzel, and S. I. Seok. Efficient inorganic-organic hybrid heterojunction solar cells containing perovskite compound and polymeric hole conductors. *Nature Photon.*, 7:486491, 2013.

[61] E. L. Ratcliff, B. Zacher, and Neal R. Armstrong. Selective interlayers and contacts in organic photovoltaic cells. *J. Phys. Chem. Lett.*, 2:13371350, 2011.

[62] A. Eischner and S. Kirchmeyer. *Organic Photovoltaics: Materials, Device Physics, and Manufacturing Technologies*, chapter VII. WILEY-VCH Verlag GmbH & Co. KGaA, 2008.

[63] V. Shrotriya, G. Li, Y. Yao, C.-W. Chu, and Y. Yang. Transition metal oxides as the buffer layer for polymer photovoltaic cells. *App. Phys. Lett.*, 88:073508, 2006.

[64] J.C. Bernede, L. Cattin, M. Morsli, and Y. Berredjem. Ultra-thin metal layer passivation of the transparent conductive anode in organic solar cells. *Sol. Energ. Mat. Sol. Cells*, 92:1508–1515, 2008.

[65] M. Y. Chan, C. S. Lee and S. L. Lai, M. K. Fung, F. L. Wong, H. Y. Sun, K. M. Lau, and S. T. Lee. Efficient organic photovoltaic devices using a combination of exciton blocking layer and anodic buffer layer. *J. Appl. Phys.*, 100:094506–1–4, 2006.

[66] K. Lee, J. Y. Kim, S. H. Park, S. H. Kim, S. Cho, and A. J. Heeger. Air-stable polymer electronic devices. *Adv. Mater.*, 19:24452449, 2007.

[67] A. Chuchmała, M. Palewicz, A. Sikora, and A. Iwan. Influence of graphene oxide interlayer on PCE value of polymer solar cells. *Synt. Met.*, 169:33–40, 2013.

[68] H. Xu, L. Yang, H. Tian, S. Yin, and F. Zhang. Rhenium oxide as the interfacial buffer layer for polymer photovoltaic cells. *Optoelectron Lett.*, 6:0176–0178, 2010.

[69] D.Y. Kim. *Organic photovoltaic cells and organic up-conversion devices*. PhD thesis, University of Florida, 2009.

[70] X. Jiang, J. Dai, H. Wang, Y. Geng, and D.H. Yan. Organic photovoltaic cells using hexadecafluorophthalocyaninatocopper ($F_{16}CuPc$) as electron acceptor material. *Chem. Phys. Lett.*, 446:329–332, 2007.

[71] J.L. Yang, S. Schumann, R.A. Hatton, and T.S. Jones. Copper hexadecafluorophthalocyanine F_{16}CuPc as an electron accepting material in bilayer small molecule organic photovoltaic cells. *Organic Electronics*, 11:13991402, 2010.

[72] J.L. Yang, P. Sullivan, S. Schumann, I. Hancox, and T.S. Jones. Organic photovoltaic cells based on unconventional electron donor fullerene and electron acceptor copper hexadecafluorophthalocyanine. *App. Phys. Lett.*, 100:023307, 2012.

[73] R. Signerski. On the light intensity dependence of short-circuit current of bilayer organic photovoltaic cells. *J. Non-Cryst. Solids*, 354:44654468, 2008.

[74] R. Signerski, G. Jarosz, J. Szostak, and J. Godlewski. Struktury fotowoltaiczne z planarnym heterozłšczem półprzewodnik II-VI/półprzewodnik molekularny. *Prace Instytutu Elektrotechniki*, 264:91–98, 2014.

[75] T. Stübinger and W. Brütting. Exciton diffusion and optical interference in organic donoracceptor photovoltaic cells. *J. Appl. Phys*, 90:3632–3641, 2001.

[76] P. Peumans, A. Yakimov, and S.R. Forrest. Small molecular weight organic thin-film photodetectors and solar cells. *J. Appl. Phys.*, 93:3693–3723, 2003.

[77] N. Karl. Charge carrier transport in organic semiconductors. *Synt. Met.*, 133-134:649–657, 2003.

[78] R. Signerski and J. Kalinowski. Modeling of photoelectrical properties of metal/organic solid/metal systems. *Mol. Cryst. Lig. Cryst.*, 228:213–219, 1993.

[79] P. de Bruyn, A.H.P. van Rest, G.A.H. Wetzelaer, D. M. de Leeuw, and P.W. M. Blom. Diffusion-limited current in organic metal-insulator-metal diodes. *Phys. Rev. Let.*, 111:186801, 2013.

[80] J. Godlewski. Currents and photocurrents in organic materials determined by the interface phenomena. *Adv. Colloid Interface Sci.*, 116:227–243, 2005.

[81] J. Godlewski. *Wstęp do elektroniki molekularnej*. Wydawnictwo Politechniki Gdańskiej, 2008.

[82] M.Pope and Ch.E. Swenberg. *Electronic Processes in Organic Crystals and Polymers*. Oxford University Press, second edition edition, 1999.

[83] W. J. Potscavage Jr., S. Yoo, and B. Kippelen. Origin of the open-circuit voltage in multilayer heterojunction organic solar cells. *Appl. Phys. Lett.*, 93:193308–1–3, 2008.

[84] M. Koehler, N. A. D. Yamamoto, A. G. Macedo, D. Z. Grodniski, L. S. Roman, and M. G. E. da Luz. The current-voltage characteristics of polymer/c60 diodes in the dark: A direct way to assess photovoltaic devices efficiency parameters. *Appl. Phys. Lett.*, 103:033304–1–5, 2013.

[85] M.D. Perez, C. Borek, S.R. Forrest, and M.E. Thompson. Molecular and morphological influences on the open circuit voltages of organic photovoltaic devices. *J. Am. Chem. Soc.*, 131:92819286, 2009.

[86] B. Qi and J. Wang. Open-circuit voltage in organic solar cells. *J.Mater.Chem.*, 22:24315–1–11, 2012.

[87] J. Godlewski M. Obarowska. Electric field dependence of the bimolecular recombination rate of the charge carriers. *Synt. Met.*, 109:219–222, 2000.

[88] Zong-Xiang Xu, V. A. Roy, Peter Stallinga, Michele Muccini, and Stefano Toffanin et al. Nanocomposite field effect transistors based on zinc oxide/polymer blends. *Appl. Phys. Lett.*, 90:223509–1–3, 2007.

[89] U. Hörmann, J. Wagner, M. Gruber, A. Opitz, and W. Brütting. Approaching the ultimate open circuit voltage in thiophene based single junction solar cells by applying diindenoperylene as acceptor. *Phys. Status Solidi RRL*, 5(7):241 243, 2011.

[90] M. Pfeiffer, K. Leo, and N. Karl. Fermi level determination in organic thin films by the Kelvin probe method. *J. Appl. Phys.*, 80:6880–6883, 1996.

[91] L. Xue, L. Liu, Q. Gao, S. Wen, J. He, and W. Tian. Planar-diffused photovoltaic device based on the MEH-PPV/PCBM system prepared by solution process. *Sol. Energ. Mat. Sol. Cells*, 93:501–507, 2009.

[92] T. Yamanari, T. Taima, J. Sakai, and K. Saito. Origin of the open-circuit voltage of organic thin-film solar cells based on conjugated polymers. *Sol. Energ. Mat. Sol. Cells*, 93:759–761, 2009.

[93] A. Ltaief, J. Davenas, A. Bouazizi, R. B. Chaâbane, P. Alcouffe, and H. B. Ouada. Film morphology effects on the electrical and optical properties of bulk heterojunction organic solar cells based on MEH-PPV/C60 composite. *Mater. Sci. Eng. C*, 25:67–75, 2005.

[94] J. Wagner, M. Gruber, A. Hinderhofer, B. Bröker A. Wilke, J. Frisch, P. Amsalem, A. Vollmer, A. Opitz, N. Koch, F. Schreiber, and W. Brütting. High fill factor and open circuit voltage in organic photovoltaic cells with diindenoperylene as donor material. *Adv. Funct. Mater.*, 20:42954303, 2010.

[95] Josep Oriol Ossó Torné. *Growth, structure and optical properties of highly ordered organic thin films of phthalocyanine and diindenoperylene.* PhD thesis, Instituto de Ciencia de Materiales de Barcelona, Max-Planck-Institut für Metallforschung, 2004.

[96] N. Wang, J. Yu, Y. Zang, J. Huang, and Y. Jiang. Effect of buffer layers on the performance of organic photovoltaic cells based on copperphthalocyanine and C60. *Sol. Energ. Mat. Sol. Cells*, 94:263–266, 2010.

[97] H.B. Michaelson. The work function of the elements and its periodicity. *J. Appl. Phys.*, 48:4729–4733, 1977.

[98] D.Y. Kim, G. Sarasqueta, and F. So. SnPc:C60 bulk heterojunction organic photovoltaic cells with MoO_3 interlayer. *Sol. Energ. Mat. Sol. Cells*, 93:1452–1456, 2009.

[99] J.W. Ma, Z. Liang, C. Jin, X.Y. Jiang, and Z.L. Zhang. Enhanced power efficiency for white oled with MoO_3 as hole injection layer and optimized charge balance. *Sol. St. Comm.*, 149:214–217, 2009.

[100] Y. Kinoshita, R. Takenaka, and H. Murata. Independent control of open-circuit voltage of organic solar cells by changing film thickness of MoO_3 buffer layer. *Appl. Phys. Lett.*, 92:243309–1–3, 2008.

[101] K. Zilberberg, J. Meyer, and T. Riedl. Solution processed metal-oxides for organic electronic devices. *J. Mater. Chem. C*, 1:4796, 2013.

[102] P. Peumans and S. R. Forrest. Very-high-efficiency double-heterostructure copper phthalocyanine/c60 photovoltaic cells. *Appl. Phys. Lett.*, 79:126–128, 2001.

[103] J.W. Kim, H.J. Kim, T.-M. Kim, T.G. Kim, J.-H. Lee, J.W. Kim, and J.-J. Kim. High performance organic planar heterojunction solar cells by controlling the molecular orientation. *Curr. Appl. Phys.*, 13:7–11, 2013.

[104] H. Gommans, B. Verreet, B.P. Rand, R. Muller, J. Poortmans, P. Heremans, and J. Genoe. On the role of bathocuproine in organic photovoltaic cells. *Adv. Funct. Mater.*, 18:3686–3691, 2008.

[105] J.Szostak, R.Signerski, and J. Godlewski. Photoelectric properties of a novel MEH-PPV/F_{16}ZnPc heterojunction. *Phys. Status Solidi A*, 210(11):2353 – 2358, 2013.

[106] A.J. Lewis, A. Ruseckas, O.P.M. Gaudin, G.R. Webster, P.L. Burn, , and I.D.W. Samuel. Singlet exciton diffusion in MEH-PPV films studied by excitonexciton annihilation. *Organic Electronics*, 7:452–456, 2006.

[107] P. E. Shaw, A. Ruseckas, and I. D. W. Samuel. Exciton diffusion measurements in Poly(3-hexylthiophene). *Adv. Mater.*, 20:35163520, 2008.

[108] L.-G. Yang, H.Z. Chen, and M. Wang. Optimal film thickness for exciton diffusion length measurement by photocurrent response in organic heterostructures. *Thin Solid Films*, 516:7701–7707, 2008.

[109] Y. Terao, H. Sasabe, and C. Adachi. Correlation of hole mobility, exciton diffusion length, and solar cell characteristics in phthalocyanine/fullerene organic solar cells. *Appl. Phys. Lett.*, 90:103515–1–3, 2007.

[110] M. Ichikawa. Measurement of exciton diffusion lengths of phthalocyanine derivatives based on interlayer excitation transfer. *Thin Solid Films*, 527:239–243, 2013.

[111] A. Ortiz-Conde and F.J. Garc$\acute{i}$a S$\acute{a}$nchez. Extraction of non-ideal junction model parameters from explicit analytic solutions of its I-V charactersitics. *Solid-State Electronics*, 49:465–472, 2005.

[112] A. Ortiz-Conde, F.J. Garc$\acute{i}$a S$\acute{a}$nchez, and J. Muci. New method to extract the model parameters of solar cells from the explicit analytic solutions of their illuminated I-V characteristics. *Sol. Energy Mater. Sol. Cells*, 90:352–361, 2006.

[113] M. Chegaar, G. Azzouzi, and P. Mialhe. Simple parameter extraction method for illuminated solar cells. *Solid-State Electron.*, 50:1234–1237, 2006.

[114] M. C. J. M. Vissenberg and M. Matters. Theory of the field-effect mobility in amorphous organic transistors. *Phys. Rev. B*, 57(20):12964–12967, 1998.

[115] J. Szostak, G. Jarosz, and R. Signerski. Photovoltaic properties of cadmium selenidetitanyl phthalocyanine planar heterojunction devices. *Chem. Phys.*, 456:5760, 2015.

[116] J. Godlewski, R. Signerski, G. Jarosz, M.Obarowska, and J. Szostak. Jedno- i dwuwarstwowe organiczne ogniwa fotowoltaiczne. *Prace Instytutu Elektrotechniki*, 264:81–90, 2014.

[117] J.Szostak, M. Makowska, G. Jarosz, R.Signerski, and J. Godlewski. Własnoci fotowoltaiczne układów organicznych. In *Materiały konferencyjne II Krajowej Konferencji Fotowoltaiki, Krynica 12-15 maja 2011*. Instytut Metalurgii i Inżynierii Materiałowej Polskiej Akademii Nauk, 2011.

[118] R. Signerski and G. Jarosz. Effect of buffer layers on performance of organic photovoltaic devices based on copper phthalocyanine - perylene dye heterojunction. *Opto-Electron. Rev.*, 19:468–473, 2011.

[119] J. Simon and J.-J.André. *Molecular Semiconductors.* Springer - Verlag, Berlin, 1985.

[120] A. Wagenpfahl, D. Rauh, M. Binder, C. Deibel, and V. Dyakonov. S-shaped current-voltage characteristics of organic solar devices. *Phys. Rev. B*, 82:115306, 2010.

[121] M. Jorgensen, K. Norrman, and F.C. Krebs. Stability/degradation of polymer solar cells. *Sol. Energ. Mater. Sol. Cells*, 92:686–714, 2008.

[122] P Kovacik, G. Sforazzini, A.G. Cook, S.M. Willis, P.S. Grant, H.E. Assender, and A.A.R. Watt. Vacuum-deposited planar heterojunction polymer solar cells. *ACS Appl. Mater. Interfaces*, 3(1):1115, 2011.

[123] G. Chen, H. Sasabe, Z. Wang, X.-F. Wang, Z. Hong, Y. Yang, and J. Kido. Co-evaporated bulk heterojunction solar cells with > 6.0 %efficiency. *Adv. Mater.*, 24:27682773, 2012.

[124] S. Schubert, M. Hermenau, J. Meiss, L. Müller-Meskamp, and K. Leo. Oxide sandwiched metal thin-film electrodes for long- term stable organic solar cells. *Adv. Funct. Mater.*, 22:49934999, 2012.

[125] C.-C. Chang, C.-L. Pai, W.-C. Chen, and S.A. Jenekhe. Spin coating of conjugated polymers for electronic and optoelectronic applications. *Thin Solid Films*, 479:254–260, 2005.

[126] O.P.M. Gaudin, I. D. W. Samuel, S. Amriou, and P.L. Burn. Thickness dependent absorption spectra in conjugated polymers: Morphology or interference? *Appl. Phys. Lett.*, 96:053305–1–3, 2010.

[127] I. Horcas, R. Fernandez, J.M. Gomez-Rodriguez, J. Colchero, J. Gomez-Herrero, and A. M. Baro. WSXM: A software for scanning probe microscopy and a tool for nanotechnology . *Rev. Sci. Instrum.*, 78:013705, 2007.